Dissertation
submitted to the
Combined Faculty of Mathematics, Engineering and Natural Sciences
of Heidelberg University, Germany
for the degree of
Doctor of Natural Sciences

Put forward by
Andreas Kirchner
born in Friedrichshafen.
Oral examination: 18.7.2024

Fluid-dynamic description

of an entire

heavy-ion collision

Referees:
Prof. Dr. Stefan Flörchinger
Prof. Dr. Carlo Ewerz

Abstract

Viscous fluid dynamics provides a very successful description of heavy-ion collisions. Recent high precision measurements at RHIC and the LHC allow to perform high precision studies and parameter extractions of the experimental data. For these analyses theoretical calculations require similar statistics as the experimental measurements, which becomes more and more challenging. For the efficient calculation of a large number of events the fluid-dynamic framework Fluid$u$M is presented and expanded in this thesis. Fluid$u$M is build on a background fluctuation splitting ansatz of the fluid fields together with a mode-by-mode decomposition allowing for an efficient gathering of statistics already on the level of the initial conditions. Different applications of Fluid$u$M using its speed and flexibility are presented.

In the second part the applicability of relativistic fluid dynamics is examined by extending the fluid-dynamic description of a heavy-ion collision to times before the collision. For this the incoming nuclei are already described as drops of liquid nuclear matter. The equations of motion based on energy-momentum and particle number conservation are solved for a toy model given by an expanding and contracting Hubble universe, which then is used to study the entropy production of this process.

Zusammenfassung

Die Dynamik viskoser Flüssigkeiten bietet eine sehr erfolgreiche Beschreibung von Schwerionenkollisionen. Die jüngsten Hochpräzisionsmessungen am RHIC und am LHC ermöglichen detaillierte Analysen und die Bestimmung von Parametern aus den experimentellen Daten. Für diese Analysen benötigen theoretische Berechnungen ähnliche viel Statistik wie die experimentellen Messungen, was eine immer größere Herausforderung darstellt. Für die effiziente Berechnung einer großen Anzahl von Ereignissen wird in dieser Arbeit das fluiddynamische Framework Fluid$u$M vorgestellt und weiterentwickelt. Fluid$u$M basiert auf einer Zerlegung der Fluidfelder in einen Hintergrund- und einen Fluktuationsteil zusammen mit einer Modenzerlegung. Dies ermöglicht das effiziente Sammeln von Statistik bereits auf der Ebene der Anfangsbedingungen. Verschiedene Anwendungen von Fluid$u$M, die dessen Geschwindigkeit und Flexibilität nutzen, werden vorgestellt.

Im zweiten Teil wird die Anwendbarkeit der relativistischen Fluiddynamik untersucht, indem die fluiddynamische Beschreibung einer Schwerionenkollision auf Zeiten vor der Kollision ausgedehnt wird. Hierfür werden die einfallenden Kerne bereits als Tropfen flüssiger Kernmaterie beschrieben. Die auf der Energie-Impuls- und Teilchenzahlerhaltung basierenden Bewegungsgleichungen werden für ein Spielzeugmodell gelöst, das durch ein expandierendes und kontrahierendes Hubble-Universum gegeben ist. Dieses Setting wird genutzt, um die Entropieerzeugung dieses Prozesses zu untersuchen.

Contents

1. Introduction

Our current understanding of modern physics is dominated by two main theories [1]: the standard model of particle physics [2, 3] and the Big Bang model [4, 5]. The standard model describes the interactions between elementary particles, while the Big Bang model explains the dynamics of our universe, starting from its inception until now. The standard model is formulated as a field theory that has been tested extensively by various experiments [6, 7]. On the contrary, the cosmological theory of the Big Bang is formulated mainly in terms of Einsteins theory of general relativity [8–12] and has a much more limited access to experimental observations, since it is (so far) impossible to create a universe in the lab. However, there is one kind of experiment connecting these two very different theories: the so-called heavy-ion collisions, also known as "little bangs". During a heavy-ion collision the ions of heavy elements (e.g. gold or uranium) are accelerated to almost the speed of light and are then brought to collision. This results in the formation of a drop of so-called quark gluon plasma (QGP), which expands rapidly. The QGP only exists for a brief moment directly after the collision since the energy density quickly reduces. The only experimentally accessible observables are related to the particles produced in the dying moments of the QGP. Although a heavy-ion collision and the Big Bang are very different events at first glance, they share some striking similarities:
A first similarity between the Big Bang and a heavy-ion collision is the rapid expansion of both systems. Moreover, it is conjectured that the QGP has also existed near the beginning of our universe. Furthermore, there are additional, more subtle similarities between the two systems. In both cases the initial conditions of the system are not directly accessible. All information about the systems and their evolutions need to be extracted from final state observables. An at first glance unexpected similarity is that both systems can be described in terms of viscous fluid dynamics [13–15]. This similarity is particularly striking when recalling that the Big Bang model describes matter (including dark matter) mainly interacting via gravity, whereas the QGP interacts via the strong interaction, also known as quantum chromodynamics (QCD).
In this thesis I will focus on the description of heavy-ion collisions by the means of fluid dynamics. These collisions share a strong connection to the study of quantum chromodynamics, since the interactions during the collision are mainly given by the interactions of quarks and gluons. However, studying heavy-ion collisions allows for much more than just the study of QCD. They also allow for the connection of multiple branches of physics, reaching from quantum field theory, to low energy nuclear structure and fluid dynamics. Experimental measurements can already be described reasonably well by the means of relativistic fluid dynamics. The shortcomings of this description reveal very interesting questions, such as the range of applicability of fluid dynamics. This particular question has sparked enough interest to motivate a run with lighter ions at one of the main experimental facilities to test the limits of the fluid-dynamic description [16]. This thesis aims at further developing the Fluid*u*M framework, created for an efficient description of heavy-ion collisions. Since the underlying equations of relativistic fluid dynamics are a complex system of non-linear partial differential equations, Fluid*u*M introduces a background fluctuation splitting together with a mode expansion scheme to allow for a fast numerical implementation together with a very efficient way of gathering statistics to compute event averages of observables. This makes Fluid*u*M an ideal tool for the exploration

of heavy-ion collisions and other fields of physics, such as nuclear structure.
Additionally, this thesis examines the applicability of fluid dynamics by extending the fluid description of a heavy-ion collision to times before the collision. Concretely, this means that the incoming nuclei are already treated as liquid drops of nuclear matter. This extension of the fluid description allows to study the thermalization dynamics and entropy production during the initial moments of a heavy-ion collision.
To begin I give an overview of the most important concepts used in the description of heavy-ion collisions, with the starting point being the underlying fundamental theory of quantum chromodynamics.

1.1. QCD and the QCD phase diagram

A fundamental part of the standard model of particle physics is the theory of quantum chromodynamics (see [17] for an extensive review), also known as QCD, governing the behavior of quarks and gluons. As part of the standard model QCD is formulated as gauge theory with its underlying symmetry being $SU(3)$. Similarly to quantum electrodynamics (with underlying symmetry $U(1)$) where charge is conserved, QCD also has a conserved quantity, called color. In total there are three colors, often referred to as red, green and blue in loose analogy to the primary colors. These colors are carried by the fermionic degrees of the theory, called quarks. The quarks appear in six different flavors (up, down, charm, strange, top and bottom), with the most abundant ones being the up and down quarks as building blocks of protons (consisting of 2 ups and one down) and neutrons (consisting of 1 up and 2 downs). The quarks interact via the exchange of gluons, acting as the force-carriers of QCD. Since QCD obeys the $SU(3)$ symmetry, there are eight different gluons, each carrying a color charge and an anti-color charge, due to color conservation at the QCD interaction vertices. An important difference to other gauge theories such as quantum electrodynamics is the non-abelian nature of $SU(3)$, allowing for self-interactions of the gluons via 3- and 4-gluon vertices.

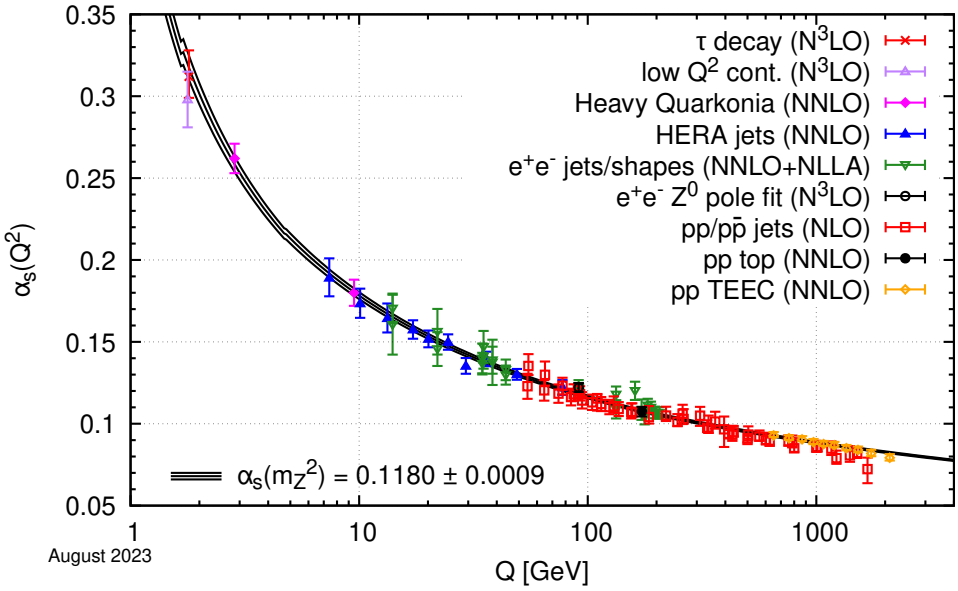

Figure 1: Comparison of measurements of the QCD coupling $\alpha_s(Q^2)$ as function of momentum Q with theoretical calculations, taken from [18]. The coupling decreases for increasing momentum Q.

One of the most interesting features of QCD is the running of its coupling constant α_s [1], which can be seen in fig. 1. The running coupling has two salient consequences: At high momentum Q, the strength of the interactions between quarks and gluons decreases leading to the phenomenon of so-called asymptotic freedom, allowing quarks and gluons to exist as almost free particles. For low momenta Q the interaction between quarks and gluons becomes very large, leading to the confinement of quarks and gluons within hadrons. These hadrons are color neutral states and are therefore not influenced by confinement. Depending on the number of quark constituents, the hadrons are either classified as mesons (two-quark bound states) or baryons (three-quark bound states). A further consequence of the running coupling is that the methods of perturbative QCD work well at high momentum scales, but stop being valid at low momentum scales. At these scales non-perturbative methods, such as lattice QCD, functional renormalization groups or the AdS/CFT correspondence can be employed. Lattice QCD [19] is formulated on a discretized space-time grid and allows a wide range of calculations ranging from the protons mass to the equation of state at finite densities. However, the so-called sign problem [20] makes calculations at high densities and low temperatures difficult, leaving some areas of the QCD phase diagram as topic of current research.

A current version of the phase diagram (see [21] for a comprehensive review) is shown in fig. 2 as function of temperature T and baryon chemical potential μ (often also labeled as μ_B). From everyday life experience it is well known that at low temperatures and low densities QCD matter appears in the form of confined hadrons. It has been shown by the means of among others lattice QCD and heavy-ion collisions, that at low chemical potential and high enough temperatures a second phase of deconfined quarks and gluons, the so-

[1] The coupling constant appearing in the Lagrangian of QCD is the so-called bare coupling determining the strength of interactions between the constituents of the theory. However, when probing the theory at different energy scales, these interactions get modified by virtual particles, effectively changing the coupling strength.

called quark gluon plasma (QGP) exists [22]. This region of ultra-high temperature and vanishing chemical potential is also of great interest from a cosmological point of view, since it is conjectured to recreate the conditions shortly after the Big Bang. More uncertainties arise when leaving the axis of vanishing chemical potential. The reasons for this are twofold: On the one hand lattice QCD looses accuracy due to the before mentioned sign problem. On the other hand, the regions of higher chemical potential become increasingly harder to access experimentally. The current main way of experimentally studying the QCD phase diagram is to collide nuclear matter and examine the outcome of the collision, i.e. heavy-ion collisions. By varying the center of mass energy $\sqrt{s}$, different amounts of energy and net baryon density can be deposited in the collision, allowing for different trajectories through the phase diagram (indicated by the green and pink lines in fig. 2). However, these trajectories cannot be extended arbitrarily in direction of $T = 0$. The reason of this limitation lies in the nature of heavy-ion collisions, where the compression of the matter during the collision produces a lot of entropy and therefore heat, making it impossible to reach the area of vanishing temperature and large chemical potential. An experimental possibility to study this region of the phase diagram are neutron stars, which allow to derive constraints on the QCD equation of state [23]. At very high chemical potentials (e.g. the core of a neutron star) it is conjectured that a color superconductor forms [24].

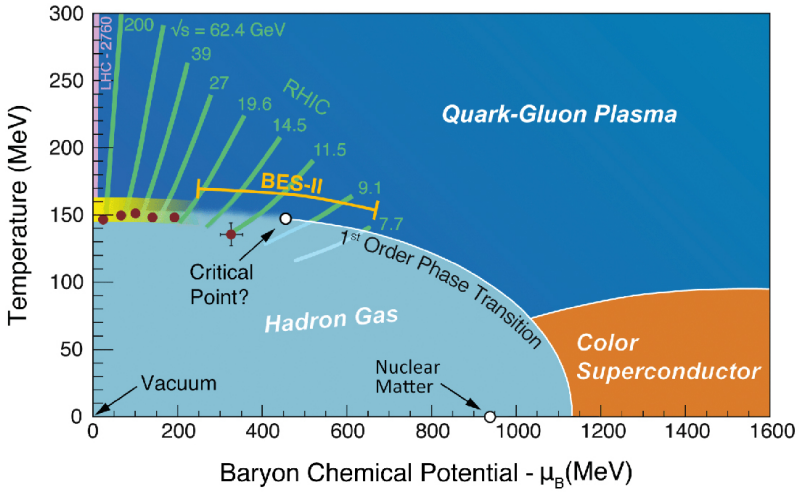

Figure 2: QCD phase diagram, taken from [25]. At low temperatures and low chemical potentials QCD matter exists in the form of hadrons due to the color confinement. At higher temperatures temperatures the quarks and gluons become deconfined, forming the so-called quark-gluon plasma. For small temperatures and large chemical potentials color superconductors are conjectured. The currently available experiments probing the QCD phase diagram at LHC and RHIC are indicated by the green and pink lines.

Returning to the currently accessible experiments probing the QCD phase diagram, I want to give a short overview of the collider experiments being carried out at RHIC and LHC in the following.

1.2. Collider Experiments

Currently there are two experimental facilities conducting heavy-ion collisions: The large hadron collider (LHC) located at the center for European nuclear research (CERN) in Geneva, Switzerland and the relativistic heavy-ion collider (RHIC) at the Brookhaven national laboratory (BNL) in Uptown, New York, USA.

The LHC is an accelerator consisting of a ring with approximately 9 km diameter, making it the largest accelerator in the world. The LHC, initially designed for searches for physics beyond the standard model, can accelerate protons up to a maximal center of mass energy of $\sqrt{s} = 14\,\text{TeV}$. Since 2010 the LHC also runs lead-lead collisions for a few weeks every year. These collisions were mainly done at $\sqrt{s} = 2.76\,\text{TeV}$ and $\sqrt{s} = 5.02\,\text{TeV}$ per nucleon pair. From the four large experiments located at the LHC, the ALICE collaboration's main focus lies on the heavy-ion collision program [26]. The ATLAS and CMS collaborations are also partly involved in the heavy-ion program. At the point of writing this document the LHC is conducting run 3, with further runs planned until 2041. These runs include proton-proton collisions, as well as lead-lead and oxygen-oxygen collisions.

The second accelerator facility RHIC, is a smaller accelerator with a diameter of 1.2 km. Contrary to the LHC, the main focus of RHIC is not to maximize the center of mass energy, but rather to be able to collide a multitude of different nuclei. Therefore, the maximal center of mass energy for proton collisions at RHIC is a bit lower than at LHC, sitting at $\sqrt{s} = 500\,\text{GeV}$. The maximal center of mass energy per nucleon pair at RHIC lies at $\sqrt{s} = 200\,\text{GeV}$. Since its commissioning in 2000 a multitude of species (Au, Ru, Zr, U, etc.) have been collided at RHIC. One important part of the physics program at RHIC, carried out by the two main experiments STAR and PHENIX, is the beam energy scan designed to study the QCD phase diagram [27]. For future research RHIC will be decommissioned and converted into the Electron-Ion Collider [28] by adding a new electron source, accelerators and storage rings to the existing infrastructure.

1.3. Short overview of a heavy-ion collision

In this section I want to give a short overview of the stages of a heavy-ion collision and introduce some of the necessary terminology and observables [2] for later.

[2] The term observable is used a bit loosly in this context and does not just refer to experimentally measurable quantities in the final state.

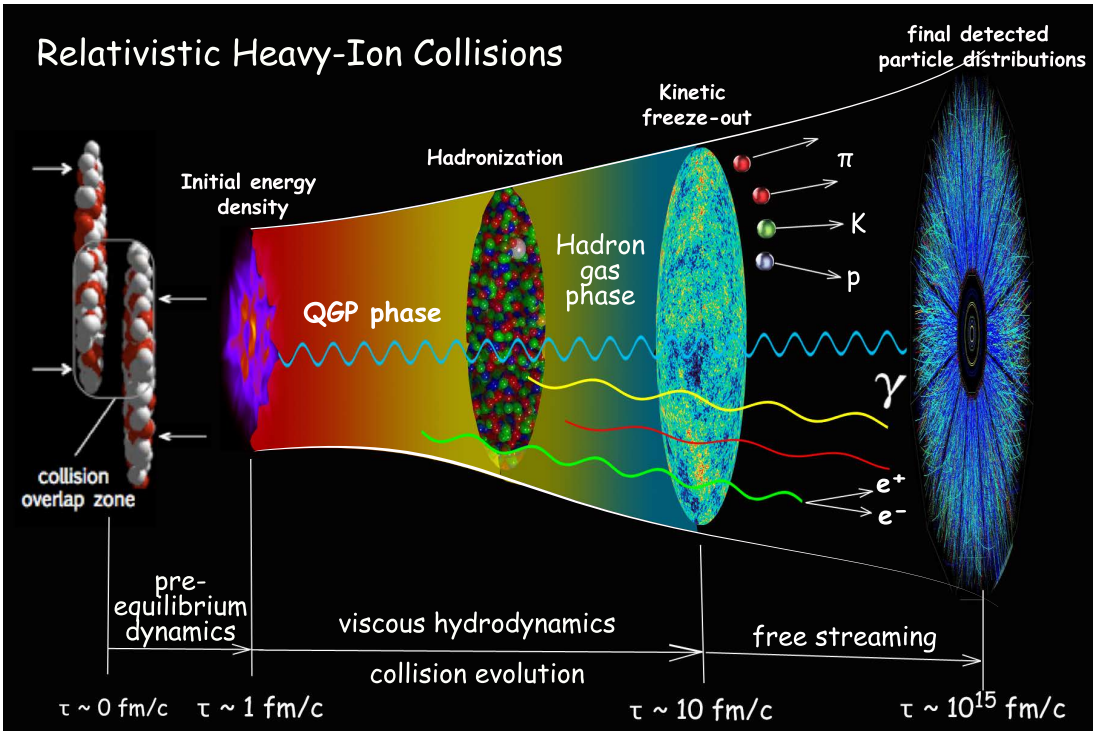

Figure 3: Schematic overview of a heavy-ion collision, taken from [29].

A schematic overview of a heavy-ion collision can be seen in fig. 3. For $\tau < 0$, i.e. before the collision, the two heavily Lorentz-contracted nuclei fly towards each other. During the collision at $\tau = 0$ a lot of energy is deposited at the collision site. After approximately 1 fm/c of the system thermalizing, the initial energy density of the QGP is created. This is also the point at which fluid-dynamic simulations are usually initialized. The system then undergoes a phase of rapid expansion, lasting roughly until $\tau \approx 10\,\text{fm/c}$. Due to the expansion of the system, the QGP cools down leading to confinement of the quarks and gluons of the plasma into hadrons. This process is also known as freeze-out. After the freeze-out, there is a short phase in which the hadrons are still dense enough to scatter among each other. With the ongoing expansion, the densities decrease resulting in free streaming hadrons. On their way to the detector hadrons may undergo decays until finally the produced particles are measured in a detector. An example of this is depicted on the far right.
Each of these phases comes with their own special features, models and observables. In the following I will give a short overview for each of the phases, including the descriptions, terms and observables most relevant for this work.

1.3.1. Before the collision & Initial state

Before the collision two nuclei fly towards each other along the beam pipe. In the following the coordinate system will always be chosen such that z-axis is aligned with the beam axis. Since the two nuclei travel at almost the speed of light, they are heavily Lorentz-contracted. During the collision, which is used to define

$\tau = 0$, a lot of energy is deposited at the collision point, defined to be at $z = 0$. For the description of the initial energy/entropy [3] there is a multitude of models available, with some of the most popular being the color glass condensate [30], Glauber models [31–33] and T$_\mathrm{R}$ENTo (Reduced Thickness Event-by-event Nuclear Topology) [34–36]. I will introduce the terminology and most important concepts for the initial state of a heavy-ion collision using the T$_\mathrm{R}$ENTo model, since it was used for this work. T$_\mathrm{R}$ENTo can be used to calculate a two-dimensional initial energy/entropy profile at $z = 0$, which is sufficient for the first part of this work. An extension for non-boost invariant initial conditions has been developed in [35, 36].
Since the exact position of the two each other approaching nuclei is impossible to control experimentally, they will hit each other with a random overlap. This overlap is quantified by the so-called impact parameter which is defined as the distance between the centers of the two nuclei. The orientation of the impact parameter in the x-y-plane defines the so-called reaction plane angle. If the two nuclei do not fully overlap, some of the nucleons inside the nuclei will collide with nucleons from the other nucleus, while other will pass the collision site without any interaction. The colliding nucleons are called participants, while the nucleons without any interaction are called spectators. In fig. 4 a sketch of a collision can be seen, where the participants are represented as filled circles while the spectators are empty circles. Additionally, the impact parameter has been marked.

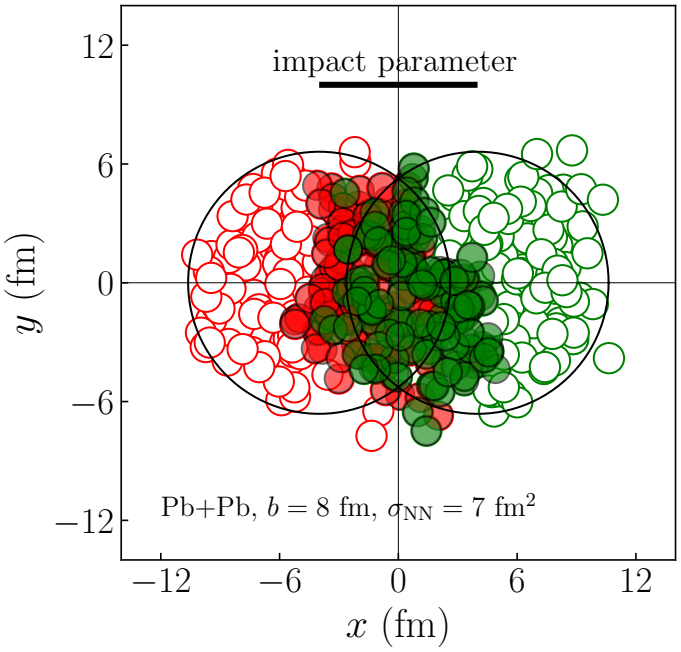

Figure 4: Sketch of the overlap during a heavy-ion collision, taken from [37]. The overlap is quantified by the so-called impact parameter (black line) which is defined as the distance between the two center of the nuclei. The colliding nucleons are called participants (filled circles), while the nucleons without any interaction are called spectators (empty circles).

[3] The concrete choice, if the initial profile is considered as entropy or energy depends on the model, with some models even interpolating between them.

The events with big/small overlap (i.e. small/big impact parameter) are often being referred to as central/peripheral events, respectively. Since the impact parameter is experimentally inaccessible, a different classification of events is used based on the number of produced particles:
In the experiment, the different events are sorted into centrality classes which are defined via the number of detected particles[4] in an event. Hereby, the events are sorted according to the number of produced particles. The $0-1\%$ centrality class is then defined as the 1% of events with the highest multiplicity, i.e. the highest number of produced particles. There is a loose relationship between the impact parameter and the multiplicity of an event. However, this relation gets washed out by fluctuations, leading to a different amount of energy being deposited in each nucleon-nucleon collision. A quantity including the fluctuations at fixed impact parameter is the total entropy of the initial profile, resulting in a stronger correlation with the final state multiplicity (see fig. 5). Similar correlations between "observables" in the initial state and observables in the final state can be found between the initial state eccentricity and the final state flow coefficients and the initial state energy and the average transverse momentum of the produced particles [37].

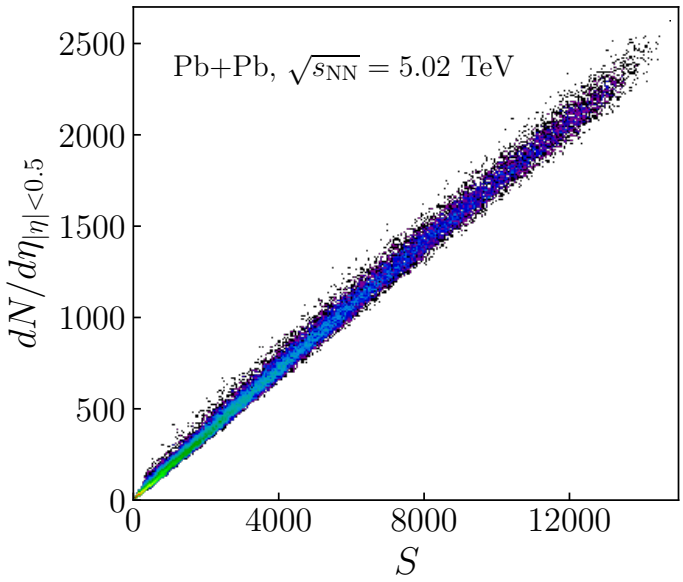

Figure 5: Correlation of the initial state entropy with the final state multiplicity, taken from [37]. The linear correlation between the two quantities is used in section 5 to establish a link to the nuclear structure parameters of the colliding nuclei.

To decide whether a collision takes place between two nucleons, a calculation for a nucleon to become wounded is carried out in T$_{\mathrm{R}}$ENTo based on the nucleon size, position and the collision energy. The position of the nucleons is sampled based on a Wood-Saxon distribution (see eq. 5.4), with the possibility to include a minimum nucleon-nucleon distance d. In this calculation several parameters enter, the main ones being the nucleon width w and the energy-dependent inelastic nucleon-nucleon cross section σ_{NN}, with modifications stemming from sub-nuclear constituents with width v and number m. Based on this

[4]Note that the terms produced and detected particles are used here as synonyms. However, in reality they can differ depending on the detector geometry and its efficiency.

probability, at each side of a wounded nucleon an amount of energy is deposited in form of a Gaussian with a fluctuating normalization which is sampled from a gamma-distribution with shape parameter k. This is being done for each nucleus individually resulting in two so-called thickness functions $\mathcal{T}_{A/B}$. These then get combined to obtain the reduced thickness $\mathcal{T}$, which then can be interpreted as energy or entropy density, via

$$\mathcal{T} \propto \left(\frac{\mathcal{T}_A^p + \mathcal{T}_B^p}{2} \right)^{1/p} . \tag{1.1}$$

The reduced thickness parameter p allows the definition of a generalized mean, which includes among others the geometric ($p = 0$), harmonic ($p = -1$) and arithmetic ($p = 1$) means.
Depending on the concrete model at hand, this reduced thickness function is either directly taken to be the energy or entropy density of the QGP or it is used as initial distribution for a subsequent thermalization process. In the first case the reduced thickness function is used as initial condition for fluid-dynamic evolution of the system. In the second case an additional pre-equilibrium phase describing the thermalization of the medium is assumed.

1.3.2. Pre-equilibrium and thermalization

The pre-equilibrium phase of a heavy-ion collision is thought to last until around 1 fm/c. In this time the system transitions from its out of equilibrium state right after the collision towards the QGP. The specific details of this thermalization procedure are object of current research (see [38] for a review). Therefore, in most fluid-dynamic simulations the pre-equilibrium phase is either omitted or replaced by a phase of free streaming [39]. During free streaming it is assumed that the initial energy/entropy density consists of non-interacting partons that evolve through free-streaming until approximately 1 fm/c and then undergo sudden equilibration.

1.3.3. Fluid dynamics

After the thermalization phase a radial expansion driven by the pressure gradients of the fluid sets in. This expansion leads to a cooling of the medium, resulting in the recombination of the quarks and gluons into hadrons due to confinement. This expansion lasts approximately from 1 fm/c to 10 fm/c. The exact duration of this expansion depends on the collision energy and geometry. More central collisions and collisions at higher energies tend to have larger and hotter fireballs leading to a longer QGP phase. During this phase the system can be described by the means of viscous fluid dynamics, which will be introduced in the next chapter. The main ingredients for this fluid-dynamic description are (besides the equations of motion) the equation of state and the transport coefficients. Both are directly linked to the underlying theory, describing the QGP (i.e. QCD) and their calculation is only possible to a limited extend from first principles. Therefore their determination is one of the goals of the heavy-ion research programs. Models for the fluid-dynamic description of the QGP are among others MUSIC [40–42], Trajectum [43] and Fluid$u$M [44], which will be

introduced in more detail in section 3.
An important experimentally accessible observable giving direct insight to the QGP dynamics and the initial state are electroweak probes, such as photons, leptons or W and Z bosons. Electroweak measurements are good probes for the early time dynamics of a heavy-ion collision, since they do not carry color charge and can even be used to constrain nuclear parton distribution functions (this is usually the case for probes with high momentum, since they are created during the hard scattering processes of the initial collision). On the other hand, soft electromagnetic probes, such as direct photons or leptons can be used to measure the temperature of the QGP fireball or its electrical conductivity.
Another important tool for gaining insights into the evolution of the QGP are hard probes in the form of heavy quarks. Since these heavy quarks have masses larger than the usual temperatures in the QGP, they are only created in the initial hard scatterings and are therefore part of the full evolution of the QGP. One of the main ways of studying heavy quarks is via the so-called nuclear modification factors R_{AA}, which are defined as

$$R_{AA} = \frac{1}{\langle N_{\text{coll}} \rangle} \frac{\mathrm{d}N_{AA}/\mathrm{d}p_{\mathrm{T}}}{\mathrm{d}\sigma_{pp}/\mathrm{d}p_{\mathrm{T}}}, \tag{1.2}$$

with $\mathrm{d}N_{AA}/\mathrm{d}p_{\mathrm{T}}$ and $\mathrm{d}\sigma_{pp}/\mathrm{d}p_{\mathrm{T}}$ being the hadron spectra in a heavy-ion and a proton-proton collision, respectively together with the number of binary collisions N_{coll} in the heavy-ion collision. Without any medium interactions within the QGP the nuclear modification factor would be unity, as a heavy-ion collision would just be a lot of individual proton-proton collisions. Therefore, deviations from unity are experimental evidence for the presence of the QGP and can be used to quantify the medium interactions.

1.3.4. Hadronization

During the expansion of the fireball the plasma cools down until eventually quarks and gluons are no longer free and recombine into hadrons. The collection of space-time points where the QGP freezes out and changes into hadrons is usually defined by the so-called freeze-out temperature T_{fo} and is called the freeze-out hypersurface. Because this recombination into hadrons is too complicated to describe from first principles it is modeled phenomenologically. The most popular model is the Cooper-Frye model where the spectrum of produced hadrons is calculated by integrating a distribution function f (depending on the fluid fields) over the freeze-out hypersurface Σ^{μ}

$$E\frac{\mathrm{d}N}{\mathrm{d}^3 p} \propto \int_{\Sigma} \mathrm{d}\Sigma^{\mu} p_{\mu} f. \tag{1.3}$$

After the creation of the hadrons, the system continues its expansion leading to a dilution until the hadrons become free streaming particles. However, shortly after their creation the hadrons are still abundant enough to scatter among each other. Since the temperatures and densities at this point are rather low, these scatterings are mostly elastic scatterings, keeping the system in kinetic, but not chemical equilibrium. One possibility of modeling this scattering phase is by the introduction of a phase of partial chemical equilibrium,

where the chemical and kinetic freeze-out occur at different temperatures [45, 46]. An alternative approach of modeling this hadronic scattering phase is via the use of codes such as UrQMD or SMASH [47, 48]. In section 4 I give a detailed discussion on how to calculate the final hadron spectra from the fluid fields on the freeze-out hypersurface, including resonance decays.
The final hadron spectra measured in the detectors are the fundamental result of the experimental efforts and are the basis for many observables. The central quantity here is the Lorentz-invariant particle yield

$$E\frac{\mathrm{d}N}{\mathrm{d}^3p} = \frac{1}{2\pi}\frac{\mathrm{d}^2N}{p_\mathrm{T}\mathrm{d}p_\mathrm{T}\mathrm{d}\eta_P}. \tag{1.4}$$

In an experiment the particle yield is reconstructed from tracks in the detector left by the particles. These measurements are done in momentum space, with the final object of the reconstruction being the particle's four-momentum $p^\mu = (p^0,\mathbf{p})$. The zeroth component of the momentum $p^0 = \gamma m$ is the rest mass m of the particle multiplied by the Lorentz factor γ. The spatial components are given by $\mathbf{p} = (p_x,p_y,p_z)$ in Cartesian coordinates. Due to the inherent geometry of the collision it is often very convenient to parameterize the momentum in terms of transverse momentum, azimuthal angle and rapidity (also often denoted by y) $\mathbf{p} = (p_\mathrm{T},\varphi,\eta_P)$, defined as

$$p_\mathrm{T} = \sqrt{p_x^2 + p_y^2}, \tag{1.5}$$

$$\varphi = \arctan(p_y/p_x), \tag{1.6}$$

$$\eta_P = \operatorname{arctanh}(p_z/p^0). \tag{1.7}$$

Since it is not always feasible to determine the particle species, the pseudo-rapidity $\eta_P' = \operatorname{arctanh}(z/t)$ is used when the particle species it not known. If the energy of the particle is much larger than its mass, its rapidity and pseudo-rapidity become the same. Usually the phenomena appearing in heavy-ion collisions are categorized in three categories, depending on the momentum they are measured at: Soft phenomena appearing for $p_\mathrm{T} \lesssim 2\,\mathrm{GeV}$. The majority of produced particles lies in this region making observables studied in this p_T-range ideal to examine the collective behavior of the system. Phenomena in the intermediate region of $2 \lesssim p_\mathrm{T} \lesssim 8\,\mathrm{GeV}$ are usually associated to the physics of heavy quarks and their interaction with the medium since they gain a bigger momentum during the expansion of the system due to their larger mass. The region of even larger transverse momentum $p_\mathrm{T} \gtrsim 8\,\mathrm{GeV}$ is mainly dominated by phenomena with hard scatterings, such as jets. Since fluid dynamics is mainly applicable in the soft sector, I will only give a short overview of the important observables of the soft sector: Since the fireball expands radially, the produced hadrons are not produced at rest, but get a boost from the radial fluid velocity. This boost is known as isotropic flow and scales with the mass of the hadron. Therefore, measuring the identified particle mean transverse momentum $\langle p_\mathrm{T}\rangle$ allows to extract information on the radial flow developed during the fluid evolution. On the other hand, anisotropic flow is related to the angular modulation of the particle

distribution function and is studied by looking at the so-called flow coefficients v_n, defined via

$$\frac{\mathrm{d}N}{\mathrm{d}\varphi} \propto \sum_{n=1}^{\infty} v_n \cos\left(n(\varphi - \Psi_{RP})\right). \tag{1.8}$$

Here φ is the azimuthal angle and Ψ_{RP} is the reaction plane angle, defined as the direction of the impact parameter in the transverse plane. These flow coefficient are very interesting to study for two main reasons: Firstly, they arise from the fluid-dynamic response of the QGP to the initial geometry of the collision. The main area of overlap of a non-central collision is roughly almond shaped. Therefore, the pressure gradients along the short direction of the medium are larger than along the long direction leading to an accelerated expansion, leading in turn to more produced particles. This response strongly depends on the equation of state and the viscosities of the system. Since the system reacts to its initial geometry, the dominant contribution is the reaction to the initial elliptic shape of the overlap region, given by the flow coefficient v_2. Secondly, higher odd flow coefficients, such as v_3 or v_5 are also interesting to study, since they are mainly driven by event-by-event fluctuations of the positions nucleons, giving access to the fluctuations of the initial state.

1.4. About this document

This thesis focuses on the description of heavy-ion collisions by the means of viscous relativistic fluid dynamics. In the first part I focus on the description of the QGP phase by fluid dynamics within the Fluid$u$M package. Additionally, I demonstrate how particle spectra including resonance decays can be calculated using the solutions to the fluid dynamic equations provided by Fluid$u$M. As conclusion of the first part, I present applications of the Fluid$u$M framework. The second part of this thesis is concerned with the extension of the fluid-dynamic description of heavy-ion collisions. Concretely, already the incoming nuclei are modeled as drops of nuclear matter whose dynamics are governed by the laws of fluid dynamics.

1.4.1. Outline

This thesis is structured as follows: First I give a short introduction into relativistic fluid dynamics in section 2, starting from non-relativistic ideal fluid dynamics. In section 3 I introduce the Fluid$u$M framework. Fluid$u$M is an efficient framework for the description of ultra-relativistic heavy-ion collisions based on mode-by-mode fluid dynamics. In section 4 I demonstrate how the particle spectra produced in a heavy-ion collision are calculated from fluid fields obtained in the previous chapter, including resonance decays. Afterwards, I illustrate the flexibility of the Fluid$u$M framework by presenting three applications in section 5: Firstly, I demonstrate how Fluid$u$M can be used to extract parameters of the QGP by Bayesian inference. The second application is related to the prediction of spectra needed for the analysis of direction photon data. For the third and final application Fluid$u$M was used for a parameter scan of nuclear structure parameters, comparing with the isobar Ru+Ru and Zr+Zr data collected at RHIC. Finally, I demonstrate how to extend the fluid-dynamic description of a heavy-ion collision to times before the collision in section 6. Possible

extensions of this work together with final remarks can be found in section 7.

1.4.2. Research work

This thesis is mainly based on the following publications:

1. A. Kirchner, E. Grossi, and S. Floerchinger, „Cooper-Frye spectra of hadrons with viscous corrections including feed down from resonance decays“, arXiv:2308.10616 (2023)
2. L. Vermunt et al., „Mapping QGP properties in Pb–Pb and Xe–Xe collisions at the LHC“, (2023)
3. A. Kirchner, K. Reygers, and A. Mazeliauskas, „Improved decay photon cocktail for direct photon analyses in nuclear collisions from hydrodynamic modeling of hadron spectra“, (arXiv, in progress)
4. A. Kirchner et al., „Extending the fluid description to times before the collision“, (arXiv, in progress)

Additionally, I present results obtained in the scope of the EMMI Rapid Reaction Task Force "Nuclear physics confronts relativistic collisions of isobars". This work was carried out together with Federica Capellino. The full results together with further results from the task force can be found in

G. e. a. Giacalone, „EMMI Rapid Reaction Task Force, Nuclear physics confronts relativistic collisions of isobars“, (arXiv, in preparation)

The results of these publications have been presented at the XXXth and XXIXth International Conference on Ultra-relativistic Nucleus-Nucleus Collisions and the workshop "Intersection of nuclear structure and high-energy nuclear collisions" at the Institute for Nuclear Theory, Seattle. Additional research I was involved in, but is not presented in this thesis can be found in:

1. F. Capellino et al., „Fluid-dynamics of charm quarks in the quark–gluon plasma“, arXiv:2307.14449 (2023)
2. F. Capellino et al., „Momentum distribution of charm hadrons in a fluid-dynamic approach“, arXiv:2307.15580 (2023)
3. M. Al Qahtani et al., „Anisotropic flow in ultracentral nucleus–nucleus collisions“, (arXiv, in preparation)

2. Relativistic fluid dynamics

This chapter is mostly inspired by [57–62] *and is intended as brief overview of the fluid dynamics needed for this thesis.*

2.1. Introduction to fluid dynamics

Fluid dynamics is one of the most general theories currently known in physics. It finds applications ranging from its initial perception as description of water to the description of galaxies [63–65] and ultra-cold atoms [66, 67]. This universal description can not only be found on these very different scales, but also when considering different materials and substances. When heated enough, all substances either become a liquid or a gas, sharing the same description in terms of fluid dynamics. The only remnant of the initial substance can be found in a few parameters such as the viscosities. This independence on the material taken into consideration exceeds the materials and their derivatives found in the periodic system. Even the quarks and gluons bound inside protons and neutrons can be described by fluid dynamics once temperatures are high enough to melt protons and neutrons.
The reasons for this universality appearing across different length and energy scales are well understood. Evidently the microscopic dynamics of these different systems are very different and complicated. However, when describing a large number of these microscopic degrees of freedom (order $\sim 10^{23}$), it is unfeasible to track each of these degrees individually. A more suitable description is based on the collective motion of the atoms or molecules in the fluid. It turns out, that this collective motion is governed by the guiding principles of conservation laws, namely the conservation of energy, momentum and mass.
As a first step I will discuss these conservation laws in a non-relativistic setting for an ideal fluid. Next, I will introduce dissipative effects into this non-relativistic description to account for non-ideal fluids. Since this thesis is mainly concerned with the physics of ultra-relativistic heavy-ion collisions, I will demonstrate how to transfer this description into a relativistic setting. Here dissipative terms have to be introduces with care to ensure a causal structure of the evolution equations.

2.1.1. Conservation laws and ideal fluid dynamics

A fluid-dynamic description is not concerned with tracking all individual degrees of freedom of a system, but focuses on its collective motion. This collective motion can be described using continuous fields, such as the fluid velocity $\mathbf{v}(t,x,y,z)$ which has to be understood as the velocity of an infinitesimal volume element of the fluid at space-time point (t,x,y,z) and not as velocity of a specific particle in the fluid. In the case of a description by means of individual particles, the knowledge of the position and momentum of each particle is sufficient. In the case of a fluid dynamic description the system can be fully described by the aforementioned

velocity field together with additional fields describing the thermodynamics of the system. Among these fields are the pressure $p(t,x,y,z)$ and the density $\rho(t,x,y,z)$ of the fluid, where local a thermal equilibrium is assumed for their definition. These thermodynamic quantities can be linked to the distribution function $f(\mathbf{x},\mathbf{p})$ of the individual particles [57]. In order to obtain equations of motion for these quantities, I employ the aforementioned guiding principles given by the conservation of mass, energy and momentum.

Conservation of mass The mass of the fluid inside a fluid cell with volume V is given by $\int \rho \mathrm{d}V$. The change of mass of this cell is given by the flux through the surface of the volume $\oint \rho \mathbf{v} \mathrm{d}\mathbf{n}$ per unit time step. Here the normal vector $\mathbf{n}$ of the volume is oriented such that the integrand is positive for a fluid streaming out of the volume. Therefore, the change in mass of the cell can be expressed as

$$\partial_t \int \rho \mathrm{d}V = - \oint \rho \mathbf{v} \mathrm{d}\mathbf{n}. \tag{2.1}$$

Using Gauß' integration theorem and demanding, that the equality holds for any volume, the conservation of mass can be written as the continuity equation

$$\partial_t \rho + \nabla \mathbf{j} = 0, \tag{2.2}$$

with the mass flux $\mathbf{j} = \rho \mathbf{v}$.

Conservation of momentum Similarly, it is possible to use the conservation of momentum given in Newton's second law to obtain another equation of motion. By integrating the pressure of the fluid over the surface of the volume, the force acting on this fluid cell is $-\nabla p$ per unit volume (in absence of external forces). Combining this with the conservation of momentum results in

$$\rho \frac{D\mathbf{v}}{Dt} = -\nabla p. \tag{2.3}$$

Here it is important to note, that the derivative denoted by D is the so-called material derivative $\frac{D\mathbf{v}}{Dt} = \partial_t \mathbf{v} + (\mathbf{v}\nabla)\mathbf{v}$, which is the change of velocity of a fluid element moving in the fluid, but not the change of the fluid velocity at one point in space. This change in velocity consists out of the change of the velocity in one point and the change of the velocity when moving through the fluid. This equation derived from the conservation of momentum is also known as Euler equation

$$\partial_t \mathbf{v} + (\mathbf{v}\nabla)\mathbf{v} = -\frac{1}{\rho}\nabla p. \tag{2.4}$$

In the presence of external forces, such as gravity, the right hand side is modified to account for these

$$\partial_t \mathbf{v} + (\mathbf{v}\nabla)\mathbf{v} = -\frac{1}{\rho}\nabla p + \mathbf{F}_{\mathrm{ext}}. \tag{2.5}$$

For future considerations, it is useful to combine the continuity equation and the Euler equation to

$$\partial_t(\rho v_i) = -\frac{\partial \Pi_{ik}}{\partial x_k}, \tag{2.6}$$

where the indices i and k run from one to three and summation over double indices is implied. Integration of this equation shows that the tensor $\Pi_{ik} = p\delta_{ik} + \rho v_i v_k$ can be interpreted as the flux of momentum component i in direction k.

Conservation of energy The final conservation law to employ is the conservation of energy, starting by considering an incompressible, stationary fluid moving between two cross sections A_1 and A_2 in a time interval Δt. The work done by the pressure acting on the cross sections A_i is $W_{\text{press}} = \frac{\Delta m}{\rho}(p_1 - p_2)$ with the displaced mass $\Delta m = \rho A_i v_i \Delta t$ ($i = 1,2$). The work done by gravity on the fluid is $W_{\text{grav}} = \Delta m g(z_1 - z_2)$. Therefore, the total work in absence of external forces, expect for gravity, is given by $W = W_{\text{press}} + W_{\text{grav}}$. Using the conservation of energy, this work is equal to the change in kinetic energy $W = \Delta E_{\text{kin}}$, given by $E_{\text{kin}} = \frac{1}{2}\Delta m(v_2^2 - v_1^2)$. Combining all of this yields the Bernoulli equation

$$\frac{1}{2}v_1^2 + gz_1 + \frac{p_1}{\rho} = \frac{1}{2}v_2^2 + gz_2 + \frac{p_2}{\rho} = const. \tag{2.7}$$

The expression for a dynamic energy flux can be obtained by considering the time derivative of the energy of one fluid cell

$$\partial_t \left(\rho \frac{v^2}{2} + \rho\epsilon\right), \tag{2.8}$$

taking ϵ to be the internal energy of the fluid per unit mass. Making use of the continuity equation eq. 2.2 and the Euler equation eq. 2.5, together with the thermodynamic differential of the canonical ensemble

$$\mathrm{d}\epsilon = T\mathrm{d}s + \frac{p}{\rho^2}\mathrm{d}\rho, \tag{2.9}$$

allows to obtain the time derivative of the energy flux as

$$\partial_t \left(\rho \frac{v^2}{2} + \rho\epsilon\right) = -\nabla \left(\rho \mathbf{v} \left(\frac{v^2}{2} + w\right)\right). \tag{2.10}$$

Note that the thermodynamic enthalpy $w = \epsilon + pV$ appears on the right hand side instead of the energy density. This can be understood by integrating both sides over an arbitrary volume and applying Gauss' theorem on the right hand side

$$\partial_t \int_V \left(\rho \frac{v^2}{2} + \rho\epsilon\right) \mathrm{d}V = \oint \left(\rho \mathbf{v} \left(\frac{v^2}{2} + w\right)\right) \mathrm{d}\mathbf{n}. \tag{2.11}$$

Therefore, the change in energy of the fluid is given by the energy flux through the surface of the volume, where the energy flux is defined with the enthalpy, not the energy. This can be understood by using $w = \epsilon + p/\rho$, which shows that the energy flux

$$\rho \mathbf{v} \left(\frac{v^2}{2} + w \right) = \rho \mathbf{v} \left(\frac{v^2}{2} + \epsilon \right) + \mathbf{v} p, \tag{2.12}$$

is given by the sum of the kinetic energy together with the pressure acting on the fluid.
The exact number of equations needed for a full description of the fluid is given by three, for the components of the fluid velocity, plus F, which is given by the thermodynamic degrees of the fluid. This can be calculated by the Gibbs phase rule $F = C - P + 2$ [68], where C is the number of components and P is the number of phases of the system. In the case of a single component fluid, which is only in its liquid phase, there are two thermodynamic degrees of freedom. Therefore, the ideal fluid has five degrees of freedom, which are fully described by the equations derived above from energy, momentum and mass conservation.
Although ideal fluid dynamics is a powerful tool capable of describing a multitude of systems as a good approximation[5], it has some obvious shortcomings. Since all of the derived equations above are invariant under time inversion, they will not be able to describe irreversible processes, such as the mixing of two fluids or dissipation processes. A more suitable description for this process is via non-ideal fluids where dissipative processes are captured by viscosities.

2.2. Dissipative effects

The viscosity of a fluid plays a crucial role in its dynamics, as can be observed by comparing the flow of water with the flow of honey. The viscosity of a fluid is related to the underlying, microscopic dynamics of the fluid governing the friction between its constituents. In order to add this internal friction to the fluid description, I will modify eq. 2.5 to account for this additional force. Since this force stems from the microscopic dynamics of the fluid, it will be a complicated function of the fluid velocity and its derivatives. Using the invariance of the fluid system under Galilean transformations, i.e. the boost of the whole system with a constant velocity, eliminates the dependence of the viscous term on the fluid velocity $\mathbf{v}$ itself. Therefore, the viscous terms can only be a function of derivatives of the fluid velocity. This is very intuitive, as the internal friction should be related to layers of the fluid "rubbing" against each other, requiring a non-vanishing gradient of the fluid velocity.
Writing the internal friction as expansion in derivatives of the fluid velocity, the appearing terms of lowest order are $\nabla \times \mathbf{v}$, $\nabla^2 \mathbf{v}$ and $\nabla(\nabla \mathbf{v})$. However, since the terms appearing in the Euler equation are all even under parity $\mathbf{x} \to -\mathbf{x}$, the lowest order candidate $\nabla \times \mathbf{v}$ is not suitable, since it is odd under parity. As I will show later, the remaining terms are related to the so-called shear and bulk viscosities of the fluid.
A more formal way of introducing these dissipative effects into the description is by reconsidering the

[5] Two famous examples are the explanation of the teapot effect and airspeed indicators, both based on the Bernoulli equation.

momentum flux tensor Π_{ik}. This can be done by expanding it beyond its ideal fluid form to

$$\Pi_{ik} = p\delta_{ik} + \rho v_i v_k - \sigma'_{ik} = -\sigma_{ik} + \rho v_i v_k. \tag{2.13}$$

The additional term σ_{ik} or σ'_{ik} is known as stress tensor and viscous stress tensor. The concrete form of σ'_{ik} can be obtained by similar considerations as before.
Assuming, that the derivatives of the fluid velocity are small enough, it is possible to truncate the expansion of the stress tensor at first order in fluid velocity derivatives. Since a fully rotating fluid has no internal friction, the most general form for the stress tensor is given by

$$\sigma_{ik} = \eta \left(\frac{\partial v_i}{\partial x_k} + \frac{\partial v_k}{\partial x_i} - \frac{2}{3}\delta_{ik}\frac{\partial v_l}{\partial x_l} \right) + \zeta \delta_{ik} \frac{\partial v_l}{\partial x_l}. \tag{2.14}$$

The coefficients η and ζ are known as shear and bulk viscosities and are independent of the fluid velocity. Adding the spatial derivative of this expansion to the right hand side of the Euler equation, yields the so-called Navier-Stokes equation

$$\rho \left(\partial_t \mathbf{v} + (\mathbf{v}\nabla)\mathbf{v} \right) = -\nabla p + \eta \Delta \mathbf{v} + \left(\zeta + \frac{\eta}{3} \right) \nabla(\nabla \mathbf{v}). \tag{2.15}$$

So far only gradients in the fluid velocity have been considered. However, also gradients of thermodynamic quantities may arise. One example are gradients in the temperature leading to heat transport. Note that heat transport is related to collisions on a constituent level of the fluid and occurs in the presence of temperature gradients, even in a fluid that is not moving macroscopically. Taking the viscous effects discussed before and the heat flux into account, the energy flux of the fluid reads as

$$\rho \mathbf{v} \left(\frac{v^2}{2} + w \right) - \mathbf{v}\sigma' - \kappa \nabla T, \tag{2.16}$$

where the coefficient κ is being introduced as the heat conductivity. The change in energy of a fluid cell is then

$$\partial_t \left(\rho \frac{v^2}{2} + \rho \epsilon \right) = -\nabla \left(\rho \mathbf{v} \left(\frac{v^2}{2} + w \right) - \mathbf{v}\sigma' - \kappa \nabla T \right). \tag{2.17}$$

A more intuitive form of this equation can be obtained by making use of the thermodynamic differentials, the continuity equation eq. 2.2 and the Navier-Stokes equation eq. 2.15

$$\rho T \left(\partial_t s + \mathbf{v}\nabla s \right) = \sigma'_{ik} \frac{\partial v_i}{\partial x_k} + \nabla(\kappa \nabla T). \tag{2.18}$$

Reconsidering an ideal fluid without viscosities, the right hand side vanishes, resulting in the equation for entropy conservation. In case of non-vanishing viscosities, the expression $\rho T \partial_t s$ is the change in heat of the fluid cell. From eq. 2.18 it becomes evident that this change in heat comes either from energy being

converted to heat through the viscosity (first term) or from a heat flux flowing into the fluid cell (second term).
In general the viscosities have to be obtained from a microscopic theory, describing the underlying physics of the constituents of the fluid. However, using the laws of thermodynamics it is possible to constrain the values of the viscosities. Since the fluid taken into consideration is a viscous one, its evolution is irreversible and the total entropy of the system has to grow

$$\partial_t \int s\rho \mathrm{d}V \geq 0. \tag{2.19}$$

Using the previously derived equations, the change in total entropy can be expressed as

$$\partial_t \int s\rho \mathrm{d}V = \int \frac{\kappa(\nabla T)^2}{T^2} + \frac{\eta}{2T}\left(\frac{\partial v_i}{\partial x_k} + \frac{\partial v_k}{\partial x_i} - \frac{2}{3}\delta_{ik}\frac{\partial v_l}{\partial x_l}\right)^2 + \frac{\zeta}{T}(\nabla \mathbf{v})^2 \mathrm{d}V. \tag{2.20}$$

To ensure that the entropy production is positive for all possible configurations of the fluid, each term has to be larger than zero individually, which is fulfilled when all the entropies are larger than zero $\eta, \zeta\ \kappa \geq 0$.
This set of equations derived for viscous fluids has a large range of applications ranging from meteorology to CFD simulations for vehicle design [69–71] and the simulation of various phenomena in video games such as smoke and fire [72]. The importance of the Navier-Stokes equation also becomes evident when considering that one of the, so far unsolved, Millenium problems posed by the Clay Mathematics Institute is related to the existence of solutions to the Navier-Stokes equation [73]. However, since I want to focus on the description of ultra-relativistic heavy-ion collisions with fluid dynamics, a relativistic covariant fluid description is needed. I will derive this relativistic description in the next chapter, taking similar steps as before by starting with an ideal, relativistic fluid.

2.3. Relativistic fluid dynamics

Similarly to its non-relativistic counterpart, relativistic fluid dynamics is also build on conservation laws and the assumption of local thermal equilibrium. The local thermal equilibrium allows to introduce a temperature $T(x)$, a chemical potential $\mu(x)$ and a fluid four-velocity $u^\mu(x)$ at each space-time point $x = x^\mu$. Note that the fluid four-velocity is defined as derivative with respect to the proper time $u^\mu(x) = \frac{\mathrm{d}x^\mu}{\mathrm{d}\tau}$. Using the relation $\mathrm{d}\tau^2 = \mathrm{d}t^2/\gamma^2$ between the proper time and the coordinate time, the fluid velocity can be expressed as $u^\mu(x) = \frac{\mathrm{d}t}{\mathrm{d}\tau}\frac{\mathrm{d}x^\mu}{\mathrm{d}t} = \gamma(1, \mathbf{v})^T$. An important consequence of this is that the four-velocity only has three independent components

$$u^\mu u_\mu = -\gamma^2(1 - \mathbf{v}^2) = -1. \tag{2.21}$$

The conservation of energy, momentum and particle number is now expressed with help of the energy-momentum tensor $T^{\mu\nu}$ and the particle current N^{μ}:

$$\nabla_{\mu} N^{\mu} = 0, \tag{2.22}$$

$$\nabla_{\mu} T^{\mu\nu} = 0. \tag{2.23}$$

To obtain a usable description of the relativistic system, concrete expressions for the energy-momentum tensor and particle current in terms of the fluid fields are needed. Generally speaking, there are two main ways of obtaining the concrete expressions. The first possibility is a more formal one based on the general decomposition of the tensors $T^{\mu\nu}$ and N^{μ}, where all the individual components are immediately present. The second possibility is to start with the simplest case, derived from assumptions, and include the remaining terms accounting for more complex dynamics later. For now I will use the second method, allowing for an easier derivation of the equations. In a later part of this work, the more formal first method is used to recover the fluid fields from a general energy-momentum tensor.

2.3.1. Ideal relativistic fluid dynamics

In order to determine the form of the energy-momentum tensor and the particle current, I start in the local rest frame of the ideal fluid. In this local rest frame the fluid is in static equilibrium, i.e. the spatial velocity vanishes $\mathbf{v} = 0$. Since the energy-momentum tensor $T^{\mu\nu}_{\text{id}}$ gives the flow of the μ-momentum in ν-direction and the system is isotropic and without flow of energy, the only non-zero components of $T^{\mu\nu}_{\text{id}}$ can be on the diagonal. The spatial isotropy of the fluid requires that the spatial components on the diagonal of the energy-momentum tensor are the same. Since the $T^{\mu 0}$ components are related to the flux of energy, the energy-momentum tensor in the local rest frame takes the form

$$T^{\mu\nu}_{\text{id}} = \begin{pmatrix} \epsilon & 0 & 0 & 0 \\ 0 & p & 0 & 0 \\ 0 & 0 & p & 0 \\ 0 & 0 & 0 & p \end{pmatrix}, \tag{2.24}$$

where ϵ is the energy and p the thermodynamic pressure. Similarly, the lack of spatial particle number currents gives the form of the particle current as

$$N^{\mu}_{\text{id}} = \begin{pmatrix} n \\ 0 \\ 0 \\ 0 \end{pmatrix}, \tag{2.25}$$

with n being the particle number. In a general frame the energy-momentum tensor and particle number current can be expressed as

$$T^{\mu\nu}_{\text{id}} = c_1 u^\mu u^\nu + c_2 g^{\mu\nu}, \tag{2.26}$$

$$N^{\mu}_{\text{id}} = c_3 u^\mu, \tag{2.27}$$

taking their respective transformation behaviors into account. The coefficients c_i can be obtained by matching the general expression for the case of $\mathbf{v} = 0$ with eq. 2.24 and eq. 2.25, yielding

$$T^{\mu\nu}_{\text{id}} = \epsilon u^\mu u^\nu + p\Delta^{\mu\nu}, \tag{2.28}$$

$$N^{\mu}_{\text{id}} = n u^\mu, \tag{2.29}$$

with $\Delta^{\mu\nu} = u^\mu u^\nu + g^{\mu\nu}$ being the projector orthogonal to the fluid velocity. Applying this to the equations of motion eq. 2.22 and eq. 2.23 yields

$$D\epsilon + (\epsilon + p)\theta = 0, \tag{2.30a}$$

$$(\epsilon + p)Du^\mu + \Delta^{\mu\nu}\partial_\nu p = 0, \tag{2.30b}$$

$$Dn + n\theta = 0. \tag{2.30c}$$

The first two equations are obtained from the energy-momentum conservation by taking the projections parallel and orthogonal to the fluid velocity. Here I introduced the comoving derivative $D = u^\mu \partial_\mu$ and $\theta = \nabla_\mu u^\mu$.

Note that similar to the non-relativistic case, this system of equations is not closed. Although the fluid velocity u^μ is a four-vector, it still has only three independent components due to the normalization condition $u_\mu u^\mu = -1$. In contrast to the previous case, I introduced a chemical potential μ together with the corresponding number density n, which increases the number of phases in the fluid by one (corresponding to the conjugated charge and its anti-charge). Therefore, the system has three thermodynamic degrees of freedom, the energy ϵ, the pressure p and the number density n. In order to close the system of five independent equations eq. 2.30, an equation of state $p = p(\epsilon,n)$ linking the thermodynamic quantities is needed.

Lastly, I shortly examine the entropy current in the relativistic setting. The covariant version of Euler's relation $\epsilon + p = Ts + \mu n$ is given by

$$S^\mu = p\beta^\mu + \beta_\nu T^{\mu\nu}_{\text{id}} - \alpha N^{\mu}_{\text{id}}, \tag{2.31}$$

with $\alpha = \frac{\mu}{T}$ and $\beta^\mu = \frac{u^\mu}{T}$. Using the first law of thermodynamics, the divergence of the entropy current reads

$$\nabla_\mu S^\mu = \beta_\nu \nabla_\mu T^{\mu\nu}_{\text{id}} - \alpha \nabla_\mu N^{\mu}_{\text{id}}. \tag{2.32}$$

Applying the previously established conservation laws for energy, momentum and particle number, it is immediately evident that the entropy is conserved $\nabla_\mu S^\mu = 0$, as it was in the non-relativistic case. The equation of motion for the entropy $Ds + s\theta = 0$ is identical to the one of the particle number density eq. 2.30c, which implies that the entropy per particle s/n is a constant of motion. Next I will take dissipative effects into account by including gradient terms of the fluid dynamic variables.

2.3.2. First order dissipative fluid dynamics

Keeping the aim of this work to describe ultra-relativistic heavy-ion collisions with fluid dynamics in mind, it seems unreasonable to expect ideal fluid dynamics being the correct way of treating this rapidly expanding system, due its fundamental assumption of local thermal equilibrium. The expansion of the system will lead to fluid cells not in thermodynamic equilibrium with their neighbors, as well as to relative motion of neighboring fluid cells. As in the non-relativistic case, this leads to a heat flux producing entropy and the dissipation of energy through friction between fluid cells. The dynamics of such a viscous fluid is obviously still governed by energy-momentum (eq. 2.23) and particle number (eq. 2.22) conservation. However, the form of the energy-momentum tensor and of the particle number current will not be the same as given in eq. 2.28 and eq. 2.29. When deriving the form of these quantities in the ideal setting, the isotropy of the system together with the lack of energy and particle fluxes was used to simplify the expressions. However, in general a four-vector and a two-tensor can have more components. To account for these additional terms, the energy-momentum tensor and particle number current are written as

$$T^{\mu\nu} = T^{\mu\nu}_{\text{id}} + \tau^{\mu\nu} = \epsilon u^\mu u^\nu + p\Delta^{\mu\nu} + \tau^{\mu\nu}, \tag{2.33}$$

$$N^\mu = N^\mu_{\text{id}} + \nu^\mu = n u^\mu + \nu^\mu, \tag{2.34}$$

introducing the dissipative currents $\tau^{\mu\nu}$ and ν^μ. So far the only constrain on the form of these currents is the symmetry of the energy-momentum tensor, requiring $\tau^{\mu\nu} = \tau^{\nu\mu}$. Note that the introduction of these dissipative currents makes the definition of the thermodynamic quantities ϵ and n a bit more subtle:
Since the fluid is no longer necessarily in equilibrium, the thermodynamic variables are ill-defined. To remedy this, I construct an artificial equilibrium state, such that the usual thermodynamic relations are valid. I define the equilibrium state via the energy and the number density, which are defined by so-called matching conditions

$$\epsilon = u_\mu u_\nu T^{\mu\nu} \qquad \text{and} \qquad n = -u_\mu N^\mu. \tag{2.35}$$

These matching conditions already put additional constraints on the dissipative currents

$$u_\mu u_\nu \tau^{\mu\nu} = 0 \qquad \text{and} \qquad u_\mu \nu^\mu = 0. \tag{2.36}$$

This reduces the degrees of freedom in the dissipative currents, but is not enough to fully determine them. To fix the final components it is convenient to expand the currents in their irreducible components which

are a scalar, a four-vector and a traceless, symmetric rank two tensor. The decomposition for $\tau^{\mu\nu}$ is given by

$$\tau^{\mu\nu} = \Pi\Delta^{\mu\nu} + 2u^{(\mu}h^{\nu)} + \pi^{\mu\nu}, \tag{2.37}$$

with the definitions

$$\Pi = -\frac{1}{3}\Delta_{\alpha\beta}\tau^{\alpha\beta}, \quad h^{\mu} = \Delta^{\mu}_{\alpha}u_{\beta}\tau^{\alpha\beta} \quad \text{and} \quad \pi^{\mu\nu} = \Delta^{\mu\nu}_{\alpha\beta}\tau^{\alpha\beta}. \tag{2.38}$$

These newly introduced fields are known as the bulk viscous pressure Π, the energy diffusion current h^{μ} and the shear stress tensor $\pi^{\mu\nu}$. The projector used for the definition of the shear stress tensor is given by $\Delta^{\mu\nu}_{\alpha\beta} = \frac{1}{2}\Delta^{\mu}_{\alpha}\Delta^{\nu}_{\beta} + \frac{1}{2}\Delta^{\mu}_{\beta}\Delta^{\nu}_{\alpha} - \frac{2}{3}\Delta^{\mu\nu}\Delta_{\alpha\beta}$ and gives the projection of a two tensor orthogonal to the fluid velocity u^{μ}. With this the natural question of the definition of the fluid velocity arises.
In the case of ideal fluid dynamics, the fluid velocity was defined uniquely via the rest frame with vanishing energy and particle flow. In the case of a viscous fluid this definition is no longer applicable due the presence of energy and particle diffusion. There are two natural choices for the fluid velocity by either using a frame with vanishing particle or vanishing energy flow. The first choice is also known as Eckart definition [74], where

$$N^{\mu} = nu^{\mu} \to \nu^{\mu} = 0. \tag{2.39}$$

The second choice is the so called Landau definition [58]

$$u_{\mu}T^{\mu\nu} = -\epsilon u^{\nu} \to h^{\mu} = 0. \tag{2.40}$$

In the following I will use the Landau definition. With this decomposition the energy-momentum tensor and particle current can be expressed as

$$T^{\mu\nu} = \epsilon u^{\mu}u^{\nu} + (p + \Pi)\Delta^{\mu\mu} + \pi^{\mu\nu}, \tag{2.41}$$

$$N^{\mu} = nu^{\mu} + \nu^{\mu}. \tag{2.42}$$

As stated in the beginning of the chapter, energy-momentum conservation and particle number conservation are still valid for a viscous fluid, resulting in the following equations of motion

$$D\epsilon + (\epsilon + p + \Pi)\theta + \pi^{\mu}_{\nu}\nabla_{\mu}u^{\nu} = 0, \tag{2.43a}$$

$$(\epsilon + p + \Pi)Du^{\mu} + \Delta^{\mu\nu}\partial_{\nu}(p + \Pi) + \Delta^{\mu\nu}\nabla_{\rho}\pi^{\rho}_{\nu} = 0, \tag{2.43b}$$

$$Dn + n\theta + \nabla_{\mu}\nu^{\mu} = 0. \tag{2.43c}$$

Counting the degrees of freedom in this theory gives five from the ideal fluid dynamic part (three from the fluid velocity plus two from energy, pressure and number density, with the equation of state linking those),

one from the bulk pressure, three from the diffusion current (using $u_\mu \nu^\mu = 0$) and five from the shear stress tensor (using $\pi^{\mu\nu} = \pi^{\nu\mu}$, $\pi^\mu_\mu = 0$ and $u_\mu \pi^{\mu\nu} = 0$), totaling fourteen. As consequence, this system of five equations eq. 2.43 is not a closed system. To remedy this equations of motion for the dissipative currents are needed.

To derive these equations, I will return to the entropy current. Since the fluid is no longer ideal and dissipative effects play a role, the entropy is no longer conserved $\nabla_\mu S^\mu \neq 0$. Generalizing the entropy current eq. 2.31 to the dissipative setting

$$S^\mu = p\beta^\mu + \beta_\nu T^{\mu\nu} - \alpha N^\mu, \tag{2.44}$$

allows the application of the dissipative forms of the energy-momentum tensor eq. 2.41 and particle current eq. 2.42. The entropy production in this dissipative setting is then given by

$$\nabla_\mu S^\mu = -\beta \Pi \theta - n^\mu \nabla_\mu \alpha + \beta \pi^{\mu\nu} \sigma_{\mu\nu}, \tag{2.45}$$

with the symmetric combination $\sigma^{\mu\nu} = \Delta^{\mu\nu}_{\alpha\beta} \nabla^\alpha u^\beta$ of the fluid velocity gradient. To fulfill the second law of thermodynamics, the entropy production needs to obey $\nabla_\mu S^\mu \geq 0$, i.e.

$$-\beta \Pi \theta - n^\mu \nabla_\mu \alpha + \beta \pi^{\mu\nu} \sigma_{\mu\nu} \geq 0. \tag{2.46}$$

To fulfill this inequality for every possible fluid configuration, each individual term needs to be positive. This leads to

$$\Pi = -\zeta \theta, \tag{2.47a}$$

$$\nu^\mu = -\kappa \nabla^\mu \alpha, \tag{2.47b}$$

$$\pi^{\mu\nu} = 2\eta \sigma_{\mu\nu}. \tag{2.47c}$$

The proportionality coefficients ζ, κ and η are known as bulk viscosity, particle diffusion and shear viscosity, respectively. Similar to the non-relativistic case, the dissipative fields are directly proportional to gradients of the fluid velocity, temperature and chemical potential. Applying these relations, the entropy production now reads

$$\nabla_\mu S^\mu = \frac{\beta}{\zeta} \Pi^2 + \frac{1}{\kappa} \nu_\mu \nu^\mu + \frac{\beta}{2\eta} \pi^{\mu\nu} \pi_{\mu\nu}. \tag{2.48}$$

Since the temperature is always a positive number and the bulk pressure is a real number, the first term is larger than zero, given $\zeta \geq 0$. Seeing that the diffusion current ν^μ is orthogonal to the fluid velocity and using that the fluid velocity $u_\mu u^\mu = -1$ is time-like, the diffusion current is a space-like vector $\nu_\mu \nu^\mu > 0$. If $\kappa > 0$, the second term is positive as well. Using that the eigenvalues of a real, symmetric matrix are real and that the trace of the square of a symmetric matrix is given by the sum of the squared eigenvalues, the

contribution of the shear stress is positive $\pi^{\mu\nu}\pi_{\mu\nu} \geq 0$. Combining this with a positive shear viscosity $\eta > 0$, the final contribution to the entropy production is also positive. This ensures a positive entropy production $\nabla_\mu S^\mu \geq 0$ for all possible fluid configurations. The constituent relations eq. 2.47 together with the equations eq. 2.43, derived from energy-momentum and particle number conservation, are the closed set of relativistic Navier-Stokes equations. Even if now fully closed, this set of equations is not a suitable description for a relativistic fluid, because it violates causality and is unstable [57]. The source of the acausality can be found in the constituent relations eq. 2.47. Any change in the chemical potential or in the fluid velocity will lead to an immediate change in the viscous fields. This immediate change allows waves to propagate faster than the speed of light, which is forbidden in any relativistic theory. A number of different theories [75–79] were developed to ensure causality together with the second law of thermodynamics. In the next section I will shortly present the Ansatz first introduced by Israel and Stewart [62], which will be used in the rest of this work.

2.3.3. Second order dissipative fluid dynamics

The constituent relations for the dissipative fields derived in the previous chapter were direct proportionalities to the gradients of the ideal fluid fields temperature, chemical potential and fluid velocity. The main idea of the Israel-Stewart theory is to generalize these relations by allowing higher order terms in the gradients of the ideal fluid fields. In the most general setting the entropy four-current does not only depend on the higher order terms of the ideal fluid fields, but also on the dissipative currents

$$S^\mu = p\beta^\mu + \beta_\nu T^{\mu\nu} - \alpha N^\mu - Q^\mu\left(\delta N^\mu, \delta T^{\mu\nu}\right). \tag{2.49}$$

Here the four vector Q^μ is a function of the deviations from local equilibrium of the particle current $\delta N^\mu = N^\mu - N^\mu_{\text{id}}$ and energy-momentum tensor $\delta T^{\mu\nu} = T^{\mu\nu} - T^{\mu\nu}_{\text{id}}$. In order to obtain the concrete form for the deviations from equilibrium, Israel and Stewart employed a Taylor-expansion one order beyond the relativistic Navier-Stokes theory, i.e. to second order. The entropy current up to second order in the dissipative terms is then given by

$$S^\mu = su^\mu + \alpha\nu^\mu - \left(\beta_0\Pi^2 + \beta_1\nu_\alpha\nu^\alpha + \beta_2\pi_{\alpha\beta}\pi^{\alpha\beta}\right)\frac{u^\mu}{2T} - \left(\alpha_0\Pi\Delta^{\mu\alpha} + \alpha_1\pi^{\mu\alpha}\right)\frac{\nu_\alpha}{T} + \mathcal{O}(\delta^3), \tag{2.50}$$

where β_0, β_1, β_2, α_0 and α_1 are the coefficients of the Taylor-expansion. In general these coefficients are complicated functions of the chemical potential and the temperature. Naturally, this form of the entropy current will give more complicated constituent relations for the dissipative currents. To obtain these relations, the

entropy production is considered, as before

$$\begin{aligned}\nabla_\mu S^\mu = &-\beta\Pi\left(\theta+\beta_0\dot{\Pi}+\beta_{\Pi\Pi}\Pi\theta+\psi\alpha_{n\Pi}\nu_\mu\dot{u}^\mu+\alpha_0\nabla_\mu\nu^\mu+\psi\alpha_{\Pi n}\nu_\mu\nabla^\mu\alpha\right)\\ &-\beta\nu^\mu\left(T\nabla_\mu\alpha-\beta_1\dot{\nu}^\mu-\beta_{nn}\nu_\mu\theta+\alpha_0\nabla_\mu\Pi+\alpha_1\nabla_\alpha\pi^\alpha_\mu+\tilde{\psi}\alpha_{n\Pi}\Pi\dot{u}_\mu\right.\\ &\qquad\left.+\tilde{\psi}\alpha_{\Pi n}\Pi\nabla_\mu\alpha+\tilde{\chi}\alpha_{\pi n}\pi^\alpha_\mu\nabla_\alpha\alpha+\tilde{\chi}\alpha_{n\pi}\pi^\alpha_\mu\dot{u}_\alpha\right)\\ &+\beta\pi^{\alpha\beta}\left(\sigma_{\alpha\beta}-\beta_2\dot{\pi}_{\alpha\beta}-\beta_{\pi\pi}\theta\pi_{\alpha\beta}-\alpha_1\nabla_{\langle\alpha}\nu_{\beta\rangle}-\chi\alpha_{\pi n}\nu_{\langle\alpha}\nu_{\beta\rangle}\alpha-\chi\alpha_{n\pi}\nu_{\langle\alpha}\dot{u}_{\nu\rangle}\right).\end{aligned}\tag{2.51}$$

In their seminal work Israel and Stewart defined constituent relations that ensure a positive entropy production

$$\Pi=-\zeta\left(\theta+\beta\dot{\Pi}+\beta_{\Pi\Pi}\Pi\theta+\alpha_0\nabla_\mu\nu^\mu+\psi\alpha_{n\Pi}\nu_\mu\dot{u}^\mu+\psi\alpha_{\Pi n}\nu_\mu\nabla^\mu\alpha\right),\tag{2.52}$$

$$\nu^\mu=\frac{\kappa}{T}\left(T\nabla^\mu\alpha-\beta_1\dot{\nu}^{\langle\mu\rangle}-\beta_{nn}\nu^\mu\theta+\tilde{\psi}\alpha_{\Pi n}\Pi\nabla^\mu\alpha+\tilde{\chi}\alpha_{\pi n}\pi^\mu_\alpha\nabla^\alpha\alpha+\tilde{\chi}\alpha_{n\pi}\pi^\mu_\alpha\dot{u}^\alpha+\alpha_0\nabla^\mu\Pi+\alpha_1\Delta^\mu_\alpha\nabla_\beta\pi^{\alpha\beta}\right),\tag{2.53}$$

$$\pi^{\mu\nu}=2\eta\left(\sigma^{\mu\nu}-\beta_2\dot{\pi}^{\langle\mu\nu\rangle}-\beta_{\pi\pi}\theta\pi^{\mu\nu}-\alpha_1\nabla^{\langle\mu}\nu^{\nu\rangle}-\chi\alpha_{\pi n}\nu^{\langle\mu}\nabla^{\nu\rangle}\alpha-\chi\alpha_{n\pi}\nu^{\langle\mu}\dot{u}^{\nu\rangle}\right).\tag{2.54}$$

From these relations one can derive equations of motion for the dissipative currents, given by

$$\dot{\Pi}+\frac{\Pi}{\tau_\Pi}=-\frac{1}{\beta_0}\left[\theta+\beta_{\Pi\Pi}\Pi\theta+\psi\alpha_{n\Pi}n_\mu\dot{u}^\mu+\alpha_0\nabla_\mu n^\mu+\psi\alpha_{\Pi n}n_\mu\nabla^\mu\alpha\right],\tag{2.55}$$

$$\begin{aligned}\dot{\nu}^\mu+\frac{\nu^\mu}{\tau_n}=\frac{1}{\beta_1}\Big[&T\nabla^\mu\alpha-\beta_{nn}n^\mu\theta+\alpha_1\Delta^\mu_\rho\nabla_\nu\pi^{\rho\nu}+\alpha_0\nabla^\mu\Pi+\tilde{\psi}\alpha_{n\Pi}\Pi\dot{u}^\mu\\ &+\tilde{\psi}\alpha_{\Pi n}\Pi\nabla^\mu\alpha+\tilde{\chi}\alpha_{\pi n}\pi^\mu_\nu\nabla^\nu\alpha+\tilde{\chi}\alpha_{n\pi}\pi^\mu_\nu\dot{u}^\nu\Big],\end{aligned}\tag{2.56}$$

$$\dot{\pi}^{\langle\mu\nu\rangle}+\frac{\pi^{\mu\nu}}{\tau_\pi}=\frac{1}{\beta_2}\left[\sigma^{\mu\nu}-\beta_{\pi\pi}\theta\pi^{\mu\nu}-\alpha_1\nabla^{\langle\mu}n^{\nu\rangle}-\chi\alpha_{\pi n}n^{\langle\mu}\nabla^{\nu\rangle}\alpha-\chi\alpha_{n\pi}n^{\langle\mu}\dot{u}^{\nu\rangle}\right].\tag{2.57}$$

This type of equations is known as relaxation type equations with the relaxation times defined as

$$\tau_\Pi=\zeta\beta_0,\tag{2.58}$$

$$\tau_n=\frac{\kappa\beta_1}{T},\tag{2.59}$$

$$\tau_\pi=2\eta\beta_2.\tag{2.60}$$

These relaxation times are the most important difference to the previously derived relativistic Navier-Stokes theory. They introduce a characteristic time scale within which the dissipative currents react to gradients in the system. In the previous case this reaction was instantaneous, violating causality. However, this gain of causality comes at the cost of additional parameters β_i and α_j. Similar to the viscosities they cannot be determined self-consistently from fluid dynamics and rely on a determination by other means such as kinetic theory.

Note that the equations derived above were obtained by Taylor-expanding the perturbations around equi-

librium up to second order in dissipative fluxes. However, this is not the only way of ordering terms when expanding in derivatives. A second, very popular choice is an expansion in terms of Knudsen and inverse Reynolds numbers. The Knudsen number is the ratio of the mean free path of the constituents of the fluid to the characteristic length of the system and is an indicator, if the system can be described by fluid dynamics or not. For a system where the mean free path of the constituents is much smaller than its characteristic length (i.e. small Knudsen number) fluid dynamics is applicable. The inverse Reynolds numbers are defined as the ratios of the dissipative fields to the equilibrium pressure and number density and quantify the deviations from equilibrium [80]. In the following I will use constituent relations for the shear stress tensor and bulk pressure including terms up to $\mathcal{O}(\mathrm{Re}^{-2})$ and $\mathcal{O}(\mathrm{KnRe}^{-1})$, but drop terms of order $\mathcal{O}(\mathrm{Kn}^2)$. This choice of truncation is motivated by the structure of the resulting equations. Excluding the second order terms in the Knudsen number allows to obtain a hyperbolic set of differential equations, ensuring causality [81]. The full evolution equations for the bulk pressure and shear stress tensor in this expansion read as

$$\Delta^{\mu\alpha}_{\nu\beta}\left[\tau_\pi\left(u^\lambda\nabla_\lambda\pi^\beta_\alpha - 2\pi^{\beta\lambda}\omega_{\alpha\lambda}\right) + 2\eta\nabla_\alpha u^\beta - \varphi_7\pi^\lambda_\alpha\pi^\beta_\lambda + \tau_{\pi\pi}\pi^\beta_\lambda\pi^\lambda_\alpha - \lambda_{\pi\Pi}\Pi\nabla_\alpha u^\beta\right] + \pi^\mu_\nu\left[1 + \delta_{\pi\pi}\nabla_\alpha u^\alpha - \varphi_6\Pi\right] = 0, \tag{2.61}$$

$$\tau_\Pi u^\mu\partial_\mu\Pi + \Pi + \zeta\nabla_\mu u^\mu + \delta_{\Pi\Pi}\Pi\nabla_\mu u^\mu - \varphi_1\Pi^2 - \lambda_{\Pi\pi}\pi^{\mu\nu}\nabla_\mu u_\nu - \varphi_3\pi^\mu_\nu\pi^\nu_\mu = 0. \tag{2.62}$$

As before the coefficients $\tau_{\pi\pi}$, $\delta_{\pi\pi}$, $\lambda_{\pi\Pi}$, $\delta_{\Pi\Pi}$, $\lambda_{\Pi\pi}$ and φ_i need to determined from a microscopic theory. The next part of this work is concerned with the description of heavy-ion collisions, mainly carried out at the LHC. Therefore, it is a valid assumption that the system is at zero net baryon chemical potential, simplifying the description. Consequence of this simplification is the absence of a baryon diffusion current, which has been left out in the above equations. In the next chapter I will demonstrate how to implement and solve these equations numerically in the scope of the Fluid$u$M framework.

3. Mode-by-mode fluid dynamics

This chapter is in parts inspired by [44, 82–84].

Now I turn to the first main part of this work: In the following chapter I introduce the Fluid$u$M framework and some of its applications in the subsequent chapter. Fluid$u$M is a framework for the description of ultrarelativistic heavy-ion collisions by the means of fluid dynamics, based on the equations derived in section 2. To obtain a numerically efficient description of these collisions, I make use of a special feature of heavy-ion collisions, namely the fact that experimental observables are always acquired by the means of event averages (mostly within one centrality bin). This allows to employ statistical symmetries and a background-fluctuation splitting ansatz.

3.1. Symmetries, coordinates and evolution equations

The choice of coordinate system is crucial to find the simplest description of a given problem. Importantly, the underlying symmetries should be reflected by the choice of the coordinate system. In the case of a heavy-ion collision, it is convenient to have a coordinate system with its origin being at the collision point of the two nuclei. I will take the z-axis to be along the beam axis. This allows the introduction of the proper time $\tau = \sqrt{t^2 - z^2}$ and of the rapidity $\eta = \operatorname{artanh}(z/t)$. For the transverse plane a parametrization in terms of cylindrical coordinates with radius $r = \sqrt{x^2 + y^2}$ and azimuthal angle $\phi = \arctan(y/x)$ is particularly convenient. The line element for this choice of coordinate system then reads as

$$\mathrm{d}s^2 = -\mathrm{d}\tau^2 + \mathrm{d}r^2 + r^2\mathrm{d}\phi^2 + \tau^2\mathrm{d}\eta^2. \tag{3.1}$$

The system of fluid equations in these coordinates can then be expressed as

$$\mathbf{A}(\Phi,\tau,r)\partial_\tau\Phi + \mathbf{B}(\Phi,\tau,r)\partial_r\Phi + \mathbf{C}(\Phi,\tau,r)\partial_\phi\Phi + \mathbf{D}(\Phi,\tau,r)\partial_\eta\Phi - \mathbf{S}(\Phi,\tau,r) = 0, \tag{3.2}$$

where $\mathbf{A}$, $\mathbf{B}$, $\mathbf{C}$ and $\mathbf{D}$ are coefficient matrices depending on the Nambu spinor Φ, as well as the radius r and proper time τ, together with the source term $\mathbf{S}$. The Nambu spinor Φ is the collection of the independent fluid fields of the description. In the most general setting all the fluid fields of the Nambu spinor depend on all four coordinates τ, r, ϕ and η. As a means of simplifying this complicated system of hyperbolic, partial differential equations I will make use of the statistical symmetries arising when describing an average of multiple collisions. Since the incoming nuclei are, to first approximation, round, the QGP created during their collisions in the overlap zone is of almond shape in the x-y-plane. Given the random positions of the nuclei in the colliding beams, the orientation of these almond shaped overlap zones will also be random. Selecting all events in one centrality and taking their event average yields a profile symmetric under azimuthal

rotations (fig. 6), i.e. the averaged fluid fields are invariant under the transformation $\phi \to \phi + \Delta\phi$.

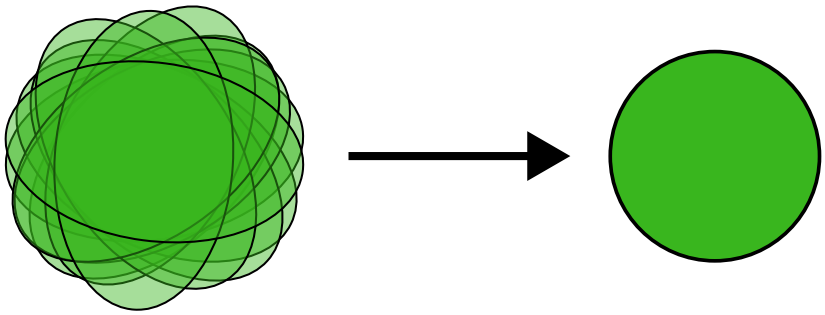

Figure 6: Sketch of event average taken in one centrality class. The event average of many profiles with random reaction plane angles yields a symmetric background configuration.

Additionally, I will only focus on the dynamics at mid-rapidity, where the usage of a boost invariant description, in which the fields are invariant under the transformation $\eta \to \eta + \Delta\eta$ is a useful simplification. Obviously these symmetries are not perfect. Therefore, the hydrodynamic fields will be decomposed into a background part which is invariant under azimuthal rotation and boosts, together with perturbations around it, which do not obey these symmetries

$$\Phi\left(\tau, r, \phi, \eta\right) = \Phi_0\left(\tau, r\right) + \epsilon\Phi_1\left(\tau, r, \phi, \eta\right). \tag{3.3}$$

Here I introduced ϵ as a formal expansion parameter, which will be set to one at the end. Applying this expansion to the general form of the fluid equations eq. 3.2 yields

$$\begin{aligned}&\mathbf{A}(\Phi_0 + \epsilon\Phi_1,\tau,r)\partial_\tau\left(\Phi_0 + \epsilon\Phi_1\right) + \mathbf{B}(\Phi_0 + \epsilon\Phi_1,\tau,r)\partial_r\left(\Phi_0 + \epsilon\Phi_1\right) + \mathbf{C}(\Phi_0 + \epsilon\Phi_1,\tau,r)\partial_\phi\left(\Phi_0 + \epsilon\Phi_1\right)\\ &+ \mathbf{D}(\Phi_0 + \epsilon\Phi_1,\tau,r)\partial_\eta\left(\Phi_0 + \epsilon\Phi_1\right) - \mathbf{S}(\Phi_0 + \epsilon\Phi_1,\tau,r) = 0.\end{aligned} \tag{3.4}$$

From this one can obtain the equations for the background fields Φ_0 by expanding in ϵ and taking only terms of zeroth order in ϵ into account. Similarly, the equations for the perturbation fields Φ_1 are obtained by taking the terms linear in ϵ. Due to the symmetries imposed on the background fields, the resulting equations are a set of 1+1 dimensional differential equations

$$\mathbf{A_0}(\Phi_0,\tau,r)\partial_\tau\Phi_0 + \mathbf{B_0}(\Phi_0,\tau,r)\partial_r\Phi_0 - \mathbf{S_0}(\Phi_0,\tau,r) = 0. \tag{3.5}$$

The additional symmetries of the background spinor Φ_0 lead to it generally having fewer independent components than the full spinor Φ. The matrices $\mathbf{A_0}$, $\mathbf{B_0}$ and $\mathbf{S_0}$ are defined as the projections of $\mathbf{A}$, $\mathbf{B}$ and $\mathbf{S}$ on the reduced subspace of the independent background components, evaluated on Φ_0. The equations for the perturbation fields are given by

$$\mathbf{A_1}(\Phi_0,\tau,r)\partial_\tau\Phi_1 + \mathbf{B_1}(\Phi_0,\tau,r)\partial_r\Phi_1 + \mathbf{C_1}(\Phi_0,\tau,r)\partial_\phi\Phi_1 + \mathbf{D_1}(\Phi_0,\tau,r)\partial_\eta\Phi_1 - \mathbf{S_1}(\Phi_0,\tau,r)\Phi_1 = 0, \tag{3.6}$$

where the matrices $\mathbf{A_1}$, $\mathbf{B_1}$, $\mathbf{C_1}$ and $\mathbf{D_1}$ simply correspond to the matrices $\mathbf{A}$, $\mathbf{B}$, $\mathbf{C}$ and $\mathbf{D}$ being evaluated on the background field configuration Φ_0. Note that the source term for the perturbation fields has additional contributions stemming from the linearization of the equations

$$\mathbf{S_1}(\Phi_0,\tau,r) = \partial_\Phi \left[\mathbf{S}(\Phi,\tau,r) - \mathbf{A}(\Phi,\tau,r)\partial_\tau\Phi_0 - \mathbf{B}(\Phi,\tau,r)\partial_r\Phi_0\right]_{\Phi=\Phi_0}. \tag{3.7}$$

From a practical point of view, the introduction of the background-fluctuation splitting ansatz eq. 3.3 reduces the dimensions of the background equations from 3+1 to 1+1. Especially for numerical algorithms, this simplifies the solving of the equation system tremendously. Evidently, the equations governing the evolution of the perturbation fields still have to be solved in 3+1 dimensions. To simplify the numerical treatment of these, it is useful to introduce an expansion in Fourier modes

$$\Phi_1(\tau,r,\phi,\eta) = \sum_{m=-\infty}^{\infty} \int \frac{\mathrm{d}k}{2\pi} e^{im\phi+ik\eta}\tilde{\Phi}_1(\tau,r,m,k). \tag{3.8}$$

Applying this expansion to the perturbation equations yields again 1+1 dimensional equations of motion for each individual mode

$$\mathbf{A_1}(\Phi_0,\tau,r)\partial_\tau\tilde{\Phi}_1 + \mathbf{B_1}(\Phi_0,\tau,r)\partial_r\tilde{\Phi}_1 + im\mathbf{C_1}(\Phi_0,\tau,r)\tilde{\Phi}_1 + ik\mathbf{D_1}(\Phi_0,\tau,r)\tilde{\Phi}_1 - \mathbf{S_1}(\Phi_0,\tau,r)\tilde{\Phi}_1 = 0. \tag{3.9}$$

Note that these equations can be solved individually for a given set of (m,k), decoupling from the equations of the other modes. Formally, all modes have to be evolved to obtain the evolution of the full event, which is not feasible in a practical calculation. However, it will become evident later that certain observables can be calculated from a few or even a single mode (up to linear order in this expansion scheme), allowing for a much more efficient computation. Evidently the symmetries of Φ_0 and Φ_1 also have to be obeyed in the initial conditions, which will be discussed next.

3.2. Initial conditions

To obtain a closed system of differential equations, initial conditions on a Cauchy hypersurface [6] need to be provided. In the following this hypersurface will always be defined as the hypersurface of constant initialization time τ_0. Evidently, the initial conditions for the background need to account for the additional symmetries, whereas the initial conditions for the perturbations need to be able to capture the event-by-event fluctuations.

3.2.1. Background fields

For the background fields the initial conditions reduce to a function of the radius r at the fixed initialization time τ_0. For a complete set of initial field configurations a function for each individual field of the background spinor Φ_0 has to be provided. However, in the following I will neglect initial flow and viscous corrections

[6] For a definition of Cauchy hypersurfaces, see section 4.1

and initialize all fields as zero with the exception of the temperature field. To obtain the temperature profile of a single event (i.e. with non-trivial ϕ-dependence), I will use the initial state model T$_\mathrm{R}$ENTo together with the equation of state. Since T$_\mathrm{R}$ENTo events are created with a random impact parameter, as well as multiplicity fluctuations of the created profiles, initial entropy density profiles in all centrality classes from 0% to 100% are created. Evidently these individual events do not share the same symmetries as the background configuration Φ_0. Since the symmetries of Φ_0 are based on averages of event ensembles, it is convenient to also define the initial background profiles as an average of an event ensemble. A single event can then be decomposed into a background part, obtained via the average of event ensembles, and a perturbation part around it. A convenient choice for the event ensembles are the experimentally defined centrality classes. However, these centrality classes are defined using the particle distribution functions, as measured in the final state by the detector. A centrality definition for the initial state is possible using the linear relationship between the initial total entropy of the collision and the multiplicity produced in the event (see section 1.3.1 for more details). The centrality classes defined by the initial entropy distribution then serve as ensembles in which the event average over the individual events is taken. The event-averaged entropy in a single centrality class is given by

$$s(r) = \frac{\mathrm{Norm}}{\tau_0}\langle T_R(r)\rangle, \tag{3.10}$$

where $\langle \ldots \rangle$ is the average over all events in the given class with random reaction plane angle and $T_R(r)$ is the transverse profile generated by T$_\mathrm{R}$ENTo . The factor $1/\tau_0$ is introduced to account for the longitudinal expansion (Bjorken flow). The normalization constant Norm is introduced to ensure the right multiplicity scaling of the T$_\mathrm{R}$ENTo events. In order to reduce the computational cost, the statistics of the event average can be enlarged by integrating out the ϕ-dependence of the initial profiles

$$\langle T_R(r)\rangle = \frac{1}{2\pi}\int_0^{2\pi} \mathrm{d}\phi \langle T_R(r,\phi)\rangle. \tag{3.11}$$

The resulting temperature profiles can be seen in fig. 7. The more central profiles have a bigger temperature at $r = 0$ and extend further out than the more peripheral profiles. The slight bends in the flanks of the profiles stem from the non-monotonicity of the speed of sound (see fig. 9) which enters through the inversion of the equation of state to change from entropy density to temperature.

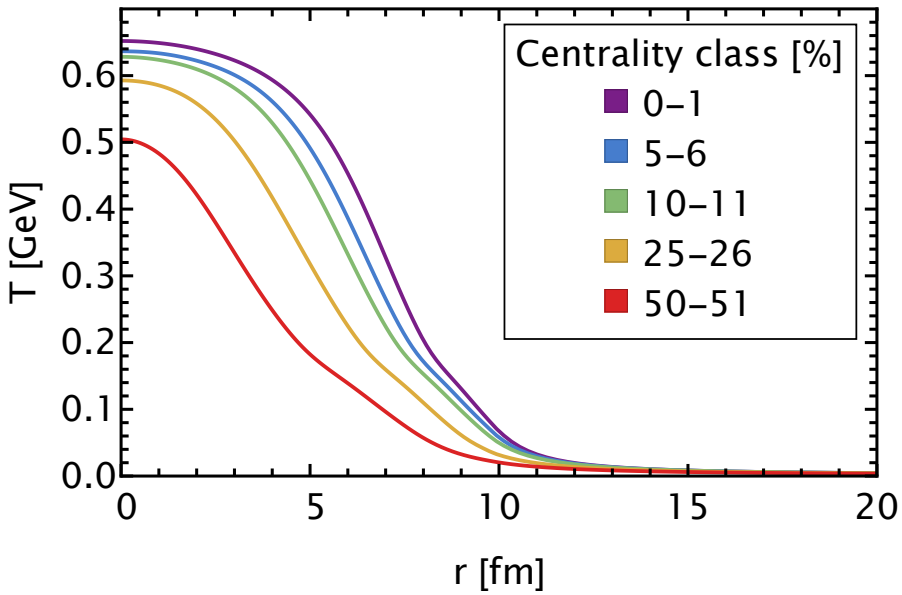

Figure 7: Initial temperature profiles for different centrality classes as function of the radius. The more central profiles have a bigger temperature at $r = 0$ and extend further out than the more peripheral profiles. The slight bends in the flanks of the profiles stem from the non-monotonicity of the speed of sound (see fig. 9) which enters through the inversion of the equation of state to change from entropy density to temperature.

The background is, by construction, a non-fluctuating quantity. Therefore, the fluctuating nature of heavy-ion collisions has to be accounted for in the perturbation part of this description, which is explained in the next section.

3.2.2. Perturbation basis

Similarly to the background fields, I also neglect initial flow and viscous corrections for the perturbation fields and only initialize a perturbation in the temperature field. These initial conditions will be more complicated due to the lack of symmetries compared to the background. Additionally, they have to include the event-by-event fluctuations from quantum and thermal fluctuations. Applying the Fourier decomposition of the perturbation modes introduced in eq. 3.8, recovers a similar situation as in the background case, where the initial perturbation configuration $\Phi_1(\tau_0,r,m,k)$ (the tilde notation has been dropped, since it will be clear from context if Φ_1 or its Fourier transformed are being referred to) is only a function of the radius r for a given set of azimuthal and longitudinal wave numbers m and k. To factor out the event-by-event fluctuations, it is convenient to decompose this initial perturbation configuration further in a set of non-

fluctuating, radial basis functions $\psi_l^{(m)}(r)$ with the radial wave number l and expansion coefficients $a_l^{(m)}(k)$ (In the following I will neglect the dependence of the expansion coefficients on the longitudinal wave number k, since the bulk of this work is concerned with the boost invariant dynamics of a heavy-ion collision).
Now I will demonstrate how to decompose the initial entropy profile in the background and perturbation parts, as well as the decomposition of the perturbation part in the basis functions $\psi_l^{(m)}(r)$. The initial transverse entropy profile is decomposed according to

$$s(r,\phi) = \bar{s}(r)(1 + \delta s(r,\phi)). \tag{3.12}$$

Here it is convenient to factor out the background entropy $\bar{s}(r)$ from the perturbation part, which according to eq. 3.8 is written as Fourier modes

$$\delta s(r,\phi) = \sum_{m=-\infty}^{\infty} a^{(m)}(r) e^{im(\phi-\phi_P)}, \tag{3.13}$$

where ϕ_P is the reaction plane angle of the event. In the following I will assume $\phi_P = 0$ without loss of generality. As introduced before, the radial dependence of the perturbation modes is split up in a set of radial basis functions $\psi_l^{(m)}(r)$ together with the corresponding expansion coefficients $a_l^{(m)}$

$$a^{(m)}(r) = \sum_l a_l^{(m)} \psi_l^{(m)}(r). \tag{3.14}$$

To avoid a conical singularity of $\delta s(r,\phi)$ at $r = 0$, the functions $\psi_l^{(m)}(r)$ need to decay like $r^{|m|}$ for $r \to 0$. This leaves a wide choice of possible sets of basis functions. However, there is a phenomenologically well motivated choice when considering the eccentricity of the initial entropy profile

$$\epsilon_m = \frac{\int_{\mathbb{R}^2} s(r,\phi) r^m e^{im\phi}}{\int_{\mathbb{R}^2} s(r,\phi) r^m}, \tag{3.15}$$

which has been shown to be related linearly to the corresponding flow coefficient in the final state [37]. Since the eccentricity is an integration over r^m, it is particularly convenient to choose the basis functions as polynomials

$$\psi_l^{(m)}(r) = \sum_{n=m}^{m+l-1} C_{l|n}^{(m)} r^n, \tag{3.16}$$

for all m except $m = 1$ and $m = 0$, which I will discuss later. This choice of basis functions ensures $a_1^{(m)} = \epsilon_m$ at leading order. In order for the polynomials to from an orthonormal basis, they need to fulfill

$$(\psi_{l_1}^{(m)}(r), \psi_{l_2}^{(m)}(r)) = \delta_{l_1,l_2}, \tag{3.17}$$

with the scalar product being defined as

$$(f(r),g(r)) = \frac{1}{N_m}\int r\mathrm{d}r\ \bar{s}(r)f^*(r)g(r). \tag{3.18}$$

For the later matching purposes it is convenient to choose a normalization constant N_m that depends on the azimuthal wave number m. The orthonormal basis allows to link the constants N_m and $C_{l|n}^{(m)}$ for the leading polynomial $\psi_1^{(m)}(r) \propto r^m$ via the relation

$$(\psi_1^{(m)}(r),\psi_1^{(m)}(r)) = 1. \tag{3.19}$$

The coefficient of the leading order polynomial is then given by

$$C_{1|m}^{(m)} = \sqrt{\frac{N_m}{\int \mathrm{d}\ r^{2m+1}\bar{s}(r)}}. \tag{3.20}$$

To fully fix these coefficients, I demand that the first expansion coefficient equals the eccentricity of the event up to first order. The expansion coefficient can be obtained via

$$a_l^{(m)} = \frac{1}{2\pi N_m}\int \mathrm{d}\phi\mathrm{d}r\ r[s(r,\phi) - \delta_{m,0}\bar{s}(r)]\psi_l^{(m)}(r)e^{-im\phi}. \tag{3.21}$$

Note that the subtraction of the background entropy only is applied in the case of $m = 0$, covering the first special case mentioned above. Demanding that $a_1^{(m)} = \epsilon_m$ up to first order in perturbations, fixes the normalization constant N_m to

$$N_m = \frac{(\int \mathrm{d}r\ r^{m+1}\bar{s}(r))^2}{\int \mathrm{d}r\ r^{2m+1}\bar{s}(r)}, \tag{3.22}$$

and subsequently also the coefficient for the first polynomial

$$C_{1|m}^{(m)} = \frac{\int \mathrm{d}r\ r^{m+1}\bar{s}(r)}{\int \mathrm{d}r\ r^{2m+1}\bar{s}(r)}. \tag{3.23}$$

A set of basis functions for a given m and a given number of l modes can then be generated from the set $\{r^m, r^{m+1}, \ldots, r^{m+l-1}\}$ using any method to construct an orthonormal basis, such as the Gram-Schmidt process [85], for example. For practical calculations I use the related QR-decomposition [86] to construct the set of orthogonal polynomials from the matrix $A_{i,j} = (r^i,r^j)$ with (r^i,r^j) being again the scalar product between r^i and r^j as introduced above. Note that in the case of $m = 1$, the eccentricity is defined by the integration over r^3, not r^1, which means that the lowest order polynomial also needs to be proportional to r^3 in this case.

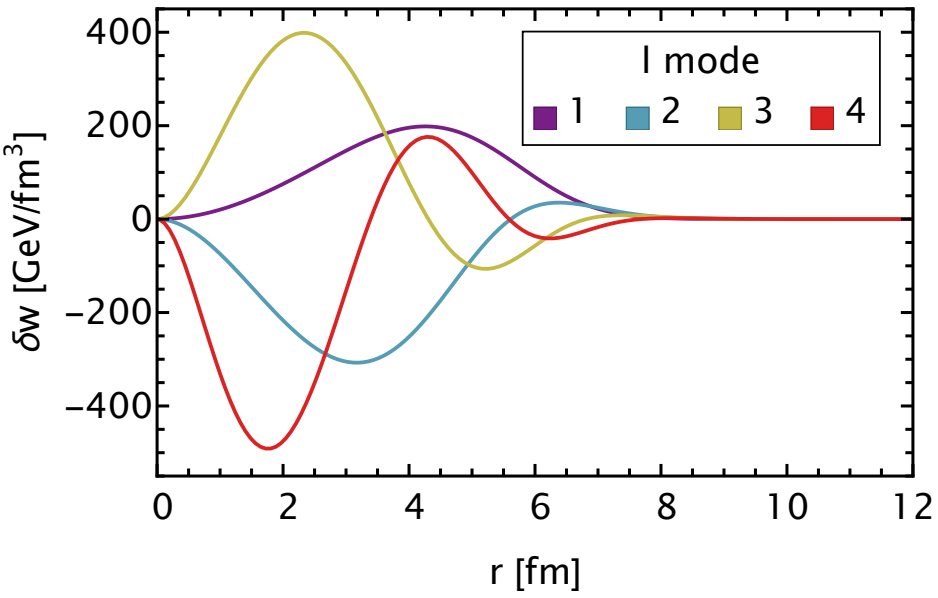

Figure 8: Plot of the initial enthalpy perturbation for $m = 2$ and l-modes $l = 1,2,3,4$ as function of the radius. The lowest order mode ($l = 1$) is proportional to $r^2\bar{s}(r)$. The higher order modes are then proportional to polynomials of higher degree in r, as described above. The orthogonality of the polynomials results in the mode of rank l having $l-1$ zero crossings (disregarding the initial value of zero at $r = 0$).

A plot of the initial enthalpy perturbation modes for $m = 2$ and $l = 1,2,3,4$ can be seen in fig. 8. The lowest order mode ($l = 1$) is proportional to $r^2\bar{s}(r)$. The higher order modes are then proportional to polynomials of higher degree in r, as described above. The orthogonality of the polynomials results in the mode of rank l having $l-1$ zero crossings (disregarding the initial value of zero at $r = 0$).
With initial conditions for the background and the perturbations at hand, it is useful to return to the equations of motion and specify the equations introduced in section 3.1, as well as the fluid fields making up the background spinor Φ_0 and the perturbation spinor Φ_1.

3.3. Equations of motion & field conventions

The fluid dynamic equations used for the description of the expanding fireball are based on the conservation of energy and momentum, as presented in section 2, together with the constituent equations from the Israel-Stewart theory. The fluid fields appearing in this system of equations are the temperature T, the three independent components of the fluid velocity u^r, u^ϕ and u^η, the components π^ϕ_ϕ, π^η_η, π^r_ϕ, π^r_η and π^ϕ_η of the shear stress tensor and finally the bulk pressure Π. Of these only the temperature, the radial component of

the fluid velocity, the bulk pressure and two components of the shear stress tensor appear in the background configuration Φ_0. The two independent components of the shear stress tensor are chosen to be π^ϕ_ϕ and π^η_η, totaling five independent fields. Obviously, the perturbation configuration Φ_1 will include more fields. These are one perturbation of the temperature, three perturbations of the fluid velocity (δu^r, δu^ϕ, δu^η), five components of the shear stress tensor and the perturbation of the bulk pressure, yielding 10 perturbation fields in total. The independent perturbation components of the shear stress tensor are chosen to be $\delta\pi^\phi_\phi$, $\delta\pi^\eta_\eta$, $\delta\pi^r_\phi$, $\delta\pi^r_\eta$ and $\delta\pi^\phi_\eta$. In practice it is more convenient to use reparametrizations and equivalent fields, such as the perturbation of the enthalpy density instead of the perturbation of the temperature. It can also be useful (especially for the calculation of the final hadron spectra, see section 4) to parametrize the fields using the so-called tetrad formalism [65]. In this formalism the fields are defined in a local orthogonal frame. The transformation into this local frame is given by the tetrad field $v^a_\mu(x)$, which itself depends on the space-time coordinate x. The tetrad field is defined such that the general coordinate metric $g_{\mu\nu}(x)$ is transformed into the Minkowksi metric $\eta_{ab} = \text{diag}(-1,1,1,1)$,

$$g_{\mu\nu}(x) = v^a_\mu(x) v^b_\nu(x) \eta_{ab}. \tag{3.24}$$

It is particularly convenient to choose the local frame such that it is aligned with the (background) fluid velocity, resulting in

$$v^a_\mu(x) = \begin{pmatrix} \bar{\gamma} & -\bar{v}\bar{\gamma} & 0 & 0 \\ -\bar{v}\bar{\gamma} & \bar{\gamma} & 0 & 0 \\ 0 & 0 & r & 0 \\ 0 & 0 & 0 & \tau \end{pmatrix}, \tag{3.25}$$

and

$$v^\mu_a(x) = \begin{pmatrix} \bar{\gamma} & \bar{v}\bar{\gamma} & 0 & 0 \\ \bar{v}\bar{\gamma} & \bar{\gamma} & 0 & 0 \\ 0 & 0 & 1/r & 0 \\ 0 & 0 & 0 & 1/\tau \end{pmatrix}, \tag{3.26}$$

for the tetrad and its inverse. The inverse of the tetrad $v^\mu_a(x)$ has been defined such that

$$v^a_\mu(x) v^\nu_a(x) = \delta^\nu_\mu \quad \text{and} \quad v^a_\mu(x) v^\mu_b(x) = \delta^a_b. \tag{3.27}$$

In the orthogonal frame the fluid velocity is then simply given by $\bar{u}^a = (1,0,0,0)$, with the perturbations around it reading as $\delta u^a = (0,v_1,v_2,v_3)$ (as usual the normalization of the fluid velocity has been used).

Similarly, the background shear stress tensor and its perturbations can be parametrized as

$$\bar{\pi}^{ab} = \begin{pmatrix} 0 & 0 & 0 & 0 \\ 0 & -\bar{\pi}^t & 0 & 0 \\ 0 & 0 & \bar{\pi}^{22} & 0 \\ 0 & 0 & 0 & \bar{\pi}^{33} \end{pmatrix}, \tag{3.28}$$

and

$$\delta\pi^{ab} = \begin{pmatrix} 0 & \delta v_1 \bar{\pi}^t & -\delta v_2 \bar{\pi}^{22} & -\delta v_3 \bar{\pi}^{33} \\ \delta v_1 \bar{\pi}^t & -\delta\pi^t & \delta\pi^{12} & \delta\pi^{13} \\ -\delta v_2 \bar{\pi}^{22} & \delta\pi^{12} & \delta\pi^{22} & \delta\pi^{23} \\ -\delta v_3 \bar{\pi}^{33} & \delta\pi^{13} & \delta\pi^{23} & \delta\pi^{33} \end{pmatrix}, \tag{3.29}$$

with the abbreviations $\bar{\pi}^t = \bar{\pi}^{22} + \bar{\pi}^{33}$ and $\delta\pi^t = \delta\pi^{22} + \delta\pi^{33}$. The tetrad formalism mainly allows for a simple parametrization of the fluid fields in the orthogonal frame. Note that the equations of motion remain unchanged even though the background fluid velocity itself is much simpler, since the tetrad fields depend on space-time and also enter the equations of motion. In the following plots I will present the results for the more intuitive fields in the Bjorken coordinate frame (i.e. $\bar{\pi}^{\phi\phi}$ instead of $\bar{\pi}^{22}$). The relations between the fields in the orthogonal frame and in the Bjorken frame can be found in Appendix A.
The final piece for a closed system of differential equations is the equation of state, together with the specification of the transport coefficients, which is presented in the next section.

3.4. Equation of state & transport properties

3.4.1. Equation of state

As already stated in the introduction of this work, the equation of state linking the different thermodynamic quantities, such as pressure and energy density, can be obtained via LQCD calculations for the region of the QCD phase diagram of interest. However, for the background-fluctuation splitting ansatz and the numerical implementation of Fluid$u$M by means of spectral methods it is essential to have a continuous and differentiable equation of state. Since the numerical solution also covers parts of the liquid already frozen out, the equation of state also needs to be valid in the hadronic phase. A suitable choice for this region is the hadron resonance gas (HRG). To obtain an equation of state $p(T)$ fulfilling these conditions, a parametrization of the pressure is fitted to the LQCD data [87, 88] above a critical temperature $T_c = 154\text{MeV}$ and to the HRG [89] below T_c [7]. The parametrization is given by

$$\frac{p(T)}{T^4} = \exp\left[-c^2\hat{T} - d^2\hat{T}^2\right] \left[\frac{\frac{(16+21/2N_f)\pi^2}{90} a_1\tilde{T} + a_2\tilde{T}^2 + a_3\tilde{T}^3 + a_4\tilde{T}^4}{1 + b_1\tilde{T} + b_2\tilde{T}^2 + b_3\tilde{T}^3 + b_4\tilde{T}^4}\right] \tag{3.30}$$

[7] An extra parametrization is used, because the parametrizations provided in the literature has a pole at low temperature due to the used Padé approximation [87]

with $\tilde{T} = T/T_c$ where $T_c = 154\,\text{MeV}$ and $N_f = 3$ as the number of free quarks and $\hat{T} = T/100\,\text{MeV}$. The best fit parameters are given in tab. 1.

a_1	a_2	a_3	a_4	b_1	b_2	b_3	b_4	c	d
-15.53	18.62	-10.73	2.74	-3.31	5.31	-4.65	1.86	-1.05	0.10

Table 1: Best fit parameters for the chosen parametrization of the pressure.

The resulting pressure can be seen in the left panel of fig. 9. In the blue shaded area data from lattice QCD has been used for the fit. For the gray shaded area the hadron resonance gas was used, while both regions are connected smoothly in the transition area. More details on both models can be found in section 6. The right hand panel of fig. 9 shows the speed of sound squared as function of the temperature. The non-monotonic behavior of the speed of sound in the region of the crossover has interesting implications for the evolution of the fluid fields.

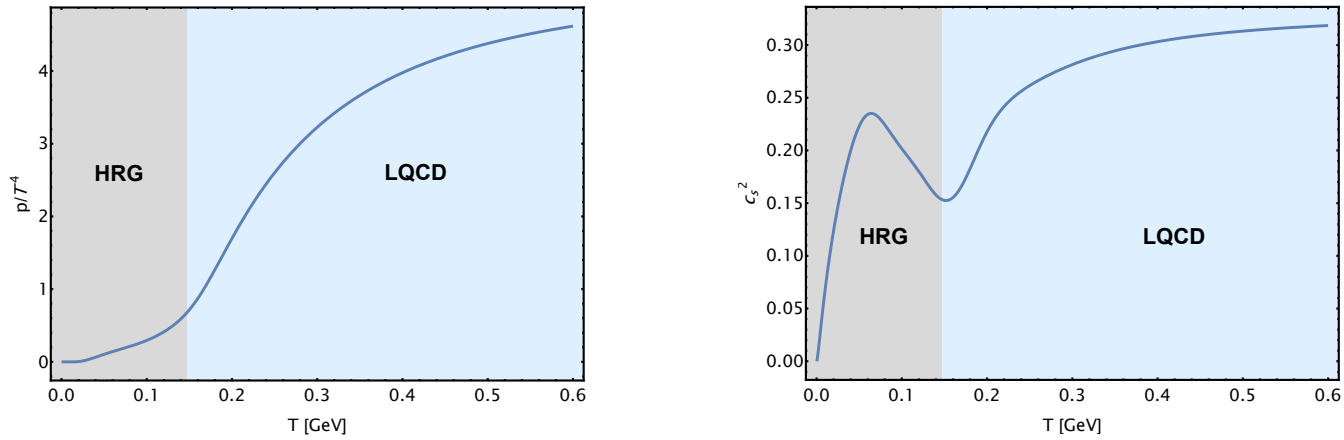

Figure 9: Plot of the pressure $p(T)$ (left) and the speed of sound squared $c_s^2(T)$ (right) as function of the temperature. In the blue shaded area data from lattice QCD has been used for the fit. For the gray shaded area the hadron resonance gas was used, while both regions are connected smoothly in the transition area. More details on both models can be found in section 6.

3.4.2. Transport properties

The fluid dynamic description also requires the specification of the transport coefficients, encoding the microscopic dynamics of the QCD matter. Since the calculation of these transport properties from first principles is still challenging [90, 91], I will use parametrizations for the shear and bulk viscosity.
Using results from Yang-Mills calculations performed in [92], the shear viscosity to entropy ratio is parametrized as

$$\frac{\eta}{s}(T) = \frac{4}{3}(\eta/s)_{\text{scale}} \left(0.0613 \left(\frac{T}{T_c} + 0.709 \right)^2 + \frac{0.02}{(T/T_c)^6} \right) \tag{3.31}$$

with $T_c = 156\,\mathrm{MeV}$ and $(\eta/s)_{\mathrm{scale}}$ taken to be around 2 (the precise value of $(\eta/s)_{\mathrm{scale}}$ will be determined and discussed later in the scope of bayesian inference using Fluid$u$M). Similarly, the ratio of the bulk viscosity to the entropy is parametrized [93] as

$$\frac{\zeta}{s}(T) = \frac{(\zeta/s)_{\max}}{1 + \left(\frac{T - 24\,\mathrm{MeV}}{175\,\mathrm{MeV}}\right)^2} \tag{3.32}$$

where $(\zeta/s)_{\max}$ is taken to be around 0.03. The concrete value is again discussed later in section 5. The corresponding relaxation times are taken to be

$$\frac{\tau_{\mathrm{bulk}}}{\zeta/(\epsilon + p)} = \frac{1}{15\left(\frac{1}{3} - c_s^2\right)^2} + \frac{0.1\,\mathrm{fm/c}}{\zeta/(\epsilon + p)}, \tag{3.33}$$

$$\frac{\tau_{\mathrm{shear}}}{\eta/(\epsilon + p)} = \begin{cases} 5 & T \geq T_{\mathrm{chem}}, \\ 5 + (T - T_{\mathrm{chem}})/3\,\mathrm{MeV} & T < T_{\mathrm{chem}}. \end{cases} \tag{3.34}$$

The modification of the shear relaxation time below the chemical freeze-out temperature ensures that the relaxation time is still much larger than the characteristic scale of the hadron resonance gas when scatterings become more sparse. From the other coefficients appearing in eq. 2.62 I set $\delta_{\pi\pi} = 4\tau_{\mathrm{shear}}/3$ and neglect all other second order transport coefficients. However, these can be included easily into the framework. With a closed system of differential equations at hand, I will now give a brief overview of their implementation in the Mathematica package Fluid$u$M and the algorithms used to solve them numerically in the next section.

3.5. Numerical methods

In this subsection I will give a short overview of the numerical methods used to solve the above presented system of partial differential equations. A more detailed description can be found in [44].
In general it is advantageous to reformulate the 1+1 dimensional system of differential equations, such that only the time is kept as continuous evolution parameter. The resulting set of ordinary differential equations can then be solved by standard numerical methods, such as the Adams method. In the present case, this is done by the method of lines, where the radial direction is discretized, turning the radial derivative ∂_r into a matrix D_{ij} acting on the discretized fluid field spinors $\Phi_j(\tau) = \Phi(\tau, r_j)$. The matrix D_{ij} representing the spatial derivative can be obtained by applying different discretization methods, such as finite difference schemes or Galerkin methods. For this system the pseudospectral discretization method [94] is a particular convenient choice. When applying a pseudospectral discretization method, the solution is approximated by a linear superposition of basis functions. The most common choice, especially for periodic boundary conditions, is the Fourier spectral method. For the purpose of this work the Chebyshev polynomials [95] of the first kind $T_n(x)$ are a more suitable choice

$$T_n(x) = \cos(n \arccos(x)), \quad x \in (-1,1). \tag{3.35}$$

The semi-infinite domain $r \in (0,\infty)$ is being mapped to the finite interval $x \in (0,1)$ via

$$r = \frac{Lx}{(1-x^2)^{1/\alpha}} = \frac{L\cos(\theta)}{\sin^{2/\alpha}(\theta)}, \tag{3.36}$$

with L being some characteristic length, $\alpha > 0$ and $\theta \in (0,\pi)$ using the substitution $x = \cos(\theta)$. The discretization points are then chosen as

$$\theta_j = \frac{(j-\frac{1}{2})\pi}{2N}, \quad j = 1,\ldots,N \tag{3.37}$$

corresponding to

$$r_j = \frac{L\cos\left(\frac{(j-\frac{1}{2})\pi}{2N}\right)}{\sin^{2/\alpha}\left(\frac{(j-\frac{1}{2})\pi}{2N}\right)}. \tag{3.38}$$

Using this discretization, the spatial derivatives can be expressed in terms of discrete sine and cosine transformations [44].

The final part of the numeric implementation is the inclusion of a numerical spectral viscosity [96–98] to suppress oscillations stemming from the spatial discretization scheme, whilst not lowering the accuracy of the solution. This is achieved by adding a diffusive term (also known as numerical viscosity) consisting out of a small second order derivative, which vanishes in the continuum limit $N \to \infty$.

The above described methods have been implemented in the code package Fluid$u$M in Mathematica. To verify and validate this implementation of the numerical methods, a comparison against the analytically calculable Gubser solution [99–101] has been performed [44]. In the next section I will present results obtained from the numerical implementation and discuss some features of the evolution of the QGP during its expansion.

3.6. Fluid evolution

In this section I want to discuss some features of the fluid evolution, starting with the background fields.

As seen before, the initial temperature background profile has its largest value in the center of the fireball, decaying for larger radii. The resulting gradients in pressure drive the expansion of the plasma leading to a cooling of the system. This broadening and decline of the temperature can be seen in fig. 10. During the evolution of the system the freeze-out hypersurface, defined by $T = T_{\text{fo}}$ gets recorded and stored by Fluid$u$M. Technically the freeze-out hypersurface needs to be defined using the full temperature (i.e. the background plus the perturbations). However, it has been shown in [102] that it is in fact possible and easier to define the freeze-out hypersurface by using only the background temperature. This means that instead of a fluctuating geometry, the freeze-out hypersurface has the same symmetries as the background configuration, but the full reconstructed temperature fluctuates on it. Since the freeze-out hypersurface shares the symmetries of

the background fields, it is a one-dimensional τ-r-curve, which can be parametrized by $(\tau(c), r(c))$, with $c \in [0,1]$ without loss of generality. Its hypersurface element is then given by

$$\mathrm{d}\Sigma_\mu = r(c)\tau(c)\left(-\frac{\partial r}{\partial c}, \frac{\partial \tau}{\partial c}, 0, 0\right)\mathrm{d}c\mathrm{d}\phi\mathrm{d}\eta. \tag{3.39}$$

Note that the temperature profile still evolves for points below the freeze-out temperatures, as a consequence of the choice of numerical algorithm. The freeze-out hyper-surface for different centrality classes is shown in fig. 11. The more central events with bigger overlap of the initial nuclei extend to larger radii, as is the case in the initial profiles. The larger temperature of the central profiles leads to a longer fluid phase, since the freeze-out temperature is the same for all centrality classes. A detailed discussion on how to obtain the hadrons in the final state from the fluid fields on the freeze-out hypersurface can be found in the next chapter.

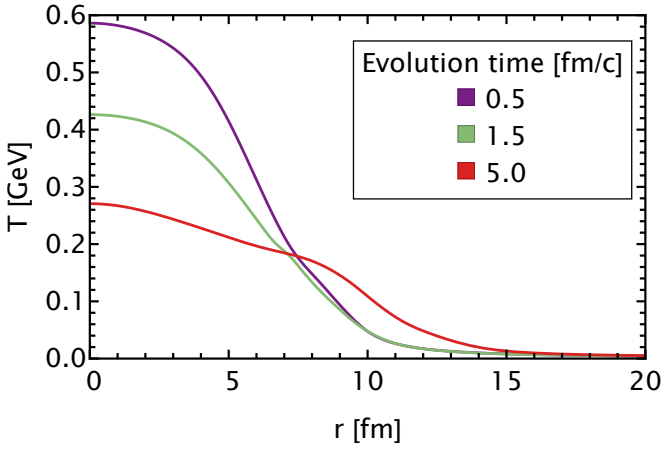

Figure 10: Background temperature after different evolution times.

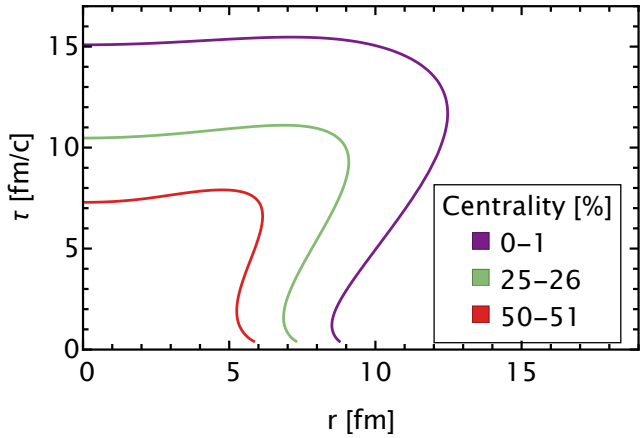

Figure 11: Freeze-out hyper-surfaces for different centrality classes.

The pressure gradient driving the expansion of the system leads to the build up of the radial fluid velocity. Over time the peak of the fluid velocity moves outwards with the QGP matter for later times. The local extrema and oscillations of the fluid velocity shown in fig. 12 can be traced back to non-monotonic behavior of the speed of sound in the range of 100-200 MeV. These non-monotonic features translate to the independent components of the shear stress tensor. The dimensionless ratio of $\pi^{\phi\phi}/w$ at different times is plotted in fig. 13. Similar to the fluid velocity, the components of the shear stress tensor also travel outwards in waves.

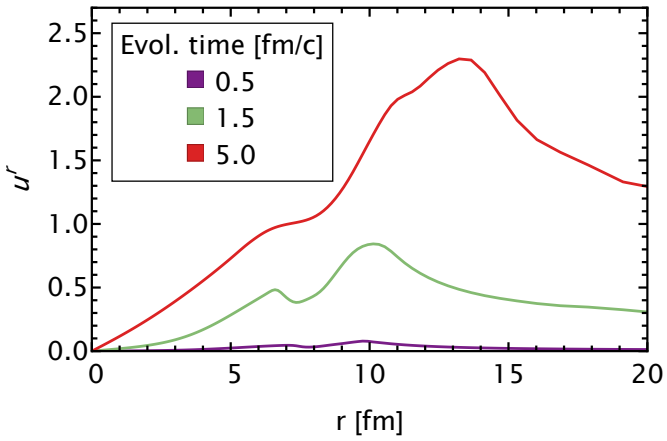

Figure 12: Radial fluid velocity after different evolution times.

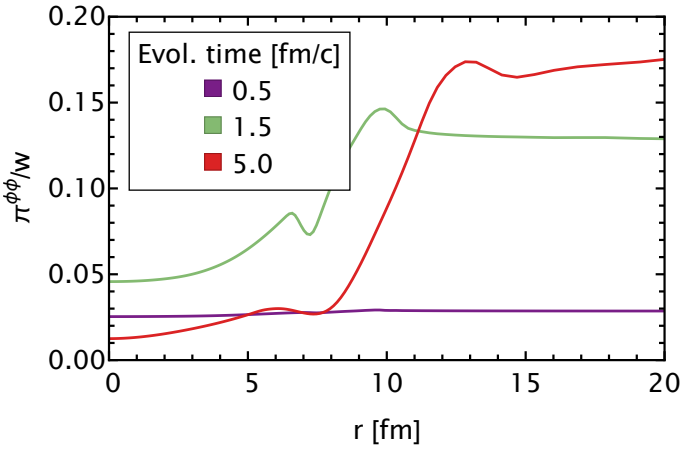

Figure 13: $\pi^{\phi\phi}$ component of the shear stress tensor after different evolution times.

The final field of the background configuration is the bulk pressure, depicted in fig. 14. As expected, the bulk pressure is negative, acting against the expansion of the system. The initial minimum of the bulk pressure develops at the radius where the bulk viscosity (eq. 3.32) has its maximum. For later times, when the fluid velocity already has gradients at smaller radii, the minimum of the bulk pressure travels inwards.

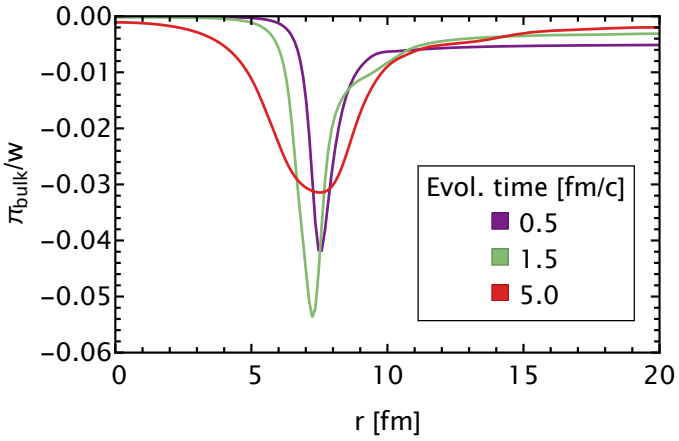

Figure 14: Bulk pressure after different evolution times.

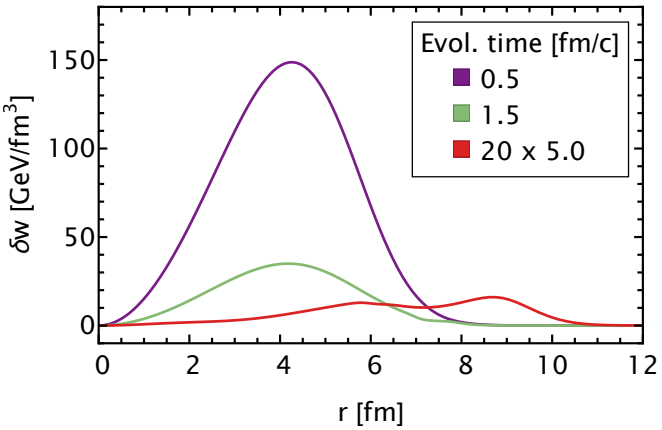

Figure 15: Enthalpy perturbation after different evolution times. The curve at $\tau = 5.0\,\mathrm{fm/c}$ (red) is rescaled by a factor 20 for better visibility.

Next I briefly discuss the evolution of the individual perturbation modes and then look at the evolution of a reconstructed event. Similar to the background, only the field corresponding to the perturbation of the temperature gets initialized with non-zero values. The perturbations of the other fields develop, sourced by the background fields and the perturbation in enthalpy (for the numerical implementation it is a convenient choice to work in terms of an enthalpy perturbation). As seen before, the individual modes evolve independently from each other. Given the wave-like shape of the initial conditions for the enthalpy perturbation, the evolution of this field is also given by waves propagating outwards, as can be seen in fig. 15. To obtain the full profile the perturbations have to be recombined with the background according to eq. 3.3. To reconstruct a realistic event an infinite amount of modes is needed formally. However, in practice the modes with high wave numbers (azimuthal, radial and longitudinal) are damped more efficiently by viscosity, since they correspond to finer details in the spatial domain.

At this point one of the strengths of the Fluid$u$M framework becomes apparent. On one hand it can be used to evolve a single event in the following way: First, the initial profile is decomposed into the background configuration (chosen according to its centrality class) and the perturbations around it. Then the perturbations get expressed in terms of the basis expansion coefficients $\{a_l^{(m)}\}$. Afterwards the fluid evolution of the background and perturbation fields is calculated. By definition of the background configuration its fluid evolution is the same for all events of one centrality class. Due to the linear nature of the perturbation equations, the expansion coefficients can be factored out, making the evolution of the perturbation fields also the same for all events of the same centrality class. Finally, the solution of the full event can be reconstructed by combining the background and perturbation solutions with the basis expansion coefficients. Since the

fluid solutions are independent of the events, the evolution of a multitude of events is a simple extension of the evolution of a single event. The decomposition of the individual events happens already on the level on the initial conditions and is given by a two-dimensional integration. Therefore it is easy to perform numerically for a large number of events. The events can then be reconstructed as the single event before, using the same fluid evolution solutions.

I will now give an example for this reconstruction for a very simple event with only one non-zero expansion coefficient, namely $a_1^{(2)} = \frac{1}{2}$. The initial enthalpy density of this event can be seen in fig. 16. The orientation of the profile has been chosen such that the long axis is aligned with the x-axis. Due to the elongated nature of the profile, the pressure gradient in the y-direction is larger than the gradient in x-direction, leading to a faster expansion along the y-axis. After a sufficient amount of time this results in a phenomenon known as shape inversion, where in this case the long axis will be aligned with the y-axis, as can be seen in fig. 17.

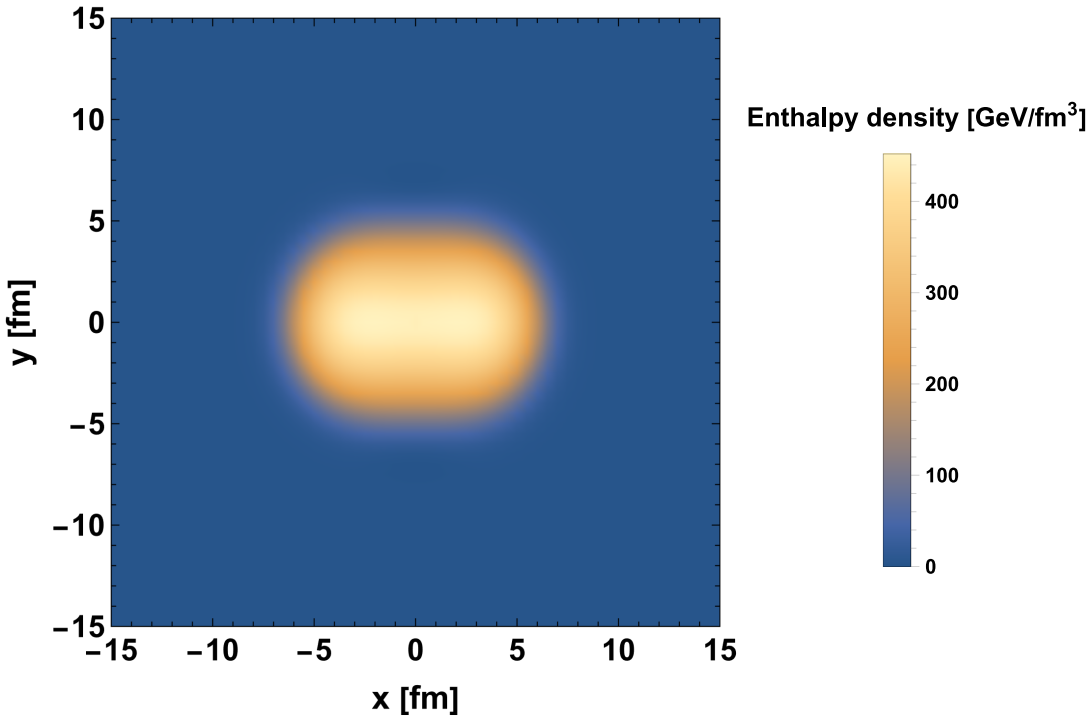

Figure 16: Initial enthalpy density for an event with the only non-zero expansion coefficient being $a_1^{(2)} = \frac{1}{2}$. The orientation of the profile has been chosen such that the long axis is aligned with the x-axis.

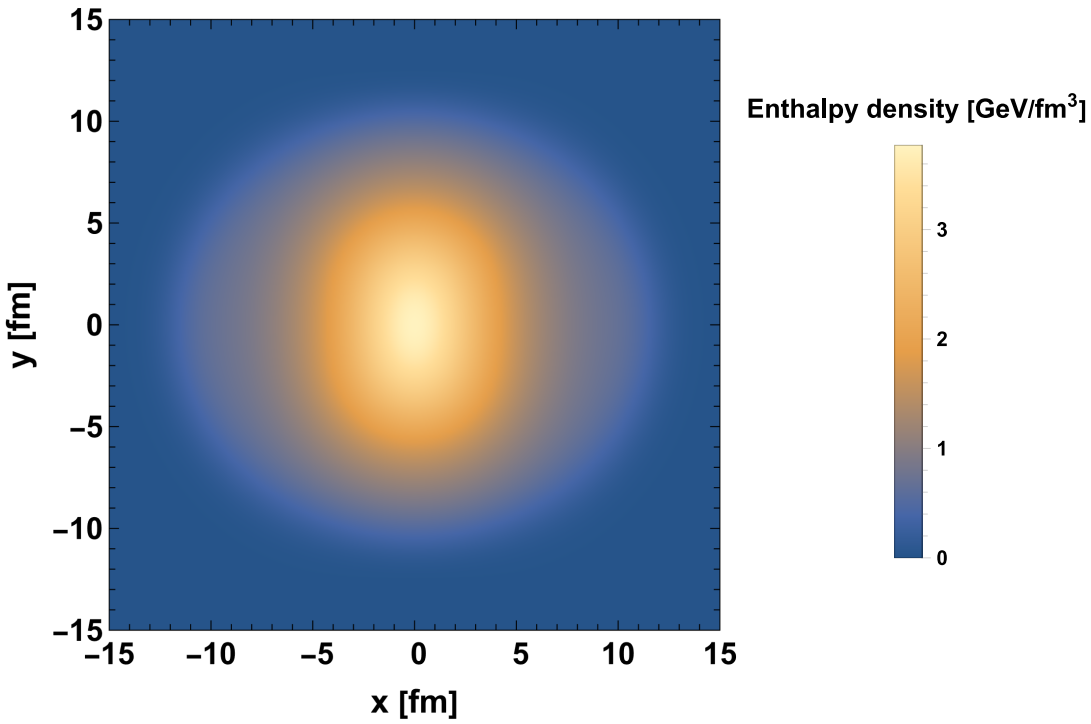

Figure 17: Enthalpy profile after 8 fm/c. The larger pressure gradients in y-direction of the initial state gives rise to a faster acceleration in this direction. After a sufficient amount of time the faster expansion leads to the so-called shape inversion, where the long axis of the profile is now oriented along the y-axis.

This process of shape inversion can also be seen when studying the modulation of the enthalpy for different times as shown in fig. 18. The modulation in this plot is defined as the ratio of the enthalpy as function of the azimuthal angle ϕ over the enthaply evaluated at $\phi = 0$ at some fixed radius r_0, i.e. $w(r_0,\phi)/w(r_0,0)$. The initial enthalpy profile shows a strong modulation as function of the azimuthal angle. This modulation then gets smaller over time, and inverts for a sufficiently long evolution time.

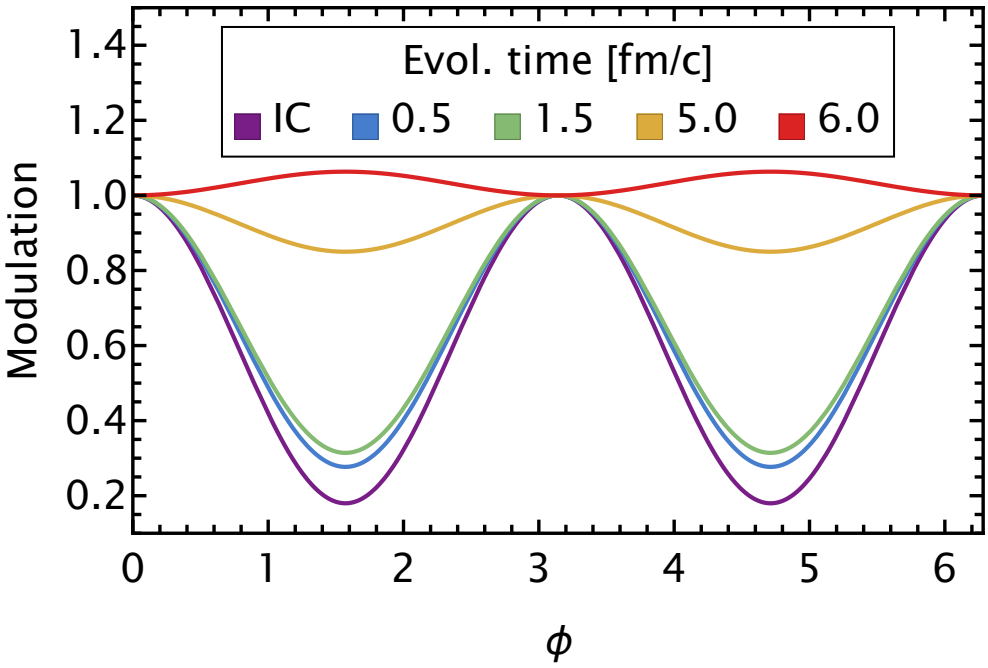

Figure 18: Enthaply modulation for different times as function of the azimuthal angle. The modulation in this plot is defined as the ratio of the enthalpy as function of the azimuthal angle ϕ over the enthaply evaluated at $\phi = 0$ at some fixed radius $r_0 = 1\,\text{fm}$, $w(r_0,\phi)/w(r_0,0)$. The initial enthalpy profile shows a strong modulation as function of the azimuthal angle. This modulation then gets smaller over time, and inverts for a sufficiently long evolution time.

Since the QGP is a viscous fluid, it is very interesting to study how the shape inversion behaves for different viscosities. For this I plot the amplitude of the enthalpy as function of the evolution time for different viscosities. The amplitude is here calculated as $|\max(w(\phi)) - \min(w(\phi))|$ at fixed radius and evolution time. The enthalpy amplitude for a system with the same parameters as above together with a system where the shear and bulk viscosities have been doubled can be seen in fig. 19. Since both cases use the same initial conditions, the amplitude of the two enthalpies is the same initially. The larger viscosity dampens the system more effectively, leading to a faster decrease of the enthalpy amplitude. For late times, after the shape inversion, the case with the smaller viscosities starts to build up the larger enthalpy amplitude, because the pressure gradients are damped less.

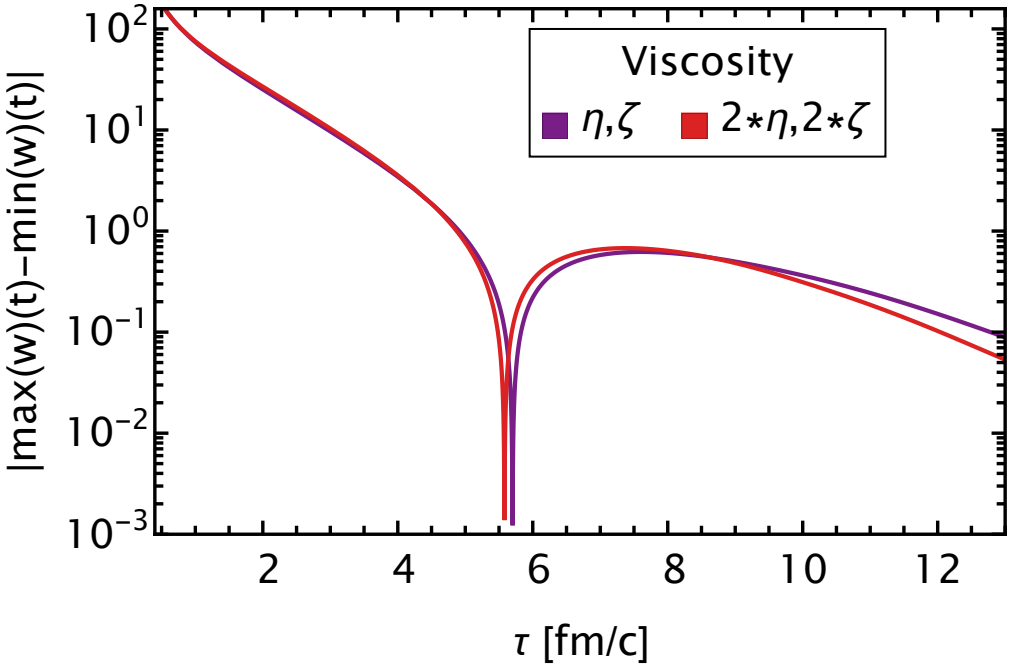

Figure 19: Difference of the enthalpy density for two reconstructed events with different viscosities as function of time. The difference is calculated between the maximum and minimum of the enthalpy at a given time and fixed radius as function of the azimuthal angle. The purple curve has the same parameters as the modulation plot from before. The red curve has double the shear and bulk viscosity. Since both cases use the same initial conditions, the amplitude of the two enthalpies is the same initially. The larger viscosity dampens the system more effectively, leading to a faster decrease of the enthalpy amplitude. For late times, after the shape inversion, the case with smaller viscosity starts to build up the larger enthalpy amplitude, because the pressure gradients are damped less.

This anisotropy of the enthaply and the fluid velocity also translates to the final state observables. In the next chapter I will discuss how to calculate the final particle spectrum, measured in the detectors from the fluid dynamic simulations described above.

4. Particle production, resonance decays & final state observables

This chapter is mostly based on [103] *and in parts inspired by* [102, 104].

So far I discussed how to model the dynamics after the initial collision by fluid dynamics. During the expansion the fluid cools down until the assumption of deconfinement is no longer valid. Instead of free quarks and gluons, the relevant degrees of freedom of the system are hadrons into which the quarks recombine. The temperature at which this effect occurs is known as critical or freeze-out temperature T_{fo} and is of the order $T_{fo} \approx 150\,\mathrm{MeV}$. Given a large enough density immediately after the freeze-out, the hadrons still can be described as expanding fluid. However, since the interactions between the individual hadrons are not as frequent as the interactions between the quarks themselves, the fluid will not remain in chemical equilibrium during the expansion. Finally, the hadrons will be so far apart that the only relevant interactions are resonance decays.
To account for this change in description, the standard procedure in numerical codes is to define a hypersurface of constant temperature, which is chosen to be the freeze-out temperature. This hypersurface is also known as the freeze-out hypersurface. In order to obtain the distribution of hadrons at any given point of the freeze-out surface, it is assumed that the momentum distribution of the outgoing hadrons is the same as the distribution of the particles within the fluid. The entirety of produced particles is then obtained by integrating this hadron distribution function over the full freeze-out surface.
In the following chapter, I will discuss different aspects of the particle production in a heavy-ion collision, starting from the proper definition of the integration over the freeze-out surface via Cauchy surfaces. As a second step I will present a framework to account for the resonance decays of the produced particles on the level of the distribution functions being integrated on the hypersurface. Lastly, I will demonstrate how this is implemented in the Fluid$u$M framework.

4.1. Cooper-Frye freeze-out & thermal spectra

To obtain the integration for the particle spectra on the freeze-out hypersurface, I start with the experimentally measured spectra and go backwards in time:
In a collider experiment particles are measured in the detectors surrounding the collision vertex. Using a collection of these detectors it is possible to measure the particles momenta and sometimes also their energy. The particles detected by such experiments have to be long lived compared to the duration of the initial reaction. In the following I will refer to such particles as stable particles, or out-states. Once these stable particles reach the detector they can be assumed to be non-interacting (with respect to the other particles produced during the collision), free states and therefore can be labeled with a momentum $\mathbf{p}$, an energy E_p and a species index identifying the particle and its quantum numbers. The momentum distribution function

of these particles is given by the number of particles of type i in a momentum shell d^3p

$$\langle E_p \frac{\mathrm{d}N_i}{\mathrm{d}^3p} \rangle. \tag{4.1}$$

This is weighted with the particle energy E_p to obtain a relativistic covariant expression, which is averaged over the events considered. Since all of these particles are assumed to be non-interacting free particles, it is possible to introduce a single particle distribution function $f(x,p)$ as the distribution of the final state particles in momentum space. The previously introduced momentum distribution can then be written as integration over the phase space distribution

$$\langle E_p \frac{\mathrm{d}N_i}{\mathrm{d}^3p} \rangle = -\int_\Sigma \mathrm{d}\Sigma_\mu p^\mu f(x,p). \tag{4.2}$$

Here Σ is a Cauchy hypersurface at a time much larger than any other timescale of the interactions present during the collision. A Cauchy hypersurface is a three-dimensional hypersurface with a future oriented time-like normal vector $\mathrm{d}\Sigma^\mu$ ($\mathrm{d}\Sigma^0 > 0$ and $\Sigma^\mu\Sigma_\mu < 0$). It can be thought of one instant in time. A key observation here is that the contributions to the integration are strictly positive, since $f(x,p) \geq 0$ as distribution function and $-\mathrm{d}\Sigma_\mu p^\mu \geq 0$ as Σ is a Cauchy hypersurface and $p^0 > 0$. In the following I will show that the conservation laws of the system allow for different choices of the hypersurface. These different choices enable the calculation of the particle spectra measured in the detectors directly on the freeze-out hypersurface.
In the limit of free-streaming particles the distribution function obeys the collisionsless Boltzmann equation

$$p^\mu \nabla_\mu f(x,p) = 0, \tag{4.3}$$

with $p^\mu = (E_p, \mathbf{p})$ being the on-shell momentum of the particle. This equation is an evolution equation for the distribution function. The corresponding currents $J^\mu_p = -p^\mu f(x,p)$ are then conserved for each on-shell momentum

$$\nabla_\mu J^\mu_p = 0. \tag{4.4}$$

Therefore, the distribution function is invariant under the transformation $x^\mu \to x^\mu + \tau p^\mu/m$. This ensures that $f(x,p)$ is a distribution function with physical properties, i.e. $f(x,p) \geq 0$ and $f(x,p) = 0$ except when $p^0 > 0$ and $p^2 + m^2 = 0$ hold in all regions which are connected by a free particle trajectory to a point in which these conditions are fulfilled. In order to discuss the different choices of hypersurfaces, it is insightful to first discuss the freeze-out hypersurface itself. An illustration of a typical freeze-out hypersurface can be seen in fig. 20. It is defined by a constant freeze-out temperature and composed of the two curves I and III. Curve IV represents a possible extension of III to form a Cauchy hypersurface. The fireball is created at τ_0 where its corona is given by curve V. The timescale of the lifetime of the fireball is set by τ_L whereas the detector is only reached at $\tau \gg \tau_L$. The black line II is the outward-going part of the lightcone originating

from the outermost point of the fireball. The arrows indicate the direction of the normal vectors $n^\mu \propto \mathrm{d}\Sigma^\mu$.

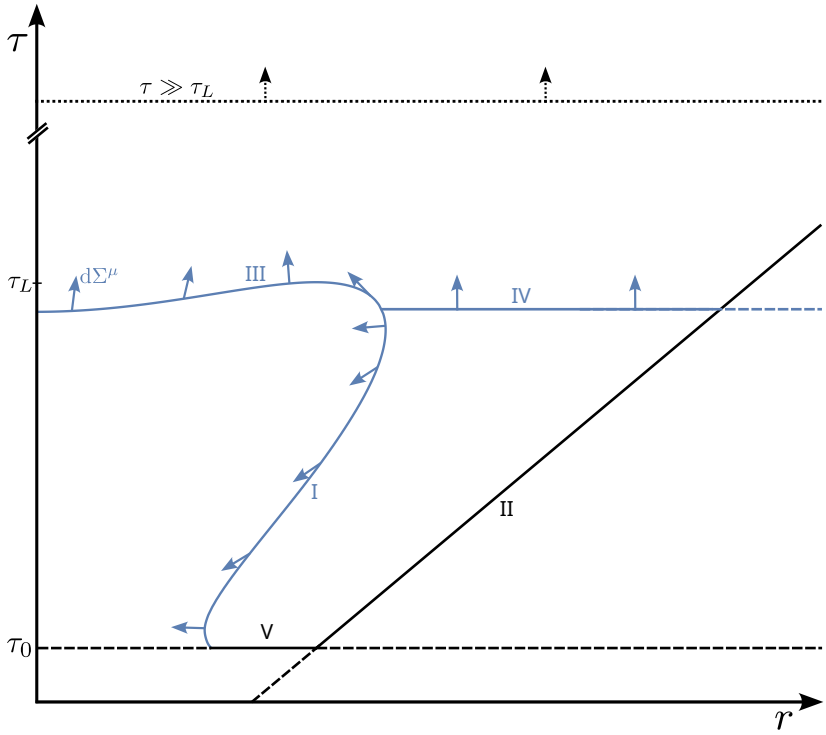

Figure 20: Illustration of a typical freeze-out hypersurface. The freeze-out hypersurface defined by a constant freeze-out temperature is given by the curves I and III. Curve IV represents a possible extension of III to form a Cauchy hypersurface. The lifetime of the fireball is given by τ_L with the dashed line defining the constant time hypersurface at $\tau \gg \tau_L$ at which the detector is located. τ_0 indicates the creation time of the fireball. At this point the corona of the fireball is given by curve V. The black line II is the outward-going part of the lightcone originating from the outermost point of the fireball. The arrows indicate the direction of the normal vectors $n^\mu \propto \mathrm{d}\Sigma^\mu$.

In this picture the fireball lies in the region enclosed by the curves I and III. Outside of this region free streaming is assumed. In the region of a possible corona (region V) a very small, but non vanishing particle density can occur. Since the energy deposited in this corona is small compared to the energy contained inside the plasma, the contribution of the corona to the final hadron spectrum can be neglected. The black line II is the outgoing lightcone originating at the outmost point of the fireball and therefore causally disconnected from the dynamics of the fireball. Therefore, $f(x,p) = 0$ for points on line II and on the right of it. To show that the integration over the hypersurface given by curves I and III and the integration over the dashed constant time hypersurface at $\tau \gg \tau_L$, located at the detector, are equivalent I will introduce an in-between step using curve IV.

I start by looking at the volume Ω enclosed by the time axis, the hypersurface consisting out of III and IV, the lightcone II and the constant time hypersurface at $\tau \gg \tau_L$. Obviously, inside Ω the hadrons are free

streaming, allowing to write

$$\int_{\Omega} \nabla_{\mu} J_p^{\mu} = 0. \tag{4.5}$$

Applying Gauss' theorem and using that the distribution function is zero on the lightcone and the time axis this can be re-expressed as integrations over III and IV and the constant time hypersurface

$$\int_{\Sigma(\tau \gg \tau_L)} \mathrm{d}\Sigma_{\mu} J_p^{\mu} - \int_{\Sigma_{III} \cup \Sigma_{IV}} \mathrm{d}\Sigma_{\mu} J_p^{\mu} = 0. \tag{4.6}$$

Applying the same procedure to the volume enclosed by I, II, IV and V (neglecting the contribution from V, as explained before), yields

$$\int_{\Sigma(\tau \gg \tau_L)} \mathrm{d}\Sigma_{\mu} J_p^{\mu} = \int_{\Sigma_I} \mathrm{d}\Sigma_{\mu} J_p^{\mu} + \int_{\Sigma_{III}} \mathrm{d}\Sigma_{\mu} J_p^{\mu}. \tag{4.7}$$

At this point, there are two important aspects to stress. Firstly, note that all contributions to the two integrations in eq. 4.6 are again positive, since the integrations are being carried out over Cauchy surfaces. This can be thought of as an integration at one moment in time of the particle density to obtain the particle number. The second point to note is that this interpretation is no longer valid after the second step, since curve I is not part of a Cauchy surface. This means that curve I cannot be thought of as an instant of time. Therefore the integrand can also no longer be seen as density, allowing for negative contributions to the integration

$$E_p \frac{\mathrm{d}N}{\mathrm{d}^3 p} = \int_{\Sigma_I} \mathrm{d}\Sigma_{\mu} J_p^{\mu} + \int_{\Sigma_{III}} \mathrm{d}\Sigma_{\mu} J_p^{\mu}. \tag{4.8}$$

This expression can be simplified by combining curves I and III, using the original definition of the freeze-out hypersurface

$$E_p \frac{\mathrm{d}N}{\mathrm{d}^3 p} = \int_{T=const.} \mathrm{d}\Sigma_{\mu} J_p^{\mu}. \tag{4.9}$$

Note that these arguments can be applied in a similar fashion to the two-point function and any higher order correlation function. After showing that the spectra obtained by integrating over the constant temperature freeze-out hypersurface (even if including negative contributions to the integration) are the same as obtained by integrating over a constant time hypersurface at the detector, I now want to discuss how to explicitly carry out this integration and how unstable particles and resonance decays can be incorporated in the model in the next section.

4.2. Particle spectra including resonance decays

At the edge of the fireball and in its final moments, the temperature of the QGP decreases and eventually quarks and gluons become confined again and recombine into hadrons. This process is also known as freeze-

out. Different models of this process have been developed among others by Hagedorn [105, 106], Landau [107] and Milekhin [108]. The standard description, conserving energy, momentum and other conserved quantum numbers, was developed by Cooper and Frye [109] and is of the form discussed in the previous section. In their original work, Cooper and Frye present the calculation of the thermally produced spectra, directly on the freeze-out hypersurface. However, since not all of these produced particles are stable and may decay already within the time of reaching the detector, the spectrum produced on the freeze-out hypersurface is not the same as the spectrum measured in the detectors. A common way of incorporating resonance decays is usually based on Monte-Carlo generators [43, 47, 48, 110], which is numerically costly since all intermediate states of the decay chains appear during the simulation. In the following section I will present a method to calculate the spectra including feed-down from resonances efficiently, based on [104].

4.2.1. Particle production including resonance decays

Generally speaking, the decay probability of particle a into particle b can be computed by integrating over the corresponding scattering matrix element and the available momentum phase space together with the phase space densities of the initial and final states. Obviously, in chemical and kinetic equilibrium the decay $a \to b$ and the inverse reaction $b \to a$ are equally probable. In the case of an expanding medium, as is the case for a heavy-ion collision, the decay will be more probable. After a sufficiently long time all decays will then have taken place. Since the time at which the particles reach the detectors (determined by the detector geometry and the particle velocity) is not large enough for all decays to happen, the individual decays are inherently probabilistic. A saving grace for the calculation is the large number of particles being produced during a heavy-ion collision. This allows to write the spectrum of particle b after the decay as

$$E_p \frac{\mathrm{d}N_b}{\mathrm{d}^3 p} = \int \frac{\mathrm{d}^3 q}{(2\pi)^3 2E_q} D^a_{b|c}(p,q) E_q \frac{\mathrm{d}N_a}{\mathrm{d}^3 q}, \tag{4.10}$$

with $D^a_{b|c}(p,q)$ being the linear decay map giving the Lorentz invariant probability of particle a (having momentum p) decaying into particle b with momentum q. In the following I will assume an isotropic two-body decay $a \to b + c$ for simplicity. The decay operator is then given by

$$D^a_{b|c}(p_\mu q^\mu) = B \frac{4\pi^2 m_a}{p^a_{b|c}} \delta(p_\mu q^\mu + m_a E^a_{b|c}), \tag{4.11}$$

with B being the branching ratio of the process and

$$E^a_{b|c} = \sqrt{m_b^2 + (p^a_{b|c})^2}, \tag{4.12}$$

$$p^a_{b|c} = \frac{1}{2m_a} \sqrt{((m_a + m_b)^2 - m_c^2)((m_a - m_b)^2 - m_c^2)}. \tag{4.13}$$

The assumption of a two-body decay does not loose generality, since the decay operator is linear and decay chains or complicated final states can be accounted for. Three- of more body decays, such as $a \to b + c + d$,

can be accounted for by the introduction of a fictitious particle f with mass $m_f^2 = -(p_c + p_d)^2$. Similarly, a decay cascade $a \to b + c \to c + d + e$ can be accounted for by repeated application of the decay operator

$$D^a_{e|f}(p_\mu q^\mu) = \int \frac{\mathrm{d}^3 k}{(2\pi)^3 2E_k} D^a_{b|c}(p_\nu k^\nu) D^b_{d|e}(k_\nu q^\nu), \tag{4.14}$$

together with the introduction of the fictitious particle $f = c + d$.
Returning to the two-body decay, the vector distribution function g_b^μ of the decay particle b can be written as

$$g_b^\mu(p,\Phi) = \sum_a \frac{\nu_a}{\nu_b} \int \frac{\mathrm{d}^3 q}{(2\pi)^3 2E_q} D^a_{b|c}(p_\nu q^\nu) f_a(-u_\nu q^\nu,\Phi) q^\mu. \tag{4.15}$$

At this point it is important to note that the vector distribution function g_b^μ only depends on the fluid fields Φ on the freeze-out surface[8]. The final particle spectrum is then obtained via

$$E_p \frac{\mathrm{d}N_b}{\mathrm{d}^3 p} = \int_\Sigma g_b^\mu \mathrm{d}\Sigma_\mu. \tag{4.16}$$

In contrast to a spectrum computed via Monte-Carlo methods, the spectrum of particle b is now obtained without the need to compute any intermediate states. The main step remaining is to carry out the integration eq. 4.15 over the decay operator.
The vector distribution function for a primary resonance a in the case of ideal fluid dynamics is given by $g_a^\mu = f_a p^\mu$, with f_a either being a Bose- or a Fermi-distribution $f_a = f_a(E_p,T,\mu_i) = (e^{(E_p - \sum_i Q_{a,i}\mu_i)/T} \pm 1)^{-1}$. Note that this distribution function only depends on Lorentz scalars (the temperature T, chemical potentials μ_i and the particle energy $E_p = -u_\mu p^\mu$ in the frame co-moving with the fluid). The chemical potentials can be conjugated to any conserved charges $Q_{a,i}$, such as baryon numbers, electrical charge etc.
Taking advantage of the Lorentz-invariance of the decay, it is possible to decompose the vector distribution function of the decay product as a sum of two scalar functions

$$g_b^\mu = f^{\mathrm{eq}}_{1,b}(E_p)(p^\mu - E_p u^\mu) + f^{\mathrm{eq}}_{0,b}(E_p) E_p u^\mu. \tag{4.17}$$

Note that since p^μ and $E_p u^\mu$ are the only available Lorentz vectors, this decomposition is unique. Here I introduced the two scalar functions f_s^{eq} with $s = 0,1$, which again only depend on Lorentz scalars. A crucial step in the calculation of the integration over the decay operator is to notice, that the two vectors appearing in the decomposition are actually two irreducible representations of the rotation group $SO(3)$ in the fluid rest frame. The two vectors $\hat{p}^\mu = p^\mu - E_p u^\mu = (0,\mathbf{p})$ and $\tilde{p}^\mu = E_p u^\mu = (E_p,\mathbf{0})$ transform as vector and scalar under $SO(3)$, respectively. Since the decay operator is linear, these two irreducible components do not mix when applying the decay operator, which allows for an individual evaluation of the two terms. I start with

[8] This is later used to define kernels, making the calculation of the final hadron spectra more efficient.

the scalar term proportional to $\tilde{p}^\mu$, reading as

$$E_P u^\mu f_{0,b} = \sum_a \frac{\nu_a}{\nu_b} \int \frac{\mathrm{d}^3 q}{(2\pi)^3 2E_q} D^a_{b|c}(p_\nu q^\nu) u^\mu E_q f_{0,a}, \tag{4.18}$$

where I neglect the arguments of the distribution functions for readability. Often integrations of this type can be simplified by re-introducing the integration over the zero component of the momentum. This often allows for an easier evaluation of the spatial integrations. For the current example, this translates to

$$E_P u^\mu f_{0,b} = \sum_a \frac{\nu_a}{\nu_b} \int \frac{\mathrm{d}^4 q}{(2\pi)^4} \theta(q^0) \delta\left(q^\nu q_\nu + m_a^2\right) D^a_{b|c}(p_\nu q^\nu) u^\mu E_q f_{0,a}. \tag{4.19}$$

Carrying out the integration over the angle φ and q^0 after applying the definition of the decay operator yields

$$E_P u^\mu f_{0,b} = B \sum_a \frac{m_a^2}{m_b^2} \frac{\nu_a}{\nu_b} \int \mathrm{d}q_T^2 \int \frac{\mathrm{d}w}{2\pi} \delta\left(q_T^2 - (1-w^2)(\frac{m_a p^a_{b|c}}{m_b})^2\right) u^\mu E_q f_{0,b}, \tag{4.20}$$

where the substitutions $q^z = w\frac{m_a p^a_{b|c}}{m_b}$ and $q^0 = \frac{m_a E^a_{b|c}}{m_b}$ were used. The final step in this integration is to express E_q in terms of q_T and w, which can be done by first considering the decomposition of q^μ in the restframe of p^μ with respect to u^μ. This decomposition reads as

$$q^\mu = q^\mu_\parallel + q^\mu_T = q^0 \frac{p^\mu}{m_b} + q^z \frac{m_b^2 u^\mu - E_p p^\mu}{m_b p} + q^\mu_T. \tag{4.21}$$

Combining this with the definition of the energy in the restframe of the particle $E_q = -u_\mu q^\mu = -u_\mu q^\mu_\parallel$ allows to write

$$E_q = \frac{m_a E_p E^a_{b|c}}{m_b^2} - w\frac{m_a p p^a_{b|c}}{m_b^2} = E(w). \tag{4.22}$$

Therefore, the q_T integration is trivial to carry out, leaving

$$E_P u^\mu f_{0,a} = B \sum_a \frac{m_a^2}{m_b^2} \frac{\nu_a}{\nu_b} \int_{-1}^{1} \frac{\mathrm{d}w}{2\pi} u^\mu E(w) f_{0,a}(E(w)). \tag{4.23}$$

The final expression for $f_{0,b}$ can now be obtained by contracting both sides with u_μ and dividing by E_P, resulting in

$$f_{0,b} = B \sum_a \frac{m_a^2}{m_b^2} \frac{\nu_a}{\nu_b} \int_{-1}^{1} \frac{\mathrm{d}w}{2\pi} \frac{E(w)}{E_p} f_{0,a}(E(w)). \tag{4.24}$$

Similarly, the integration over the vector component can be re-expressed as

$$f_{1,b} = B \sum_a \frac{m_a^2}{m_b^2} \frac{\nu_a}{\nu_b} \int_{-1}^{1} \frac{\mathrm{d}w}{2\pi} \frac{Q(w)}{|\mathbf{p}|} f_{1,a}(E(w)), \tag{4.25}$$

with

$$Q(w) = \frac{m_a E^a_{b|c} |\mathbf{p}|}{m_b^2} - w \frac{m_a p^a_{b|c} E_p}{m_b^2}. \tag{4.26}$$

This shows that the distribution functions $f_{s,b}$ of the decay products can be calculated from the distribution functions $f_{s,a}$ of the parent particle by this scalar integration. Evidently, this is much simpler than the integration over the full momentum eq. 4.15. The distribution function for a stable particle is then obtained by propagating the decays through the decay chain, starting with the heaviest particle, summing over all particles a that can decay into particle b. This iterative application of the decay operator is depicted in fig. 21 for the decay chain $h_1 \to (\rho,\ \pi) \to \pi$, where all other decays feeding into these particles have been neglected.

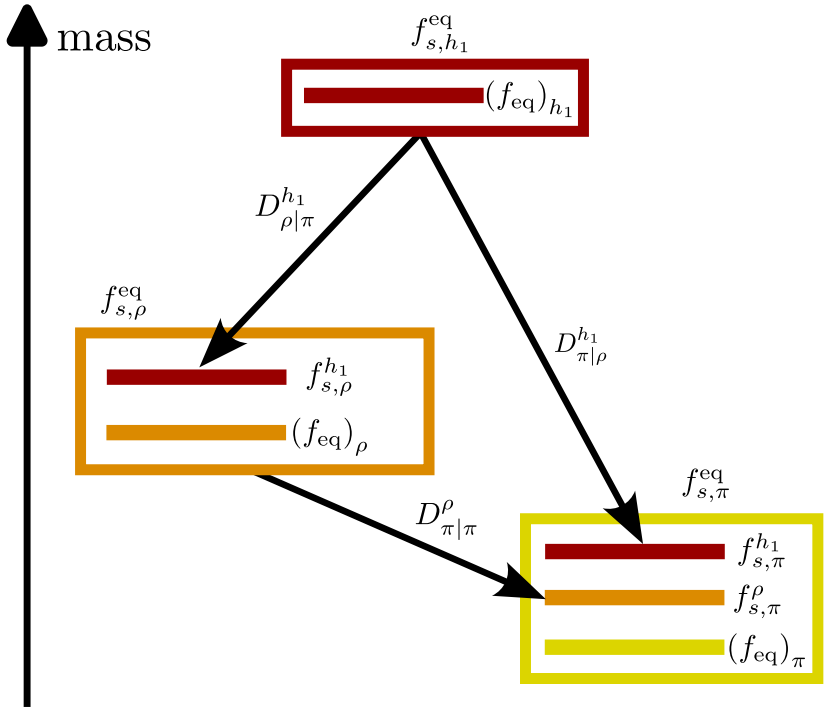

Figure 21: Schematic illustration of the subsequent application of the decay operator. The h_1 distribution is initialized with its thermal distribution (red line), which is also the full distribution function (red box) in this simplified example. The full h_1 distribution then contributes to the ρ and π distribution functions via application of the decay operator. The full ρ distribution function (orange box) is then given by the sum of the thermal ρ distribution function (orange line) and the contributions from the h_1 decay (red line). Similarly the full pion distribution function (yellow box) is given by the sum of the thermal pions (yellow line) and the contributions from the h_1 and ρ decays (red and orange lines).

Since there are no resonances feeding down into the h_1 resonance in this example, the distribution function is only given by the thermally produced h_1

$$f^{\mathrm{eq}}_{s,h_1} = (f_{\mathrm{eq}})_{h_1}\,, \tag{4.27}$$

where f_{eq} is a Bose-Einstein distribution, since the h_1 is a meson. Employing the previously established transformation rules for the distribution functions allows to calculate the feed down from the h_1 resonance into the π and the ρ. Since the ρ itself is not a stable particle, the decay operator has to be applied once more to account for the decay $\rho \to \pi\pi$. To get the full contribution from this decay to the pion spectrum, the decay operator has to be applied to the full ρ distribution function, i.e. the sum of the thermally produced ρ and the ρ stemming from h_1 decays. The final distribution functions for the ρ and the π are then given by

$$f^{\mathrm{eq}}_{s,\rho} = (f_{\mathrm{eq}})_{\rho} + f^{h_1}_{s,\rho}, \tag{4.28}$$

$$f^{\mathrm{eq}}_{s,\pi} = (f_{\mathrm{eq}})_{\pi} + f^{h_1}_{s,\pi} + f^{\rho}_{s,\pi}. \tag{4.29}$$

In this case $f^{\rho}_{s,\pi}$ represents all contributions from ρ decays to the pion distribution function, irrespective of their origin. For practical calculations with larger decay lists, the decay operator is applied to all the particles, starting from the heaviest resonance, propagating down the feed downs to the lighter particles.
This concludes the discussion on the concept of including resonances into the description of the freeze-out during a heavy-ion collision. In the next section this concept is applied to the mode-by-mode fluid dynamics developed in the previous chapter.

4.2.2. Application to mody-by-mode fluid dynamics

For reasons of simplicity, the discussion presented in the previous chapter was limited to ideal fluid dynamics. This is an insufficient description of a heavy-ion collision, due to the absence of viscous corrections. Evidently, the presence of the viscous fields modifies the distribution function. The concrete form of this modification is non-trivial and a topic of current research. In the following I will assume that the modifications to the equilibrium distribution function are small and can be expressed as linear deviations. The distribution function is then given by

$$f(\Phi) = f_{\mathrm{eq}}(\beta,v,\alpha) + \Delta f_{\mathrm{shear}} + \Delta f_{\mathrm{bulk}} + \Delta f_{\mathrm{diff}}, \tag{4.30}$$

where I included corrections arising from the presence of shear and bulk viscosity, as well as a baryon number diffusion current. These corrections are linear in their respective dissipative fields. The inclusion of additional corrections arising from e.g. electric charge conservation is straight forward. This distribution function only depends on the fluid fields on the freeze-out hypersurface, but not on their concrete evolution. This makes it possible to compute the decay chains presented above only once and tabulate the resulting distribution functions. Using these tabulated distribution functions the integration over the freeze-out hypersurface can in parts already be computed in advance, speeding up the actual fluid dynamic simulation.
At this point it is important to stress a key point arising in the setting of linearized fluid dynamics. The corrections Δf to the distribution functions and the perturbations $\delta\Phi$ of the fluid fields are fundamentally different. Regardless of the magnitude of the dissipative fields, they always can be split in a symmetric background with perturbations around it. To obtain a consistent description in this setting of linearized fluid dynamics, it is necessary to apply the background-fluctuation splitting also to the Δf corrections of the distribution functions, leading to Δf_i terms proportional to $\delta\Phi$. However, this is not the same as $(\delta\Phi)^2$.
In the following I will use the standard forms, used in almost all state-of-the-art fluid-dynamic simulations, for the out-of-equilibrium corrections [42], given by

$$\Delta f_{\mathrm{shear}} = f_{\mathrm{eq}}(1 \pm f_{\mathrm{eq}}) \frac{p_\mu p_\nu \pi^{\mu\nu}}{2(e+p)T^2}, \tag{4.31}$$

$$\Delta f_{\mathrm{bulk}} = f_{\mathrm{eq}}(1 \pm f_{\mathrm{eq}}) \left[\frac{E_p}{T}\left(\frac{1}{3} - c_s^2\right) - \frac{1}{3}\frac{m^2}{TE_p} \right] \frac{\tau_B \pi_B}{\zeta}, \tag{4.32}$$

$$\Delta f_{\mathrm{diff}} = f_{\mathrm{eq}}(1 \pm f_{\mathrm{eq}}) \left[\frac{n_B}{e+p} - \frac{Q_B}{E_P} \right] \frac{\nu^\mu p_\mu}{\kappa}. \tag{4.33}$$

Here m is the mass of the primary resonance, c_s^2 is the speed of sound, τ_b/ζ is the ratio of the bulk relaxation time and bulk viscosity and n_B and Q_B are the baryon density and baryon charge respectively, together with the baryon diffusion coefficient κ. Since these corrections modify the distribution function, the vector distribution function evidently changes as well

$$g^\mu = g^\mu_{\text{eq}} + g^{\mu\nu\rho}_{\text{shear}}\pi_{\nu\rho} + g^\mu_{\text{bulk}}\pi_B + g^{\mu\rho}_{\text{diff}}\nu_\rho, \tag{4.34}$$

where the concrete form of the each correction can be obtain by comparing with the corresponding Δf_i, e.g. $g^{\mu\nu\rho}_{\text{shear}}\pi_{\nu\rho} = \Delta f_{\text{shear}} p^\mu$. As before, it will be very valuable to consider the decomposition of the corrections under $SO(3)$ when applying the decay operator. Since multiple particle momenta appear in the Δf_i, higher order tensor of the particle momentum, such as $p^\mu p^\nu p^\rho$ or even $p^\mu p^\nu p^\rho p^\sigma$ have to be decomposed. A systematic way of obtaining the required tensor decompositions is the substitution of the one-tensor decomposition $p^\mu = \tilde{p}^\mu + \hat{p}^\mu$ for each appearing momentum. For higher order tensors this will generate terms, such as $\hat{p}^\mu\hat{p}^\nu$, which are not irreducible. Since $\hat{p}^\mu\hat{p}^\nu$ is symmetric, removing its trace will yield the correct irreducible representation of $SO(3)$ (symmetric and traceless tensors are irreducible representations of $SO(3)$). The full tensor decompositions for p^μ, $p^\mu p^\nu$, $p^\mu p^\nu p^\rho$ and $p^\mu p^\nu p^\rho p^\sigma$ are given in appendix B. With these tensor decompositions at hand, the inclusion of any additional term can be done by considering the underlying tensor structure:
Considering the equilibrium contribution g^μ_{eq} and the bulk correction $g^\mu_{\text{bulk}}\pi_B$, it is obvious that both terms can be re-written as jp^μ where j is a scalar prefactor consisting out of e.g. the distribution function f_{eq}, and combinations of particle mass, temperature, bulk viscosity etc., appearing in the bulk contribution. Therefore, both terms share the same Lorentz tensor structure (while having a different j as prefactor) and subsequently also share the same tensor decomposition. Absorbing the different prefactors j into the distribution functions then gives the same structure in the integration over the freeze-out surface

$$E_p\frac{\mathrm{d}N_b}{\mathrm{d}^3p} \propto \int_\Sigma \left(f_{1,b}(E_p)(p^\mu - E_p u^\mu) + f_{0,b}(E_p)E_p u^\mu\right)\mathrm{d}\Sigma_\mu. \tag{4.35}$$

In this case the $f_{s,b}$ are the prefactors j after applying the transformations to account for resonance decays. Obviously the equilibrium contribution of the spectrum and the bulk correction to it share the same integration kernel, with only the scalar distribution functions being different. This, of course, also holds for terms that are proportional to a higher order tensor in the particle momenta. Exceptions to this statement can arise, when considering fields with varying symmetries, such as the shear stress tensor: The correction proportional to the shear stress tensor is a Lorentz-three tensor $p^\mu p^\nu p^\sigma$, where two of the indices are being contracted with the shear stress tensor itself. When applying the linearization of the fluid fields to this object, a contraction with the background part $p^\mu p^\nu p^\sigma \bar{\pi}_{\nu\sigma}$ and a contraction with the perturbation part $p^\mu p^\nu p^\sigma \delta\pi_{\nu\sigma}$ of the shear stress tensor is generated. Applying the tensor decomposition of $p^\mu p^\nu p^\sigma$ to both cases will yield more non-zero terms for the perturbation case, since the background part of the shear stress tensor is orthogonal to the background fluid velocity $\bar{\pi}^{\mu\nu}\bar{u}_\mu = 0$, whereas the perturbation part is not $\delta\pi^{\mu\nu}\bar{u}_\mu \neq 0$.

With a recipe at hand for treating corrections proportional to up to four particle momenta, I now combine this method of treating the particle production with resonance decays with the linearized fluid dynamics. To obtain a consistent description, the background-fluctuation splitting of course also needs to be applied on the level of the freeze-out integration. Therefore, the final hadron spectrum can be written as

$$\frac{\mathrm{d}N}{p_T \mathrm{d}p_T \mathrm{d}\phi_P \mathrm{d}\eta_P} = \frac{\mathrm{d}\bar{N}}{2\pi p_T \mathrm{d}p_T \mathrm{d}\eta_P} + \frac{\delta \mathrm{d}N}{p_T \mathrm{d}p_T \mathrm{d}\phi_P \mathrm{d}\eta_P}. \tag{4.36}$$

Formally both appearing terms need to be integrated over the full freeze-out surface. Employing the hypersurface element given in eq. 3.39 in the integration over the freeze-out hypersurface, allows to precompute the azimuthal and rapidity integration, only leaving the integration over the parameter c to be carried out. The precomputed integrations can be stored as function of the fluid fields and the mean transverse momentum and are referred to as kernels. This integration has to be carried out for each fluid evolution individually, since the values of the fluid fields on the freeze-out surface, as well as the freeze-out hypersurface itself might change. After carrying out these integrations, the background spectrum is given by

$$\begin{aligned}
\frac{\mathrm{d}\bar{N}}{2\pi p_T \mathrm{d}p_T \mathrm{d}\eta_P} &= \frac{\nu}{(2\pi)^3} \int_0^1 \mathrm{d}c \tau(c) r(c) \\
&\left(\frac{\partial r}{\partial c} \left[K_1^{\mathrm{eq}} + \frac{\bar{\pi}^{22}}{2(e+p)T^2} K_1^{\mathrm{shear}} + \frac{\bar{\pi}^{33}}{2(e+p)T^2} K_3^{\mathrm{shear}} + \bar{\Pi} K_1^{\mathrm{bulk}} + \bar{\gamma}\bar{\nu} K_1^{\mathrm{diff}} \right] \right. \\
&\left. - \frac{\partial \tau}{\partial c} \left[K_2^{\mathrm{eq}} + \frac{\bar{\pi}^{22}}{2(e+p)T^2} K_2^{\mathrm{shear}} + \frac{\bar{\pi}^{33}}{2(e+p)T^2} K_4^{\mathrm{shear}} + \bar{\Pi} K_2^{\mathrm{bulk}} + \bar{\gamma}\bar{\nu} K_2^{\mathrm{diff}} \right] \right).
\end{aligned} \tag{4.37}$$

Here the K_i^a are the aforementioned kernels. Since these kernels only depend on the background fluid velocity and the transverse momentum, they can be precomputed and stored. A similar expression can be obtained for the perturbation spectrum, reading

$$\frac{\delta \mathrm{d}N}{p_T \mathrm{d}p_T \mathrm{d}\phi_P \mathrm{d}\eta_P} \propto \frac{\partial f_{\mathrm{eq}}}{\partial \Phi_i} \delta\Phi_i + \frac{\partial \Delta f_{\mathrm{shear}}}{\partial \Phi_i} \delta\Phi_i + \frac{\partial \Delta f_{\mathrm{bulk}}}{\partial \Phi_i} \delta\Phi_i + \frac{\partial \Delta f_{\mathrm{diff}}}{\partial \Phi_i} \delta\Phi_i, \tag{4.38}$$

where a shorthand notation for the perturbations has been introduced. The full expressions for the kernels, especially for the perturbation kernels, are quite lengthy and can be found in [103]. A detailed discussion on how to use these perturbation kernels to calculate the flow coefficients can be found in [102]. Note that an interesting special case can be easily obtained from these kernel expression: If the decay operator is not applied to the distribution functions, the spectra thermal without resonance decays are calculated. In the presented setting this can be achieved by simply setting $f = f_i$ for all $i = 0,1,2,\ldots$ appearing in the tensor decomposition, with f being the initial distribution function for the respective contribution. This can either be done on the level of the numerical implementation or before, during the calculation of the kernel expressions. If done during the calculation of the kernel expressions, it leads to a massive simplification, even allowing for the analytic calculation of the ϕ- and η-integrations, as was shown in [102, 103].
So far all calculations in this chapter have been done with the implicit assumption that the freeze-out

happens at one temperature. At this temperature the distribution function of the hadrons freezes out instantaneously, fixing the chemical and kinetic composition of the produced hadrons. This simultaneous freezing-out of the chemical and kinetic distribution is not necessarily the case. At some point during the expansion of the fireball hadrons are produced, as described before. Initially these hadrons are still dense enough to scatter amongs each other. Since the temperature is already quite low, the inelastic scatterings changing the chemical composition of the produced hadrons become increasingly inefficient, resulting in the freeze-out of the chemical composition. At this point the hadrons still scatter elastically, changing their kinetic distribution. After a while the density of the hadron gas becomes low enough for the elastic collisions being no longer effective. At this point the kinetic distribution of the hadrons also is frozen out. This separation into a chemical and kinetic freeze-out is known as partial chemical equilibrium (PCE) [45, 46]. Even though the chemical composition of the system is not changed anymore by inelastic scatterings, it still is changed by resonance decays. Since the system still expands the loss of chemical equilibrium leads to a build up of chemical potentials conjugated to the number densities of the produced hadrons. These chemical potentials are not independent of each other, because the hadron can decay in each other linking the chemical potentials along the decay chains. Using the lowest order of the gradient expansion of the fluid dynamic equations, an implicit evolution equation for the chemical potentials can be derived based on the conservation of the entropy per particle number (for details see [46, 103, 111]).

A comparison between the thermal spectra and the spectra including resonance decays for pions, kaons and protons can be seen in fig. 22. Additionally, the spectra calculated including a PCE phase are shown. The inclusion of resonance decays leads to an increase of the produced pions, kaons and protons. This increase is of similar magnitude for all three particles, with the largest increase being found for the low p_{T} pions. As lightest stable particle this increase for low transverse momenta is expected.

When considering the spectra with the inclusion of the PCE, it can be seen that the impact here is bigger for protons compared to the other particles. This can be attributed to the lower number of protons being produced. Therefore the impact of a few extra produced protons is bigger.

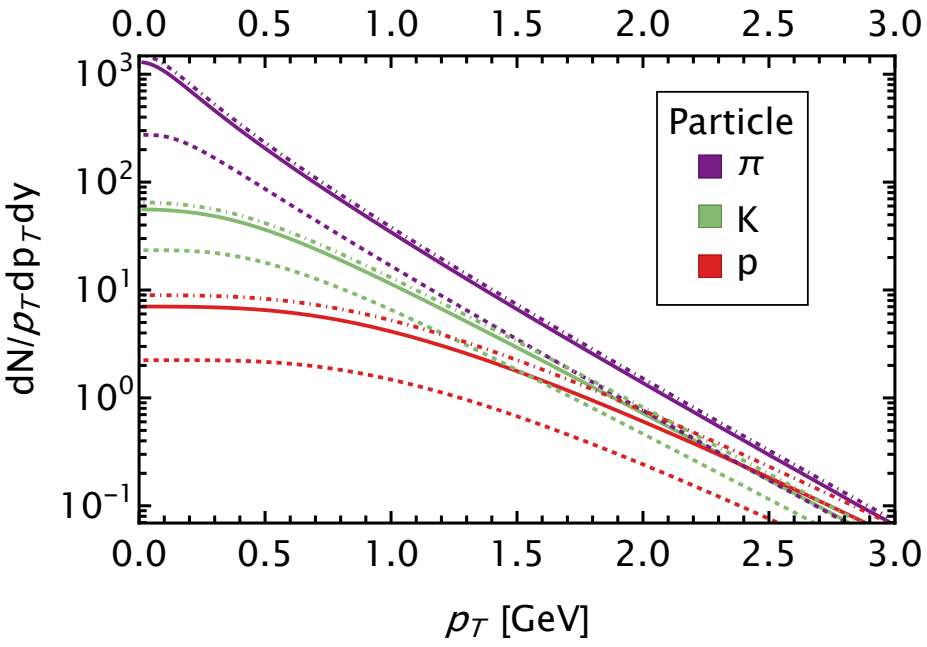

Figure 22: Comparison of the pion, kaon and proton spectra with (solid lines) and without (dashed lines) resonance decays. Additionally the spectra with resonance decays and PCE are shown (dash-dotted lines).

5. Applications of mode-by-mode fluid dynamics

This chapter is mostly based on [51, 53, 112].

In this chapter I to present three different applications of the Fluid$u$M framework: In the first application Fluid$u$M was used for a Bayesian parameter extraction of QGP parameters. For the second application Fluid$u$M was used to provide the spectra of neutral particles needed for the experimental analysis of direct photons. The last application presented here is a study on the interplay of nuclear structure and heavy-ion collisions. All of these applications make use of the flexibility of the Fluid$u$M framework, e.g. allowing for the quantification of theoretical model uncertainties as part of the Bayesian parameter extraction. Before going into the details of the individual applications, I want to present a short comparison of the Fluid$u$M framework with the framework presented in [113] as validation.

5.1. Framework validation

Since Fluid$u$M is fundamentally different from event-by-event frameworks, it is useful to compare the two different approaches. For this the framework presented in [113] by the Duke group has been chosen. It is an event-by-event framework combining initial conditions generated by T$_\mathrm{R}$ENTo [34] with the fluid evolution simulated by VISH2+1 [114]. This model includes a switching temperature T_switch at which the system switches from evolving the QGP to an evolution of hadrons carried out by UrQMD [48, 115]. The transition from quarks and gluons to hadrons is based on the Cooper-Frye prescription. The optimal parameters for the framework to reconstruct the spectra and flow coefficients, measured at Pb-Pb collisions at $\sqrt{s} = 2.76\,\mathrm{TeV}$, were obtained by Bayesian inference using a Gaussian process emulator together with Markov-Chain Monte-Carlo methods. To compare the best fit results obtained in this way, the best fit values of the Duke analysis for identified particles were used in Fluid$u$M. The results for the multiplicity and the mean transverse momentum[9] can be seen in fig. 23.

[9] The flow coefficients also have been examined in [113], but are not of interest for now, since all three following applications of Fluid$u$M only use the background configuration.

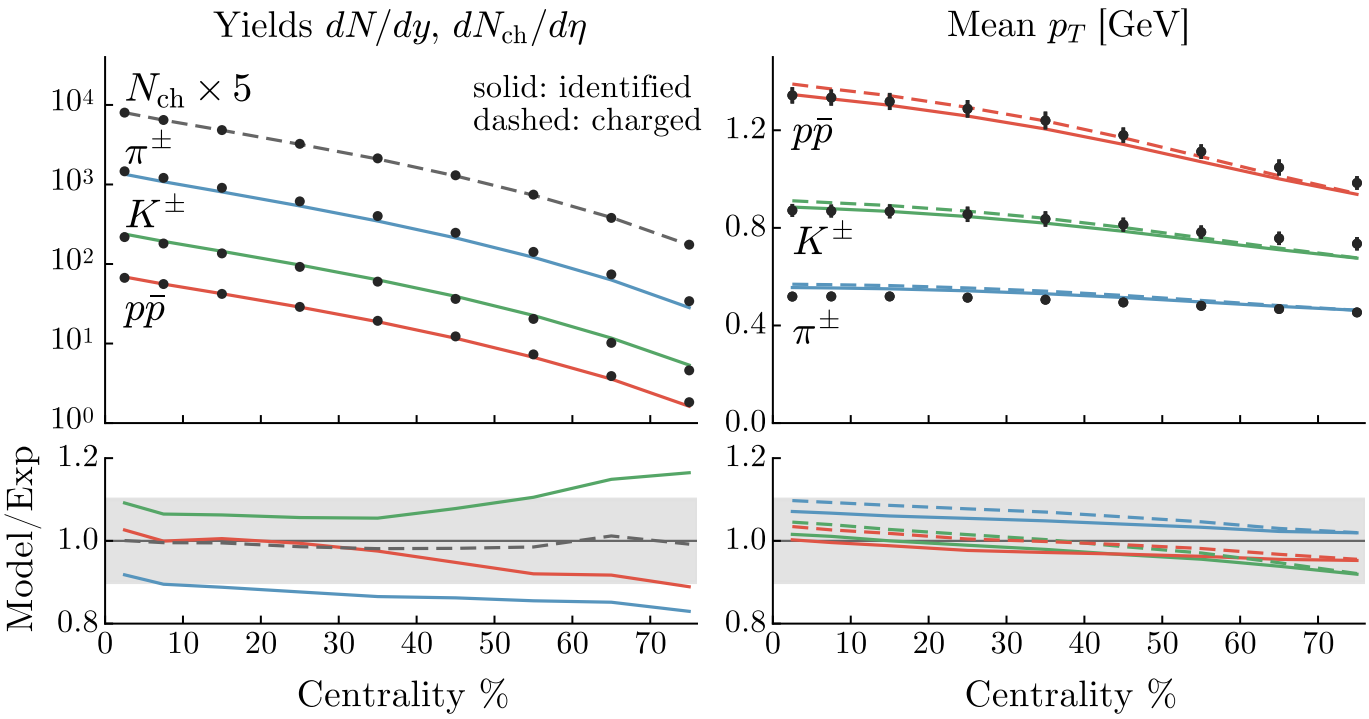

Figure 23: Model calculations using the best fit parameters, taken from [113]. The left top panel shows the yields as function of the centrality, with the model to data ratio being shown in the bottom left panel. The right panels show the mean transverse momentum and its model over data ratio, respectively. The points are experimental data taken by ALICE while the lines are theory calculations from the Duke analysis.

The results for the same quantities, calculated with the best fit parameters from [113], but using the above described Fluid$u$M framework can be seen in fig. 24. A first key point in the comparison between the Fluid$u$M results and the experimental data is, that the charged particle yields are reproduced very well, with the model to data ratio being almost flat around unity. A similar behavior can be seen in the charged particle yield of the Duke group. Turning to the charged particle yields, a first difference of the two frameworks becomes apparent: While the Duke results overestimate the kaons and underestimate the pions, with the protons only being slightly underestimated, the Fluid$u$M results behave fundamentally different. They show the same ordering of the particles in the ratio, with all the ratios being shifted up. As a consequence, the pions are captured better, remaining within the 10% band for the full centrality range. However, the deviations of the pion and proton ratios are further away from unity, with only the proton yield ratio entering the 10% deviation band at approximately 35% centrality. A similar trend also shows when considering the mean transverse momentum. The best fit results obtained by the Duke group all lie within the 10% deviation band with the ratios being ordered as pions, kaons and then protons. The Fluid$u$M ratios show the same ordering, shifted down when compared to the Duke results. This leads to a bigger underestimation of the kaon and proton mean transverse momenta.

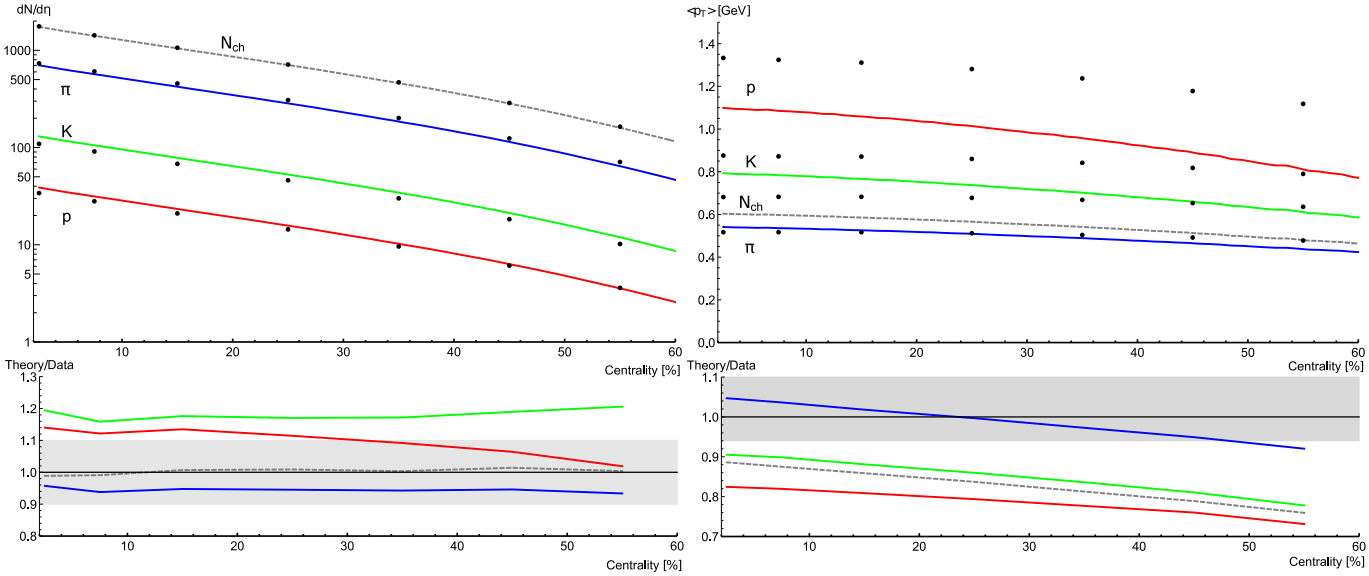

Figure 24: Comparison of identified particle and charge particle yields and mean transverse momenta as function of centrality with experimental data (points). The parameters for the simulation are the same as the best fit parameters obtained in [113]. The model over data ratios for yields and mean transverse momenta show the same tendencies and ordering as the Duke results (fig. 23), while generally being further away from unity. These differences can be attributed to the use of the hadronic afterburner in the Duke framework, not being used in Fluid*u*M.

These discrepancies between the two models can be attributed to the main difference between the frameworks. While Fluid*u*M accounts for resonance decays, it currently has no hadronic afterburner implemented[10]. The Duke framework simulates the hadronic rescattering phase with the UrQMD afterburner. Since UrQMD uses Monte Carlo techniques to solve the Boltzmann equation, it is difficult to combine with Fluid*u*M. The reason for this lies in the nature of Fluid*u*M, which calculates a continuous distribution of the final state hadrons, instead of a discrete set of hadrons with their momenta. However, the impact of an afterburner has been studied in [116] and is shown in fig. 25 for the identified yields and mean transverse momenta. The yield and mean transverse momentum of pions with (solid line) and without (dashed line) the afterburner are very similar. Contrary, the yields of kaons and protons are slightly decreased by the afterburner. The mean transverse momentum of the kaons and protons are influenced heavily by the afterburner, increasing especially much for the protons. These effects of increased mean transverse momentum and decreased yields, especially for protons and kaons, account for the difference in results between the Fluid*u*M and Duke frameworks.

[10] A hadronic afterburner accounts for the scatterings occurring after the freeze-out. These re-scatterings can be mimicked by the inclusion of a PCE phase, which was not done in this analysis.

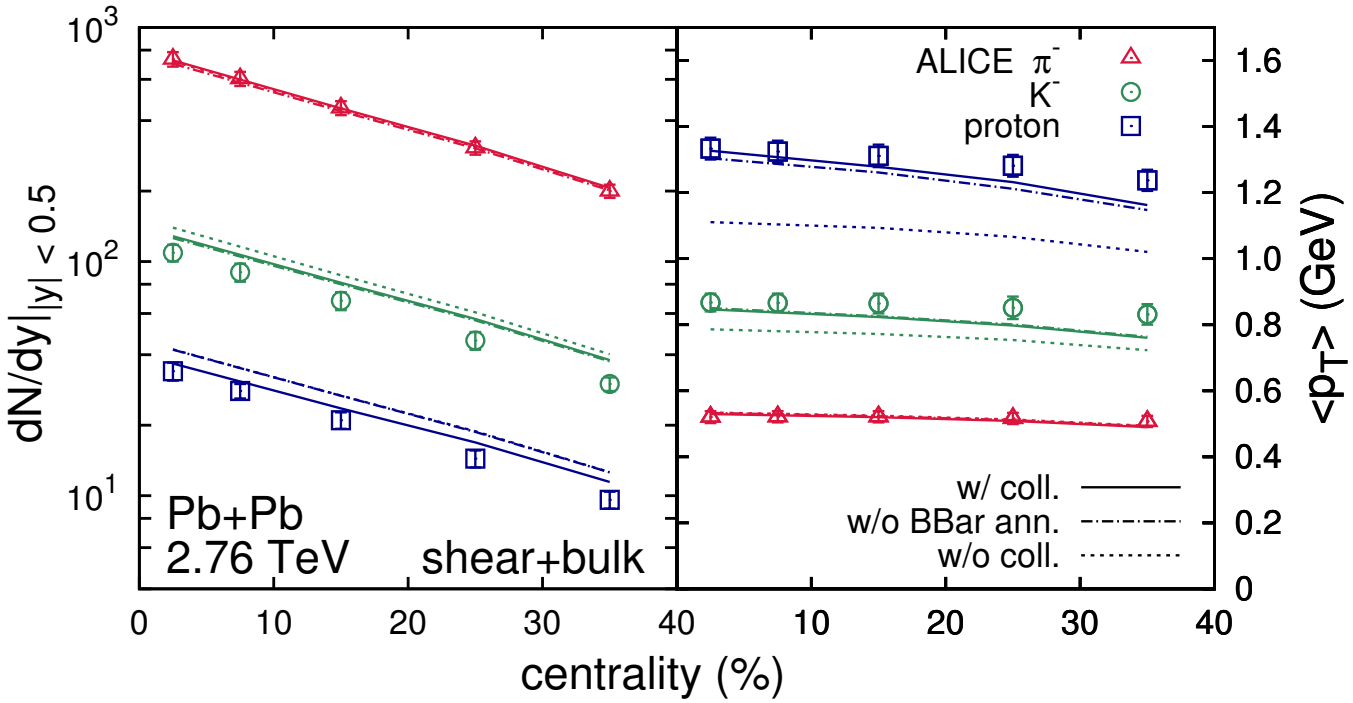

Figure 25: Impact of an afterburner on the identified particle yields and mean transverse momenta for pions, kaons and protons, taken from [116]. The increase in transverse momenta and decrease in yields, especially for kaons and protons, accounts for the differences in results between the Fluid$u$M and Duke frameworks.

5.2. Bayesian parameter extraction

The recent increase in precision of experimental measurements of heavy-ion collisions [117, 118] allows for a more thorough comparison of theoretical calculations and the experimental measurements [113, 119, 120], as well as a more precise parameter extraction of the QCD liquid. This parameter extraction can be realized in various ways by comparing the theoretical calculations with experimental measurements and minimizing the goodness of the fit. To determine this goodness of the fit, various methods can be applied. In the past Fluid$u$M was used together with a classical χ^2 minimization to determine the set of model parameters optimally describing the experimental data [121]. Recently, it has been demonstrated that deep learning and Bayesian analysis show great potential to extract more information from the experimental data. In the following I will give a brief overview of the model based on Bayesian parameter extraction, developed in [112].

The theoretical simulation of the events is carried out by the combination of T$_\mathrm{R}$ENTo + Fluid$u$M + FastReso, as presented in the previous part of this work. The free parameters are the overall normalization of the initial entropy density Norm, the $(\eta/s)_\mathrm{scale}$ and $(\zeta/s)_\mathrm{max}$ from the parametrizations of the viscosities, the initialization time for the fluid dynamics τ_0 and the two freeze-out temperatures T_chem and T_kin. Since the

fit is performed simultaneously on three data sets (Pb-Pb@2.76 TeV, Pb-Pb@5.02 TeV, Xe-Xe@5.44 TeV) the norm and initialization time will depend on the system while the other parameters are system independent. The ranges for the free parameters are reported in tab. 2. The remaining T$_\mathrm{R}$ENTo parameters are taken to be $w = 0.5\,\mathrm{fm}$, $m = 4$, $v = 0.4\,\mathrm{fm}$, $p = 0$, $k = 1$ and $v = 0.75\,\mathrm{fm}$.

	$(\eta/s)_{\mathrm{scale}}$	$(\zeta/s)_{\mathrm{max}}$	T_{kin} [MeV]	T_{chem} [MeV]	Norm	τ_0 [fm/c]
Pb-Pb (2.76 TeV)					$5-80$	$0.01-3.0$
Pb-Pb (5.02 TeV)	$0.08-0.52$	$10^{-4}-0.3$	$110-140$	$130-155$	$80-140$	$2.0-7.0$
Xe-Xe (5.44 TeV)					$70-150$	$2.0-7.0$

Table 2: Ranges for the six free parameters of the fit.

Since the Bayesian analysis requires extensive exploration of the free parameters it is beneficial to develop an emulator for the T$_\mathrm{R}$ENTo + Fluid$u$M + FastReso framework, despite the inherent speed of Fluid$u$M. A very popular choice for the emulator is a Gaussian process emulator. However, in [112] an ensemble of neural networks was first used as emulator for the fluid-dynamic simulations. Details on the architecture, training and verification of the neural network can be found in the provided reference.
This fast emulator can now be used to infer the posterior probability distributions of the free parameters using the experimental data and Bayes theorem. A suitable method for this is the so called Markov-Chain Monte-Carlo algorithm. The mean values of the resulting probability distributions together with the according 68% confidence intervals are reported in tab. 3. The shear viscosity remains unconstrained by the fit, because the observables chosen for the fit only have very limited dependence on the shear viscosity. Comparisons of these best fit parameters with the results of different frameworks can be found in [112].

	$(\eta/s)_{\mathrm{min}}$	$(\zeta/s)_{\mathrm{max}}$	T_{kin} [MeV]	T_{chem} [MeV]	Norm	τ_0 [fm/c]
Pb-Pb (2.76 TeV)					$36.0^{+3.1}_{-3.6}$	$0.76^{+0.21}_{-0.23}$
Pb-Pb (5.02 TeV)	unconstr.	$0.083^{+0.012}_{-0.012}$	122^{+2}_{-1}	141^{+0}_{+0}	$109.0^{+4.5}_{-4.1}$	$3.66^{+0.3}_{-0.3}$
Xe-Xe (5.44 TeV)					$103.7^{+4.6}_{-4.6}$	$3.01^{+0.31}_{-0.31}$

Table 3: Best fit parameters with uncertainties for a simultaneous fit of all three collision systems. The best values and their uncertainties are the mean values and 68% confidence intervals from the final probability distributions. The shear viscosity remains unconstrained by the fit, because the observables chosen for the fit only have very limited dependence on the shear viscosity.

So far there is no crucial difference to previously carried out parameter extractions. However, the speed of Fluid$u$M and the neural network emulator allow for an additional evaluation of the model itself by varying different parts of it and redoing the whole fitting procedure. Among these variations are the restriction of the experimental data used to only a subset of the data (e.g. taking only the pion and kaon data into account), as well as the inclusion of additional free parameters (e.g. the shear relaxation time). A summary of the results with these variations is presented in fig. 26. The impact of the changes can be seen when plotting the various best fit results for each of the cases against the experimental data, as shown in fig. 26. The best

fit values agree in most cases. Notable deviations arise when including low momentum pions and increasing the upper p_{T} cut on the experimental data. Both of these deviations are expected, since the enhancement of low-momentum pions is believed to come from a non-fluid-dynamic origin. The deviation in especially the shear viscosity for the inclusion of higher momentum particles is accounted for by the proportionality of the shear correction to p_{T}^2. Therefore, the high momentum points are more sensitive to this parameter, leading to a larger change.

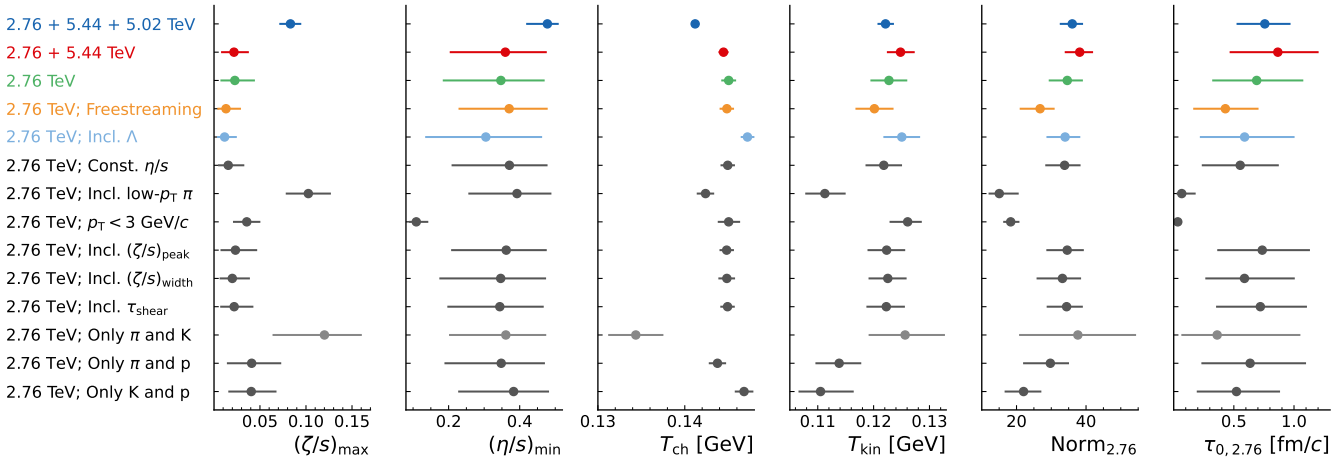

Figure 26: Mean values together with the corresponding 68% confidence intervals for all analyzed configurations of the model. The best fit values agree in most cases. Notable examples are the inclusion of low momentum pions and increasing the upper p_{T} cut on the experimental data.

To illustrate the values reported in fig. 26, the p_{T} spectra for pions, kaons and protons for the three examined collision systems in the $0-5\%$ centrality class are plotted in fig. 27. The top panels display the transverse momentum spectra, whereas the bottom panels show the ratio between theory and experimental data. The uncertainty bands are generated from the fit results of the different configurations from fig. 26. These theory uncertainties are around 20% for the Pb-Pb at 2.76 TeV and around 40% for the other two collision systems. This increase in the theoretical uncertainty can be attributed to the fact, that the model variations were carried out for the Pb-Pb@2.76 TeV system.

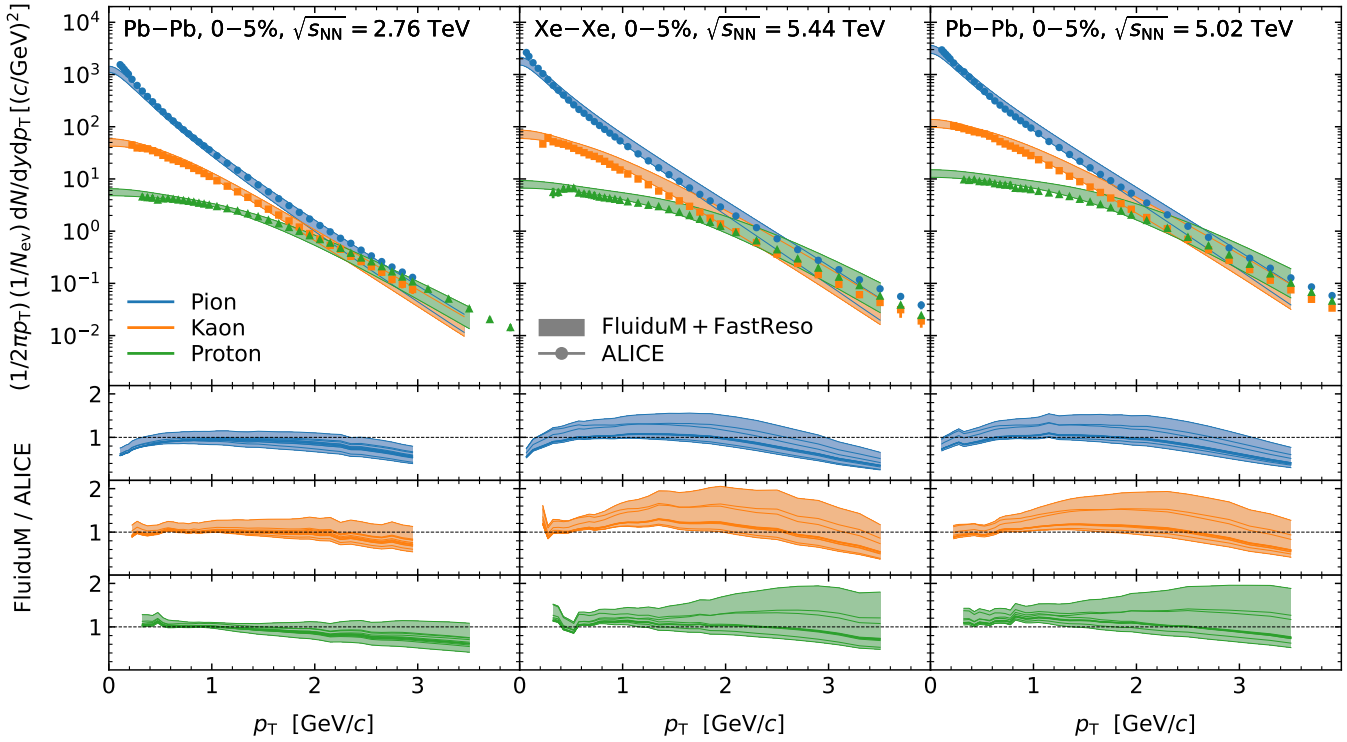

Figure 27: Comparison of experimental data and Fluid*u*M+FastReso calculations evaluated with the best fit parameters (top row) from fig. 26. The top panels display the transverse momentum spectra, whereas the bottom panels show the ratio between theory and experimental data.

5.3. Direct photon analysis

One of the main ways of gaining direct access to the evolution of the QGP is the measurement of direct photons as they are produced during all stages of the collision and are unaffected by hadronization. Additionally, the spectrum of the thermal photons allows to gain insight on the temperature of the medium. However, measuring the spectrum of the direct photons is rather challenging due to a large background from decay photons. The most dominant contributions to this background are the decay of the neutral pion $\pi^0 \to \gamma\gamma$ and the decay of the η-meson $\eta \to \gamma\gamma$. Together, these two decays constituent about 98% of the decay-photon background [122]. Since the π^0 and the η are neutral particles, their measurements are difficult and typically associated with larger uncertainties (especially for the η). Therefore, most experimental measurements of the direct photon spectrum model the η spectrum, especially at low p_T. Among the previously used models for predicting the η/π^0 are e.g.

- **m_T-scaling**: The m_T scaling hypothesis assumes that different particle species share the same spectra shape as function of m_T and only differ in their normalization constant. This has been used by the WA98 experiment at the CERN SPS [123] and the PHENIX experiment at RHIC [124].

- **Tsallis blast wave fits**: The STAR experiment used a Tsallis blast wave fit to account for radial flow

[125].

- **pp scaling**: Ren and Drees proposed a method based on the rescaling η/π^0 ratio measured in pp collisions [126] by multiplying by the K/π ratios $\eta/\pi^0|_{\mathrm{AA}} = \frac{K/\pi|_{\mathrm{AA}}}{K/\pi|_{\mathrm{pp}}}\,\eta/\pi^0|_{\mathrm{pp}}$.

All of these models are not based on a full fluid-dynamic simulation. Therefore, to acquire a more precise model, Fluid*u*M was used to search for a predictor for the η/π^0 ratio. The most obvious choice is to simply use the parameters obtained in [112] and predict the η/π^0 ratio from this. However, it turns out that a data-driven ansatz taking the experimentally measured data into account minimizes the model dependence. In this ansatz the η/π^0 ratio is predicted to be

$$\eta/\pi^0|_{\mathrm{AA}} = \frac{\eta/\pi^0|_{\mathrm{hydro}}}{K/\pi|_{\mathrm{hydro}}}\,K/\pi|_{\mathrm{AA,meas}}. \tag{5.1}$$

This ansatz has two main benefits. On the one hand, using the double ratio $(\eta/\pi^0|_{\mathrm{hydro}})/(K/\pi|_{\mathrm{hydro}})$ instead of using directly the η/π^0 from Fluid*u*M minimizes the model dependence. On the other hand, this ansatz makes use of the K/π ratio that can be measured with much higher accuracy experimentally compared to the η/π^0 ratio. Since Fluid*u*M is a fluid-dynamic simulation, it is only valid for low transverse momenta. A saving grace is that the η/π^0 ratio is experimentally found to be constant for $p_{\mathrm{T}} > 5\,\mathrm{GeV}$, independent of collision energy and centrality [126]. To have a continuous description of the η/π^0 ratio for the whole p_{T}-range the following parametrization is used

$$\eta/\pi^0 = s(p_T)A\frac{\exp\left(\frac{p_T\beta-\gamma\sqrt{m_\eta^2+p_T^2}}{T}\right)}{\exp\left(\frac{p_T\beta-\gamma\sqrt{m_{\pi^0}^2+p_T^2}}{T}\right)} + (1-s(p_T))r, \tag{5.2}$$

with

$$s(p_T) = 1 - \frac{1}{2}\left(1+\mathrm{erf}\left(\frac{p_T-p_0}{d}\right)\right), \tag{5.3}$$

to ensure a smooth transition between the two regimes. The parameters of the model are determined by fitting to the Fluid*u*M results. The resulting curve together with the experimental data and the predictions from the other models can be seen in fig. 28. The parametrization is in agreement with the experimental measurement for the η/π^0 ratio. Contrary, the η/π^0 ratio obtained from m_{T}-scaling and from pp collisions do not capture the η/π^0 ratio measured in Pb-Pb collisions in the low momentum regime. The method proposed by Dress and Ren also is in good agreement with the experimental measurement and approaches the same limit for $p_{\mathrm{T}} \to 0$ as the data-driven Fluid*u*M prediction. However, the data-driven Fluid*u*M model only relies on the results of one experimental measurement for the low momentum prediction. The concrete values for the best fit parameters for eq. 5.2 and eq. 5.3 can be found in [51].

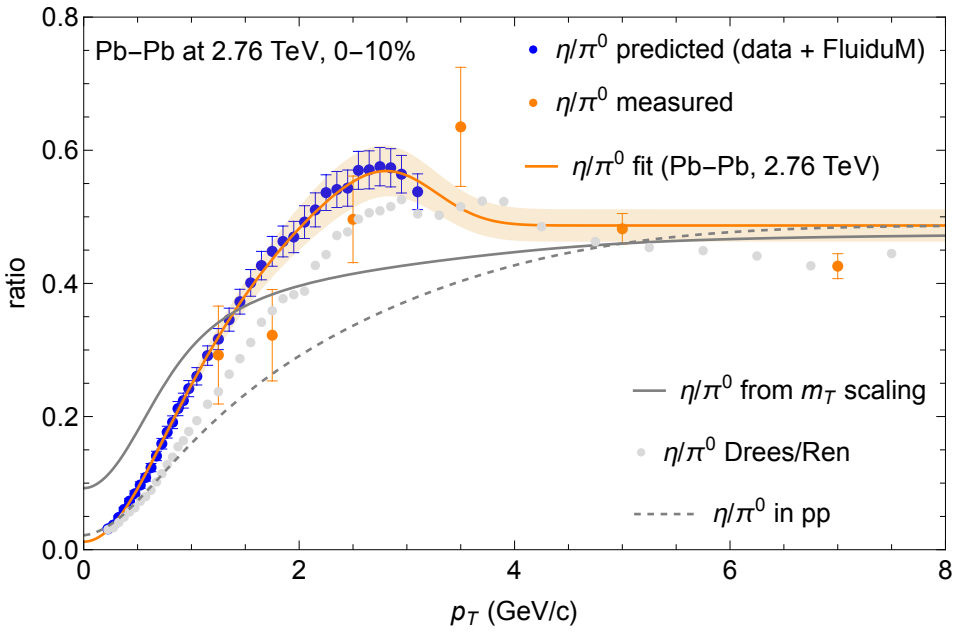

Figure 28: η/π^0 ratio from the various models together with the experimentally measured data. The parametrization is in agreement with the experimental measurement for the η/π^0 ratio. Contrary, the η/π^0 ratio obtained from m_{T}-scaling and from pp collisions do not capture the η/π^0 ratio measured in Pb-Pb collisions in the low momentum regime. The method proposed by Dress and Ren also is in good agreement with the experimental measurement and approaches the same limit for $p_{\mathrm{T}} \to 0$ as the data-driven Fluid*u*M prediction. However, the data-driven Fluid*u*M model only relies on the results of one experimental measurement for the low momentum prediction.

Evidently, the data-driven prediction for the η/π^0 ratio can be calculated with any event-by-event framework, as well. However, during the inception of this project the speed of Fluid*u*M was crucial in testing different ratios of particle spectra to find the optimal predictor. Additionally, the flexibility of Fluid*u*M was used to verify that the predicted η/π^0 ratio shows minimal model dependence by comparing the ratios for a large range of the model parameters. A similar approach was chosen for the next application, to study the connection of low energy nuclear structure and heavy-ion collisions.

5.4. Nuclear structure

One last application of Fluid*u*M I want to discuss in the scope of this thesis is a study carried out on the connection of nuclear structure and heavy-ion collisions. It became apparent that this connection is much stronger than previously thought before, after RHIC published its results taken from the isobaric collisions of ${}^{96}_{44}\mathrm{Ru}+{}^{96}_{44}\mathrm{Ru}$ and ${}^{96}_{40}\mathrm{Zr}+{}^{96}_{40}\mathrm{Zr}$, initially intended to study the chiral magnetic effect [127]. During the analysis of the data, a previously unexpected non-trivial multiplicity ratio of the two collision systems was found [128]. The absolute multiplicities together with their ratio as function of the centrality can be seen in fig. 29.

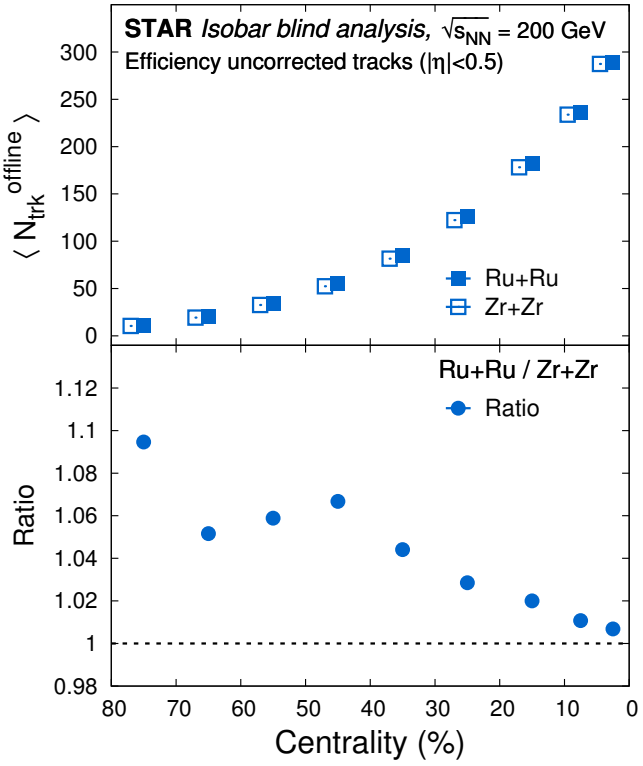

Figure 29: Measured absolute multiplicity and their ratios for the $^{96}_{44}$Ru+$^{96}_{44}$Ru and $^{96}_{40}$Zr+$^{96}_{40}$Zr collisions carried out at RHIC, taken from [127].

It has been shown in various initial state and transport calculations that this nontrivial multiplicity ratio can be attributed to the difference in the so-called neutron skin thickness of the two nuclei [129–133]. The density profile $\rho(r,\theta,\phi)$ of the incoming nuclei can be parametrized with a Wood-Saxon distribution (as is the case in T$_\mathrm{R}$ENTo)

$$\rho(r,\theta,\phi) \propto \frac{1}{1+\exp((r - R_0(1+\beta_2 Y_2^0(\theta,\phi)+\beta_3 Y_3^0(\theta,\phi)))/a_0)}, \tag{5.4}$$

where R_0 is the half-width radius of the nucleus, β_2 and β_3 are the nuclear deformation parameters and a_0 is the diffusivity, also known as neutron skin thickness. $Y_2^0(\theta,\phi)$ and $Y_3^0(\theta,\phi)$ are spherical harmonics depending on the polar angle θ and the azimuthal angle ϕ.

Fluid$u$M offers an ideal tool to study the impact of these different nuclear structure parameters, because the usually numerically very costly task of gathering statistics is being done on the level of the initial conditions. Creating a multitude of initial conditions and running the fluid dynamic simulation only for the event-averages is far less demanding than running the fluid simulation for every individual initial profile. This is especially true, when comparing to the isobar data collected at RHIC which amounts to approximately 3.8 billion isobar collisions of Ru and Zr.

The idea of this study is not a precise parameter extraction, as presented before, but much rather to determine the impact of the parameters of the nuclear density on the multiplicity ratio. Additionally, the impact of other T$_\mathrm{R}$ENTo parameters (p, k, w, m, v, d) and QGP parameters (τ_0, T_{fo}, η/s, ζ/s) was examined.

To gauge the impact of each of these parameters, I define a default parameter configuration and compare this baseline to a setting where only one parameter at a time has been changed. The default configurations for the T$_\mathrm{R}$ENTo parameters is $p = 0$, $w = 0.5$, $k = 1$, $d = 0$ without any sub-nucleon structure. For the nuclear parameters I will look at five different combinations: Three where the neutron skin of Ruthenium is smaller/the same/bigger than the neutron skin of Zirconium, one case where I set all nuclear deformations to zero to obtain round nuclei and one case where I increase/decrease the radius of Zirconium/Ruthenium. The nuclear parameters of the baseline parametrization for Ruthenium and Zirconium are displayed in tab. 4.

	R_0 [fm]	β_2	β_3	a_0 [fm]
Ru	5.09	0.16	0.0	0.473
Zr	5.016	0.0	0.16	0.527

Table 4: Nuclear structure parameters for the baseline parametrizations of Ruthenium and Zirconium.

In order to obtain a set of initial conditions for each parameter combination I use the T$_\mathrm{R}$ENTo entropy histogram from 50 million minimum bias events to define 200 centrality classes. Given the approximately linear relationship between the initial state entropy and the final state multiplicity, the ratio of these histograms can already give valuable insights into the importance of each parameter, except the QGP parameters, obviously. The results for the histogram ratios as function of the measured particles (specifically N_trck) are presented in fig. 30. The default parametrization $a_\mathrm{Zr} > a_\mathrm{Ru}$, as well as the case of round nuclei agree well with the experimental data, indicating that deformations seem to have little impact on the multiplicity ratio. A key observation here is that the ratio becomes flat or even inverts its shape as function of the measured tracks when the diffusivities are taken to be the same or are inverted.

The histogram ratios for the different collision parameters are shown in fig. 31. The different collision parameters do not significantly change the histogram ratios. Notable exceptions are the case of $w = 1.2\,\mathrm{fm}$ moving the ratio further to unity, as well as the cases $p = -1$ and $m = 4$, $v = 0.1\,\mathrm{fm}$ moving the ratio away from it. The decrease of the ratio can be attributed to the washing out of the difference in nuclear structure through the increased nucleon size. Similarly, the increase of the ratio stems from the spikier initial entropy profile created by $p = -1$ or having four very small partons, enhancing the differences in the nuclear structure of the two nuclei.

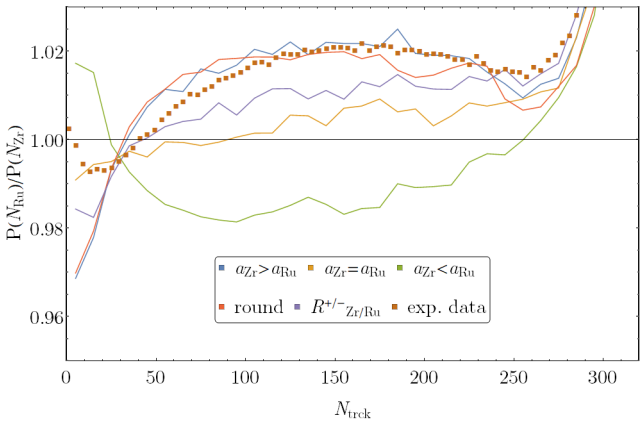

Figure 30: Histogram ratio of the five different sets of nuclear structure parameters together with the experimental data as function of N_{trck}.

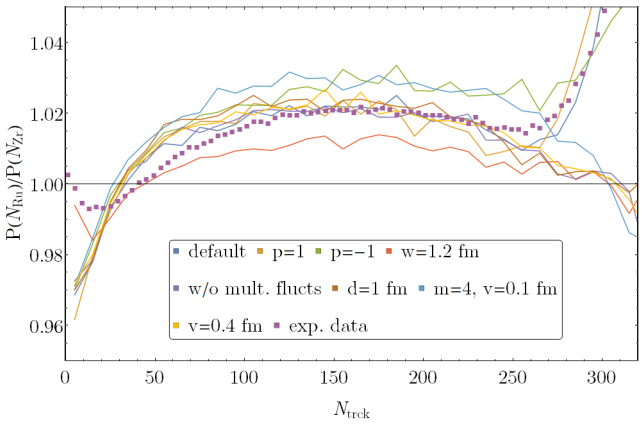

Figure 31: Histogram ratio of the different sets of collision parameters together with the experimental data as function of N_{trck}.

Since a comparison in every centrality bin is not needed, it is more efficient to only generate events in a few centrality classes. In these select bins (defined by the histogram from before), I generate 400.000 events, equaling the same statistics as a run with 80 million minimum bias events. In addition to the parameter combinations shown in fig.30 and fig.31, it is also interesting to study the effect of changing QGP parameters, such as the viscosities, on the multiplicity ratio. Note that in the following the experimental data are only plotted to guide the eye. Since the main objective of this study is to gauge the impact of the individual parameters on the histogram/multiplicity ratio, the final state results were produced without explicit fitting to the experimental data, explaining the off-set between theory and experiment in the following results. Firstly, the impact of the different QGP parameters is shown in fig. 32. Since the QGP produced in both collision systems is the same, the naive expectation that the ratio is insensitive to a change of QGP parameters gets confirmed. Since the initialization time τ_0 directly enters the normalization of the initial entropy profiles (in turn also affecting the final multiplicities), the ratios show a slightly stronger dependence on τ_0 than on the other parameters.

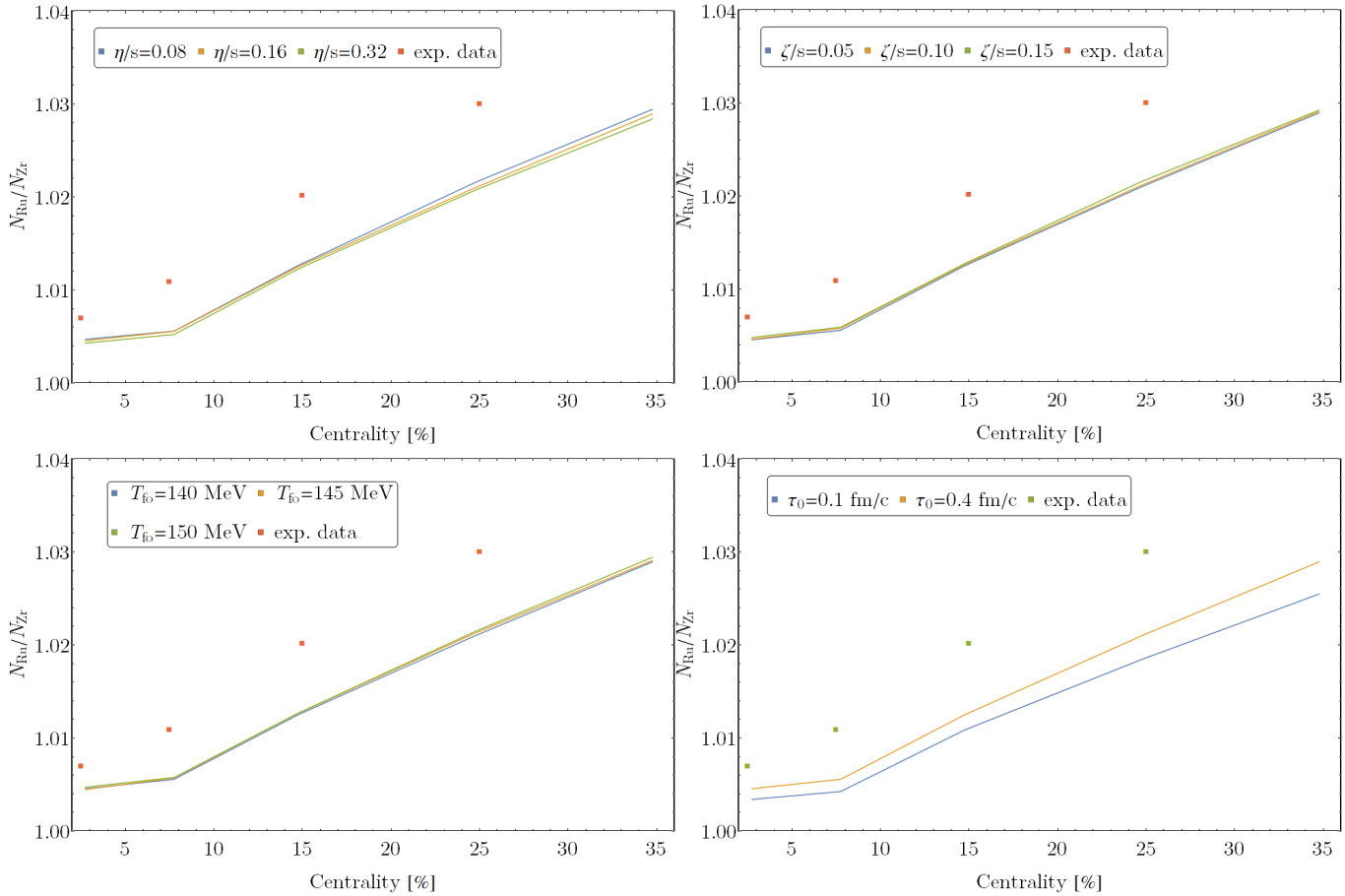

Figure 32: Multiplicity ratio for different QGP parameters as function of the centrality. Since the QGP produced in both collision systems is the same, the naive expectation that the ratio is insensitive to a change of QGP parameters gets confirmed. The theoretical results are not normalized to the experimental data.

Finally, the different nuclear and collision parametrizations can be examined again with the inclusion of the hydrodynamic phase (fig. 33). As was the case for the initial state results (fig. 30), the different nuclear parametrizations leave the multiplicity ratio unchanged, with the exception of the same or inverted diffusivity. In case for same diffusivity for Ruthenium and Zirconium, the multiplicity ratio is almost flat at unity, as was the case for the histogram ratios. The only possibility to obtain a histogram ratio smaller than one is again by inverting the ordering of the diffusivities.

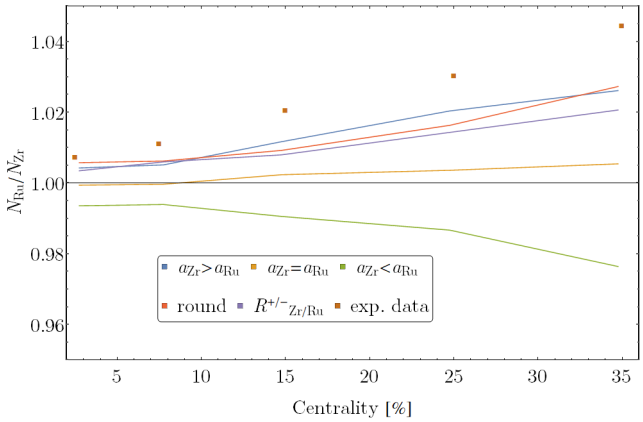

Figure 33: Multiplicity ratio of the different nuclear parametrizations.

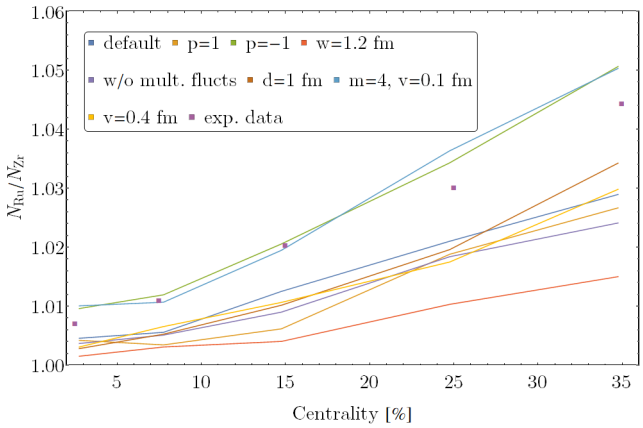

Figure 34: Multiplicity ratio of the different collision parametrizations.

The results for the multiplicity ratios of the different collision parametrizations are shown in fig. 34. Similar to the different nuclear parametrizations, the final state results show the same behavior as the initial state results, where the increase in nucleon width washes out the difference in nuclear structure and moves the ratio further to unity, whereas the sharper/spikier initial profiles for $p = -1$ and the four small partons moves it away from unity.

This confirms that the multiplicity ratio is mainly dominated by the difference in the neutron skin thickness of the two isobars. A more extensive study including more observables, such as the initial state energy (as predictor of the mean transverse momentum) and the initial state eccentricities (as predictors for the flow coefficients) has been carried out in the scope of the EMMI Rapid Reaction Taskforce “Nuclear physics confronts relativistic collisions of isobars” together with Federica Capellino. The results of this study are presented in the RRTF final report [53].

6. Extending the fluid description of heavy-ion collisions to times before the collision

6.1. Introduction

As second part of this thesis I examine a possible extension of the fluid-dynamic description of heavy-ion collisions. Concretely speaking, I extend the fluid description to times even before the collision, already describing the incoming nuclei by means of fluid dynamics. Traditionally, the fluid-dynamic description of a heavy-ion collision starts after approximately 1 fm/c after the initial collision of the two nuclei. At this stage the QGP has thermalized and is close enough to equilibrium to be described in terms of viscous fluid dynamics. With this approach the violent initial collision is not described by fluid dynamics. During the collision the system first is compressed heavily and then undergoes a fast expansion, resulting in it not being in thermal equilibrium. This far out of equilibrium system is not usually associated with fluid dynamics. However, by employing a relaxation-time-type fluid dynamics, such as proposed by Israel and Stewart, the out of equilibrium dynamics of the system can be accounted for with the viscous fields introduced in these frameworks.

In the following I develop this extension of the fluid dynamic description of heavy-ion collisions. The first step is to provide a set of equations of motion, together with an equation of state. Compared to the previous part of this thesis, baryon diffusion plays an important role in the dynamics examined here. Therefore, the equations of motion and the equation of state have to account for a non-zero chemical potential. As a next step I discuss the description of the incoming nuclei in terms of fluid dynamics. Finally, I examine the dynamics of the collision by considering two model systems. The first is an interactionless longitudinal setup in 1+1 dimensions. The second model mimics a heavy-ion collision as a universe filled with nuclear matter that contracts and expands homogeneously. It is used to study the entropy production during the collision and the trajectory of the system through the phase diagram.

6.2. Fluid-dynamic setting

In order to describe the full dynamics of the collisions by fluid dynamics, equations of motion describing the system are needed. The most obvious choice is the set of equations used in the previous chapters, based on the conservation of energy and momentum. As discussed in section 2, the relativistic Israel-Stewart equations together with the conservation of $T^{\mu\nu}$ and N^{μ} present a set of causal equations, allowing the fluid to be out of equilibrium. As before, an equation of state needs to be provided to obtain a closed system of equations. However, providing a suitable equation of state is a much bigger undertaking than before, since it needs to cover a much larger area of the QCD phase diagram.

The incoming nuclei, flying through the vacuum of the accelerator, sit at $T = 0\,\mathrm{MeV}$ and $\mu \approx 920\,\mathrm{MeV}$ in the phase diagram. During the collision the internal friction of the fluid transforms the chemical potential into heat, with a typical hotspot of an event at the LHC sitting around $T \approx 500\,\mathrm{MeV}$ and $\mu \approx 0\,\mathrm{MeV}$. As seen in the discussion of the Fluid$u$M framework, in the previous chapters, the endpoint of the QGP

fireball evolution lies on the freeze-out hypersurface which corresponds to $T \approx 150\,\mathrm{MeV}$ and $\mu \approx 0\,\mathrm{MeV}$ in the phase diagram. However, since QCD calculations, especially at finite temperature and finite baryon chemical potential, are topic of current research there is no single description covering the full needed range of the phase diagram. Therefore a combination of individual models, covering subareas of the phase diagram is employed. The individual models together with an indication of the area they are applied to are depicted in fig. 35. In the following I will briefly discuss the three models and how to combine them to obtain a continuous, differentiable function for $p(T,\mu)$, starting with lattice QCD.

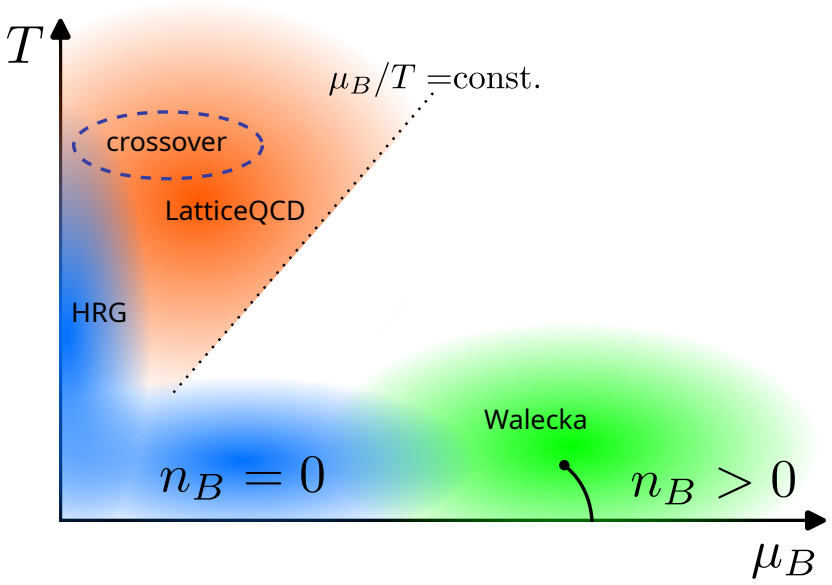

Figure 35: Sketch of the three models used for the equation of state. The region of the crossover between the QGP and hadrons, as well as the vacuum-nuclear matter phase transition are marked.

Lattice QCD For the case of high temperature and small chemical potentials the methods of lattice QCD [87, 88] can be used to calculate $p(T,\mu)$. The pressure and its derivative are calculated for discrete values of the temperature and chemical potential (the actual calculation uses a grid of temperature and μ/T for values with $\mu/T < 3$). A smooth function for the pressure can be obtained by using an interpolation of the data points. This interpolation is given by an equilibrium term at vanishing chemical potential together with an expansion up to sixth order in chemical potential

$$p(T,\mu) = p(T) + \sum_{i=2,4,6} \frac{\chi_i(T)}{i!}\mu^i. \tag{6.1}$$

Since the interpolations given in the literature are obtained using the Padé approximation, they become unphysical due to their pole at low temperatures. This pole can be removed by switching to the hadron resonance gas, describing QCD matter at low temperatures and densities.

Hadron resonance gas At low densities, i.e. low temperatures and chemical potentials, it has been shown that the strongly interacting QCD matter can be well described as a gas of non-interacting hadrons with their resonances [89]. At temperatures below approximately 150 MeV, the gas mainly consists out of pions, whose interactions are suppressed. Since heavy particles only appear in small densities $n_i \propto e^{-m_i/T}$, their mutual interactions (proportional to $n_i n_k \propto e^{-(m_i+m_k)/T}$) can also be neglected. The pressure therefore is given by the sum of the partial pressures of all hadrons and their resonances

$$P_{\mathrm{HRG}}(T,\mu) = \sum_{\text{baryons}} d_i P_{\mathrm{FG}}(T, B_i\mu; m_i) + \sum_{\text{mesons}} d_i P_{\mathrm{BG}}(T, 0; m_i) \,, \tag{6.2}$$

where d_i are the degeneracy factors related to spin, color charge etc. and the B_i the baryon charges. The partial pressures for fermions and bosons can be calculated with

$$P_{\mathrm{FG}}(T,\mu;m) = \frac{1}{2\pi^2}\left(\frac{m}{\beta}\right)^2 \sum_{k=1}^{\infty} \frac{(-1)^{(k+1)}}{k^2} K_2\left(k\beta m\right) e^{k\alpha} \,, \tag{6.3}$$

$$P_{\mathrm{BG}}(T;m) = \frac{1}{2\pi^2}\left(\frac{m}{\beta}\right)^2 \sum_{k=1}^{\infty} \frac{1}{k^2} K_2\left(k\beta m\right), \tag{6.4}$$

with K_2 being a modified Bessel function of the second kind. Since in the derivation of this expression, the virial expansion was used, it is only valid at low densities. Therefore an additional model describing the thermodynamics at low temperatures and high baryonic densities is needed. An additional requirement for this model is that it needs to be able to describe the first order phase transition from vacuum to nuclear matter. A suitable choice for such a model is the so called Walecka model.

Walecka model The Walecka model [134–138] is an effective model for the description of cold nuclear matter, interacting via the exchange of scalar and vector mesons. Generally speaking, these interactions can appear via the exchange of the scalar meson σ, the pseudo-scalar mesons π^0, $\pi^\pm$ and the singlet vector meson ω_μ between the baryonic matter fields ψ_a with the index a running over protons and neutrons. However, for the case of this work it is sufficient to work with isospin symmetric matter and neglect the interactions via the exchange of the pseudo-scalars. The effective Lagrangian describing this model is then given by

$$\mathcal{L} = \bar{\psi} i\gamma^\nu \left(\partial_\nu - ig\omega_\nu - i\mu\delta_{0\nu}\right)\psi + h\sigma\bar{\psi}\psi + \frac{1}{4}\sigma\left(-\partial_\mu\partial^\mu\right)\sigma + U_{\mathrm{mic}}(\sigma,\omega_0) + \frac{1}{4}F_{\mu\nu}F^{\mu\nu} + \frac{1}{2}m_\omega^2\omega_\mu\omega^\mu, \tag{6.5}$$

with the microscopic potential being parametrized as

$$U_{\mathrm{mic}} = \frac{1}{2}m_\pi^2(\sigma^2 - f_\pi^2) + \frac{1}{8}\lambda(\sigma^2 - f_\pi^2)^2 + \frac{1}{3}\frac{\gamma_3}{f_\pi^2}(\sigma^2 - f_\pi^2)^2 + \frac{1}{4}\frac{\gamma_4}{f_\pi^4}(\sigma^2 - f_\pi^2)^4 - m_\pi^2 f_\pi(\sigma - f_\pi) - \frac{1}{2}m_\omega^2\omega_0^2. \tag{6.6}$$

The parameters appearing in the potential are the couplings to nuclear matter g and h, the chemical potential μ, the masses of the sigma and omega mesons m_σ and m_ω together with the pion decay constant f_π and

three additional parameters λ, γ_3 and γ_4. To fix these parameters, experimental measurements as well as physical constraints will be used starting with the experimentally measured omega mass $m_\omega = 783\,\mathrm{MeV}$, pion mass $m_\pi = 135\,\mathrm{MeV}$ and pion decay constant $f_\pi = 93\,\mathrm{MeV}$. The coupling to the sigma meson can be fixed by the requirement $hf_\pi = m_N = 939\,\mathrm{MeV}$ with m_N being the nucleon mass, resulting in $h = 10$. The remaining parameters are fixed by constraints obtained from properties of the first order phase transition as well as properties of nuclear matter [137]. The values used in the following are given by $g = 9.5$, $\lambda = 50$, $\gamma_3 = 3$ and $\gamma_4 = 50$.

The assumptions used in the derivation of this model limits its range of applicability to a small area around to phase transition. Therefore, the running of the couplings can be neglected, allowing to simplify the subsequent calculations by employing a mean fields approximation. In this case the pressure of the Walecka model is given by the pressure of the fermionic matter modified by the presence of the sigma and omega mesons

$$P_{\mathrm{WM}} = 4P_{\mathrm{FG}}(T, \mu^*, m_N^*) - U_{\mathrm{mic}}(\bar{\sigma},\bar{\omega}_0) \tag{6.7}$$

where $\bar{\sigma}$ and $\bar{\omega}_0$ are the mean field values of the meson fields. At this point it is important to note, that the presence of the mesonic fields also introduces a shift in the chemical potential $\mu^* = \mu + g\bar{\omega}_0$ and the nucleon mass $m_N^* = h\bar{\sigma}$. The values of the mesonic fields have to be determined self consistently by the so-called gap equations

$$\partial_{\bar{\sigma}} P_{\mathrm{WM}}(T,\mu^*,m_N^*) = 0, \tag{6.8}$$

$$\partial_{\bar{\omega}_0} P_{\mathrm{WM}}(T,\mu^*,m_N^*) = 0, \tag{6.9}$$

which can be derived from thermodynamic stability conditions. The fermionic pressure contribution appearing in eq. 6.7 is given by

$$P_{FG}(T,\mu) = T\left(\frac{mT}{2\pi}\right)^{3/2} F_{3/2}\left(\frac{\mu - m}{T}\right), \tag{6.10}$$

where $F_{3/2}$ is the complete Fermi-Dirac integral. The complete Fermi-Dirac integral F_j is directly related to the polylogarithm $L_s(z)$ via

$$F_j(x) = -L_{j+1}(-e^x). \tag{6.11}$$

Since the system initially is at zero temperature, the low temperature limit of the Walecka model is needed during the initial stages of the collision. Formally the low temperature limit of the Fermi integration appearing when calculating the pressure is given by the Sommerfeld expansion [139]. The Sommerfeld expansion for the degenerate pressure is equivalent to the asymptotic expansion of the complete Fermi-

Dirac integral [140], given by

$$P_{FG}(T,\mu) = T\left(\frac{mT}{2\pi}\right)^{3/2} F_{3/2}\left(\frac{\mu-m}{T}\right) \tag{6.12}$$

$$= \sum_{n=0}^{\infty} 2^{-2n-\frac{1}{2}}(4^n-2)\frac{\zeta(2n)}{\pi^{3/2}\Gamma(\frac{7}{2}-2n)} m^{\frac{3}{2}}(\mu-m)^{\frac{5}{2}-2n}T^{2n} \tag{6.13}$$

$$= \frac{(2m)^{\frac{3}{2}}(\mu-m)^{\frac{5}{2}}}{15\pi^2} + \frac{m^{\frac{3}{2}}T^2\sqrt{\mu-m}}{6\sqrt{2}} - \frac{7m^{\frac{3}{2}}\pi^2T^4}{1440\sqrt{2}(\mu-m)^{\frac{3}{2}}} + \mathcal{O}(T^6). \tag{6.14}$$

The effective potential (i.e. the negative of the pressure) as function of the σ meson field for fixed chemical potentials at zero temperature is shown in fig. 36. For values of the chemical potential smaller than the critical chemical potential, the effective potential only has one minimum with $U_{\text{eff}} = 0$. This corresponds to the vacuum state, since $p = -U_{\text{eff}}$. For increasing chemical potential, a second minimum begins to form. For $\mu = \mu_{\text{crit}}$ the two global minima, corresponding to the coexistence of the matter and the vacuum phase, exist. For even larger values of the chemical potential, the second minimum becomes the global minimum with $U_{\text{eff}} < 0$, leading to a matter phase with non-vanishing pressure.

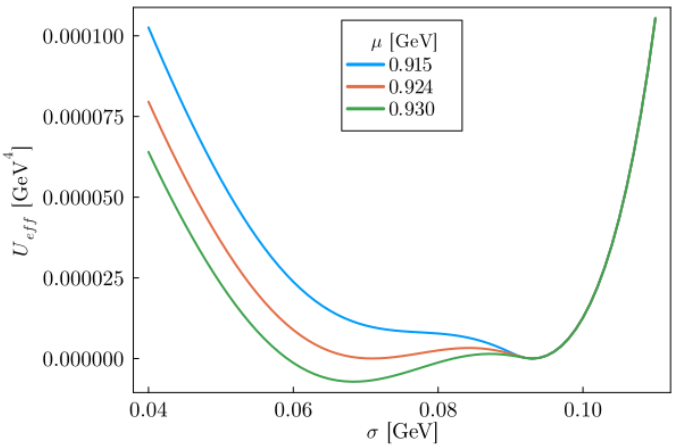

Figure 36: The effective potential as function of the σ meson field for fixed chemical potentials at zero temperature is shown in fig. 36. For values of the chemical potential smaller than the critical chemical potential, the effective potential only has one minimum with $U_{\text{eff}} = 0$. This corresponds to the vacuum state, since $p = -U_{\text{eff}}$. For increasing chemical potential, a second minimum begins to form. For $\mu = \mu_{\text{crit}}$ the two global minima, corresponding to the coexistence of the matter and the vacuum phase, exist. For even larger values of the chemical potential, the second minimum becomes the global minimum with $U_{\text{eff}} < 0$, leading to a matter phase with non-vanishing pressure.

Therefore, the pressure as function of the chemical potential starts out at zero with a continuous, but sudden increase at $\mu = \mu_{\text{crit}}$. The resulting jump in the number density can be seen in fig. 37. For vanishing temperature, the number density remains zero until the critical chemical potential is reach. At this point the number density jumps to the nuclear saturation density $n_0 = 0.153\,\text{fm}^3$. For temperatures larger than zero,

a small number density already builds up before the jump. For sufficiently large temperatures ($T \gtrapprox 20\,\mathrm{MeV}$) the endpoint of the phase transition line is crossed and the number density increases continuously without a jump.

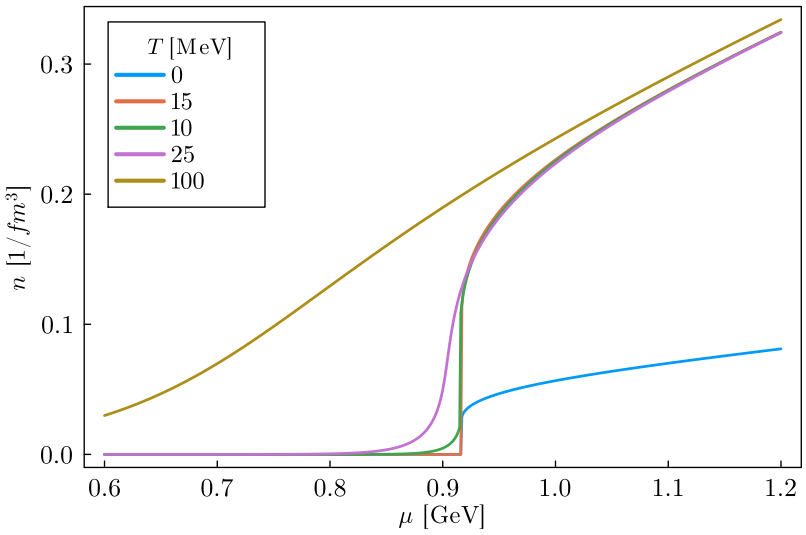

Figure 37: Number density of the Walecka model as function of the chemical potential. For temperatures below $T \lessapprox 20\,\mathrm{MeV}$ a jump in the number density can be found.

Due to the jump of the number density at the phase transition, the description of the system in terms of chemical potential and temperature is not sufficient any more (for a given pair of T and μ, that lie on the transition line any value of n within the jump is possible, which means $n(T,\mu)$ is not a function anymore). Vividly this can be understood by remembering that the fluid transitions between two phases, which are both present during the transition. When undergoing the phase transition, the temperature and chemical potential of the system do not change as long as the system transitions between the two phases. To describe the dynamics of this transition an additional parameter (e.g. the volume ratio of the two phases) is needed. During this phase coexistence the temperature, chemical potential and pressure have to be the same in both phases, as required by the thermodynamic stability conditions. For the scope of this work the microscopic details of the phase transition are not important, but one would expect the transition to take place via bubble nucleation or spinodal decomposition and related dynamics. A more suitable, macroscopic description of the dynamics of the phase transition can be obtained by considering the Massieu potential

$$w(\beta,\alpha) = \beta p, \tag{6.15}$$

with $\beta = 1/T$ and $\alpha = \mu/T$. The differential of the Massieu potential is given by $\mathrm{d}w = -\epsilon \mathrm{d}\beta + n\mathrm{d}\alpha$. This formalism has the advantage of being closely related to the dual affine geometry studied in information geometry. The coordinates $\gamma^m = (-\beta,\alpha)$ are easily related to the temperature T and chemical potential μ, which are usually taken to be the independent variables in the grand canonical ensembles. Combining

the conserved densities of the system into a vector $c_m = (\epsilon, n)$, allows to express the Massieu potential as $w = \gamma^m c_m + s(c)$, with $s(c)$ being the entropy. The differential can then be written as $\mathrm{d}w = c_m \mathrm{d}\gamma^m$. Returning to the dynamics of the phase transition, the Massieu potential can be written as linear combination of the two phases

$$w(\gamma) = [1 - r(\gamma)]w'(\gamma) + r(\gamma)w''(\gamma). \tag{6.16}$$

Here $w'(\gamma)$ is the Massieu potential in phase I and $w''(\gamma)$ is the Massieu potential in phase II. The parameter $r(\gamma)$ is zero in phase I and one in phase II and can be interpreted as fraction of the volumina of the two phases. During the transition the fraction $1 - r = V'/V$ is filled by a fluid in phase I and the fraction $r = V''/V$ is filled by phase II. Note that since the temperature, chemical potential and pressure agree in both phases during the transition, the Massieu potentials also agree $w'(\gamma) = w''(\gamma)$, while the derivatives can be different. The conserved charges also can be expressed as a linear superposition of the two phases

$$c_m(\gamma) = [1 - r(\gamma)]c'(\gamma) + r(\gamma)c''(\gamma). \tag{6.17}$$

The differential is then given by

$$\mathrm{d}c_m(\gamma) = \left[(1 - r)\, G'_{mn}(\gamma) + r\, G''_{mn}(\gamma)\right] d\gamma^n + [c''_m(\gamma) - c'_m(\gamma)]dr, \tag{6.18}$$

with the so-called thermal Fisher metric

$$G_{mn}(\gamma) = \frac{d^2 w(\gamma)}{d\gamma^m d\gamma^n} = V\left[\langle (c_m c_n + c_n c_m)/2\rangle - \langle c_m\rangle\langle c_n\rangle\right] = \frac{dc_n}{d\gamma_m}, \tag{6.19}$$

and its inverse

$$G^{mn}(c) = \frac{d\gamma^n(c)}{dc_m} = -\frac{d^2 s(c)}{dc_m dc_n}. \tag{6.20}$$

In order to obtain a closed system of equations again, one needs an equation of motion for the volume ratio r. Away from the phase transition, the equations of motion for the conserved charges can be written as

$$u^\mu \partial_\mu c_m + f_m = 0, \tag{6.21}$$

where f_m involves all fluid fields and their derivatives, which is equivalent to the description in terms of the thermodynamic variables γ^n given by

$$u^\mu \partial_\mu \gamma^n + G^{nm} f_m = 0. \tag{6.22}$$

In the presence of the phase transition, the differential $\mathrm{d}c_m$ changes, as seen in eq. 6.18, leading to a modified equation of motion for the coordinates γ^n

$$u^\mu \partial_\mu \gamma^n + G^{nm}(\gamma, r)\left[f_m + [c''_m(\gamma) - c'_m(\gamma)]u^\mu \partial_\mu r\right] = 0. \tag{6.23}$$

Here $G^{nm}(\gamma,r)$ is the inverse of the linear combination of the thermal Fisher metrices $[(1-r)\,G'_{mn}(\gamma) + r\,G''_{mn}(\gamma)]$, appearing in eq. 6.18. Note that away from the phase transition, eq. 6.22 is recovered.
During the phase transition, i.e. $0 \leq t \leq 1$, the coordinates γ^m are restricted to the hypersurface of the phase transition. Therefore, the differential of the coordinates during the phase transition must obey

$$\mathrm{d}\gamma^m n_m(\gamma) = 0. \tag{6.24}$$

Here $n_m(\gamma)$ is the normal vector of the phase transition hypersurface. Using this restriction, the evolution equation for the mixing parameter r can be derived as

$$u^\mu \partial_\mu r = -\frac{n_p(\gamma) G^{pq}(\gamma,r) f_q}{n_v(\gamma) G^{vs}(\gamma,r)[c''_s(\gamma) - c'_s(\gamma)]}. \tag{6.25}$$

The derivative of the mixing parameter is inverse proportional to the difference of the conserved charges, resulting in a faster phase transition when the two phases are similar to each other, i.e. the difference of their conserved charges is small. Substituting this evolution equation into the modified equation for the coordinates eq. 6.23, yields

$$u^\mu \partial_\mu \gamma^n + G^{nm}(\gamma,r)\left[f_m - [c''_m(\gamma) - c'_m(\gamma)]\frac{n_p(\gamma) G^{pq}(\gamma,r) f_q}{n_v(\gamma) G^{vs}(\gamma,r)[c''_s(\gamma) - c'_s(\gamma)]}\right] = 0. \tag{6.26}$$

This closes the system of equations also during the phase transition. Note that the precise normalization of the normal vector $n_m(\gamma)$ is not important. In practice, the phase transition can e.g. be found by checking for a jump either in the number density or the fields. For a numerical implementation it is particularly convenient to have a continuous parametrization. For the Walecka model described above, the phase transition can be parametrized as

$$\mu(T) = 0.924\,\mathrm{GeV} - 42.123\,\mathrm{GeV}^{-1}T^2 - 53\,938.76\,\mathrm{GeV}^{-3}T^4, \tag{6.27}$$

for $0 \leq T \leq 21\,\mathrm{MeV}$. The parametrization was obtained by fitting the polynomial function $\mu(T)$ to the values of the chemical potential at which the $\bar{\sigma}$ jumps for a given temperature. A comparison of the phase transition line obtained from finding the jump in the $\bar{\sigma}$ field with the parametrization can be seen in fig. 38.

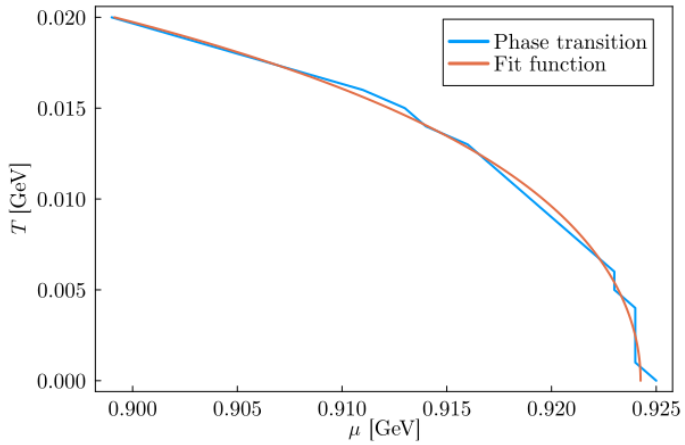

Figure 38: Comparison of the phase transition line obtained from the jump of the $\bar{\sigma}$ field with the parametrization. The values of the blue curve are calculated by finding the jump of $\bar{\sigma}$ for a given temperature. The polynomial fit to these values is shown as the red curve.

The normal vector is then given by

$$n_m(\gamma) = \left(-1, -2T(42.123\,\mathrm{GeV}^{-1} + 2 * 53\,938.76\,\mathrm{GeV}^{-3}T^2)\right). \tag{6.28}$$

Composite equation of state So far I have covered different models of the equation of state, which are applicable in different regions of the QCD phase diagram. However, especially for the numerical implementation it is crucial to have one smooth, differentiable equation of state covering all needed regions of the phase diagram. In the past some efforts have been made in obtaining such an equation of state [141, 142]. These approaches usually only provide a composite equation of state valid up to $\mu/T \lessapprox 3$. For the description of the incoming nuclei a wider range of coverage is needed. Since it is very hard to find an analytic parametrization for the pressure capturing the functional form at small and big μ/T simultaneously, the interpolation will be done by a neural network.

The architecture of the neural network was chosen as network with two inputs, one output and two hidden layers with 15 nodes each in between. The two input values of the network are the temperature and chemical potential. The output of the network is the pressure $p(T,\mu)$. The network was trained in two steps. As first step the model was trained by minimizing the difference between the network and the pressure data. This data was generated using the models presented above in their respective ranges of applicability. A comparison of the pressure calculated using the HRG and using LQCD can be seen in fig. 39. As a second step the network was trained including the first and second derivatives of the pressure in the loss. A comparison between the pressure from the neural network and the pressures obtained from the HRG and LQCD can be seen in fig. 40.

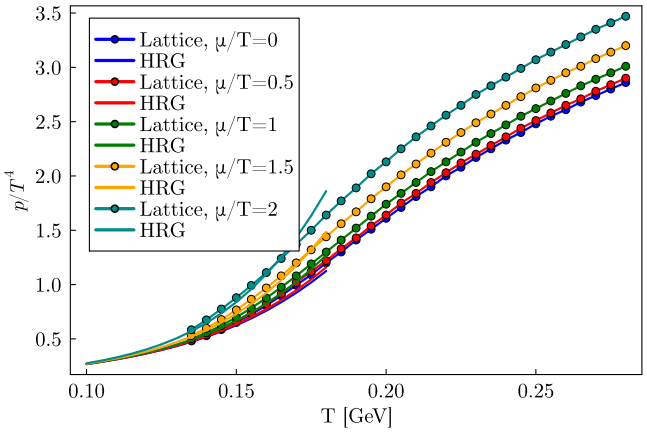

Figure 39: Comparison of the pressure obtained from lattice QCD calculations (lines with dots) and from the hadron resonance gas (lines without dots). The pressure is plotted as function of the temperature for fixed μ/T. The two models agree well around the crossover, i.e. around $T \approx 150\,\mathrm{MeV}$.

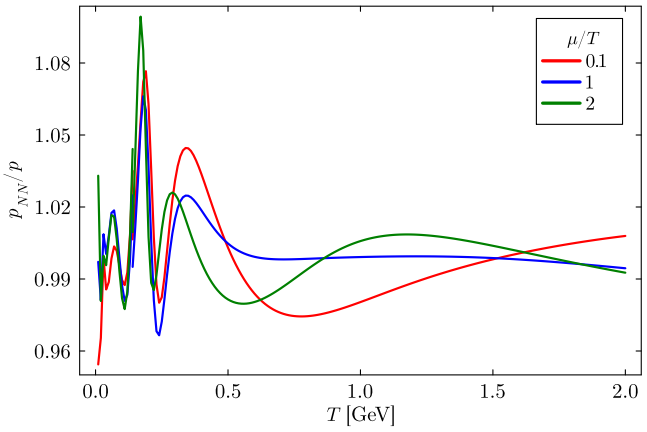

Figure 40: Comparison of the pressure obtained from the neural network fit (p_{NN}) with the pressures obtained from the hadron resonance gas and lattice QCD. The ratio is plotted as function of the temperature for different fixed μ/T.

6.3. Longitudinal setup

With the equation of state discussed at length, the missing ingredients for a full description of the system are equations of motion and initial conditions. First, I want to briefly discuss the equations of motion and the symmetries of the system

6.3.1. Longitudinal collision

The early times after the collision are dominated by longitudinal dynamics. Therefore, I want to focus on a system of two colliding nuclei restricted to dynamics only in the $t-$ and z-direction. This is equivalent to a collision of two nuclei with infinite extension in the x-y-plane. For this system a description in terms of cartesian coordinates (t,x,y,z) is well suited. Since the dynamics is restricted to the longitudinal direction the number of independent fields decreases:
The fluid velocity can only have a non-zero t- and z-component. Using the normalization $u_\mu u^\mu = -1$ the fluid velocity can be parametrized as

$$u_\mu = \left(\sqrt{1+u^2},0,0,u\right). \tag{6.29}$$

Similarly, the diffusion current only can have non-zero t- and z-components, which are parametrized as

$$\nu_\mu = \left(\frac{u\nu}{\sqrt{1+u^2}},0,0,\nu\right), \tag{6.30}$$

where the orthogonality of the diffusion current and the fluid velocity has been taken into account. Employing the restrictions arising from the orthogonality to the fluid velocity, tracelessness and the limitation to longitudinal dynamics the shear stress tensor is written as

$$\pi^{\mu\nu} = \pi^{zz} \begin{pmatrix} \frac{u^2}{1+u^2} & 0 & 0 & \frac{u}{\sqrt{1+u^2}} \\ 0 & -\frac{1}{2}\frac{1}{1+u^2} & 0 & 0 \\ 0 & 0 & -\frac{1}{2}\frac{1}{1+u^2} & 0 \\ \frac{u}{\sqrt{1+u^2}} & 0 & 0 & 1 \end{pmatrix}. \tag{6.31}$$

The remaining fields are the temperature, chemical potential and bulk pressure. The equations of motion for these fields will be derived from the conservation of energy and momentum as described in section 2. Since I will consider a spatially homogeneous system, simplifications to the equations of motion arise, which are discussed later. Next I will demonstrate how to describe the incoming nuclei as drops of liquid matter.

6.4. Preparation of the incoming nuclei

Evidently, for a collision of two nuclei, two nuclei flying towards each other are needed. To set up this system I first consider only one nucleus and how to describe it by the means of fluid dynamics.

6.4.1. Modeling of a single nucleus

The idea to describe nuclear matter as a fluid, is in fact not new. It was first proposed by Bethe, Weizäcker and Gamow in the so called liquid drop model [143, 144]. The liquid drop model gives a way of calculating the mass of an atomic nucleus from its proton and neutron number. The original equation from Weizäcker has five contributions to the mass of the nucleus: a volume and surface energy term (accounting for the interaction energy of the nucleons with each other inside the volume of the nucleus and on its surface), a coulomb term (accounting for the repelling force between the protons), an asymmetry term (accounting for the Pauli exclusion principle) and a pairing term (accounting for the tendency of proton and neutron pairs to occur). This model was derived by treating each nucleus as drop of an incompressible fluid with a very high density and provides a good description of the masses of different nuclei.
Since the collision takes place in vacuum, the nucleus sits at $T = 0$ and the critical chemical potential $\mu_{\text{crit}} \approx 920\,\text{MeV}$. Obviously this point lies on the phase transition line of the first order phase transition of the Walecka model. Therefore, the density profile of the nucleus has to be modeled by the volume ratio parameter r. The number density profile is modeled by the Wood-Saxon profile

$$n(z) = \frac{n_0}{1 + e^{(z-R)/a}}, \tag{6.32}$$

where R is the radius of the nucleus, a is the neutron skin thickness and n_0 is a normalization constant. Note that, since the nucleus is sitting on the phase transition, the thermodynamic pressure of the fluid is zero, resulting in a stable nucleus. For a nucleus at rest the fluid velocity is given by $u^\mu = (1,0,0,0)$. Using

this, the number density current and energy-momentum tensor of the nucleus at rest can be written as

$$N^\mu = n(0, \mu_{\text{crit}})u^\mu, \qquad T^{\mu\nu} = \epsilon(0, \mu_{\text{crit}})u^\mu u^\nu. \tag{6.33}$$

To obtain a nucleus flying through space with velocity v the system can be boosted accordingly. The resulting equations of motion are the ones of a free streaming, interactionless system

$$u^\mu \partial_\mu n = 0, \qquad u^\mu \partial_\mu \epsilon = 0. \tag{6.34}$$

With the description of one free streaming nucleus at hand, an initial setting for the full collision system can be developed.

6.4.2. Modeling of two colliding nuclei

Evidently, one single nucleus is not enough for a collision. To obtain an energy-momentum tensor and a number density current describing the full collision system the energy-momentum tensors and number density currents boosted with $\pm v$ are added. In the following I denote quantities related to the right/left moving nucleus with index $\rightarrow$ / $\leftarrow$. With this notation, the energy-momentum tensor and number density current of the full system are given by

$$N^\mu_{\text{sum}} = N^\mu_{\rightarrow} + N^\mu_{\leftarrow} \quad \text{and} \quad T^{\mu\nu}_{\text{sum}} = T^{\mu\nu}_{\rightarrow} + T^{\mu\nu}_{\leftarrow}. \tag{6.35}$$

The fluid fields describing the full collision system can be recovered using the tensor decomposition introduced in eq. 2.41 and eq. 2.42, also known as Landau matching. The decomposition reads as

$$N^\mu_{\text{sum}} = n_{\text{sum}} u^\mu_{\text{sum}} + \nu^\mu_{\text{sum}}, \tag{6.36}$$

$$T^{\mu\nu}_{\text{sum}} = \epsilon_{\text{sum}} u^\mu_{\text{sum}} u^\nu_{\text{sum}} + (p_{\text{sum}} + \Pi_{\text{sum}})\Delta^{\mu\nu}_{\text{sum}} + \pi^{\mu\nu}_{\text{sum}}. \tag{6.37}$$

Using the restriction to the longitudinal dynamics again, the number density current can be expressed as $N^\mu_{\text{sum}} = (\gamma_{\text{sum}} n_{\text{sum}} + \beta_{\text{sum}} \nu_{\text{sum}}, 0, 0, \gamma_{\text{sum}} \beta_{\text{sum}} n_{\text{sum}} + \nu_{\text{sum}})$. The number density and diffusion current in the collision system are then given by

$$n = \frac{1}{\gamma}\left[\gamma_{\rightarrow} n_{\rightarrow} + \gamma_{\leftarrow} n_{\leftarrow} - \beta\nu\right], \tag{6.38}$$

$$\nu = \gamma^2\left[\gamma_{\rightarrow} n_{\rightarrow}(\beta_{\rightarrow} - \beta) + \gamma_{\leftarrow} n_{\leftarrow}(\beta_{\leftarrow} - \beta)\right]. \tag{6.39}$$

Here and in the following I will suppress the sum index for reasons of readability. When using the Landau matching conditions, the fluid velocity and energy density of the system are given by the time-like eigenvector and corresponding eigenvalue of the energy-momentum tensor

$$T^\mu_\nu u^\nu = -\epsilon u^\mu, \tag{6.40}$$

where the eigenvector (i.e. the fluid velocity) gets normalized to $u_\mu u^\mu = -1$. The shear stress tensor and bulk pressure can be obtained by

$$\Pi = \frac{1}{3}\Delta^{\mu\nu}T_{\mu\nu} - p(T,\mu), \tag{6.41}$$

$$\pi^{\mu\nu} = T^{\mu\nu} - \epsilon u^\mu u^\nu - (p+\Pi)\Delta^{\mu\nu}. \tag{6.42}$$

Since the thermodynamic description of the system was chosen to be in terms of T and μ (or β and α), the equation of state has to be inverted to obtain the temperature and chemical potential (or equivalent variables) from the energy and number density recovered from the matching procedure. With the matching procedure at hand, a first crude approximation of the collision is possible.

6.4.3. Interactionless collision

Since the colliding nuclei almost move with the speed of light, the time available for interactions is very limited. Therefore, a first, very simple model of the collision is the interactionless limit given by the Landau matching procedure executed at different times. Considering a Pb-Pb collision at $\sqrt{s} = 2.76\,\text{TeV}$, corresponding to $\gamma \approx 2960$, and initializing the two nuclei at $z = \pm 0.025\,\text{fm}$ at $t = 0$, the number density of the collision system at different times can be seen in fig. 41.

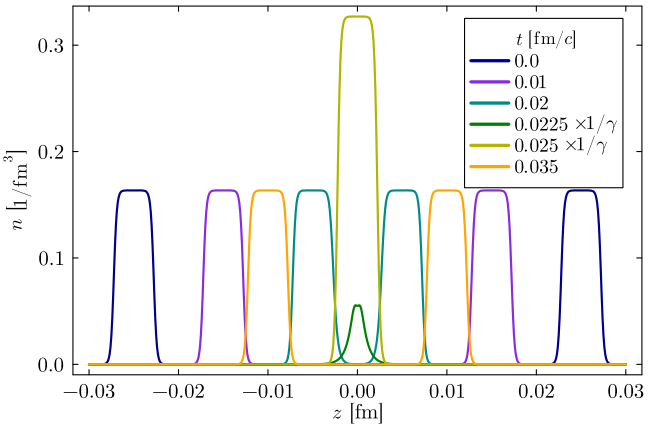

Figure 41: Number density obtained from Landau matching at different times. Note that the profiles at $t = 0.0225\,\text{fm/c}$ and $t = 0.025\,\text{fm/c}$ have been rescaled by γ for better visibility.

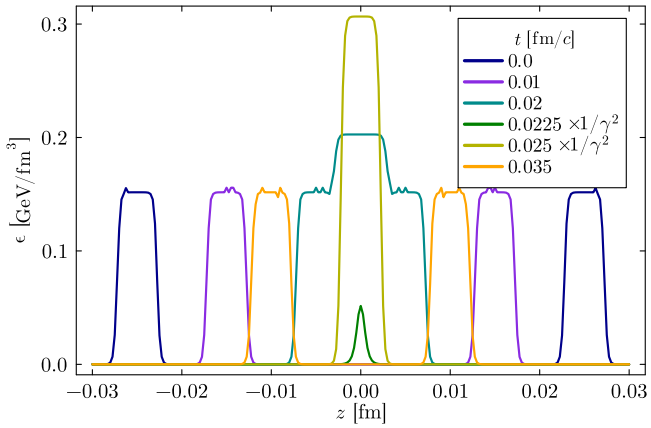

Figure 42: Energy density obtained from Landau matching at different times. Note that the profiles at $t = 0.0225\,\text{fm/c}$ and $t = 0.025\,\text{fm/c}$ have been rescaled by γ^2 for better visibility.

Initially the two nuclei are separated far enough, such that they are basically separate nuclei that do not feel the presence of the other nucleus. However, if they move further together, the nuclei start to overlap which leads to an increase of the number density. When the two nuclei are at the same point, the effective number density is much higher than twice the initial number density due to the Lorentz contraction of the nuclei.

Curiously, a similar but distinct behavior can be found in the energy density, as seen in fig. 42. In contrast to the number density at $t = 0.02\,\mathrm{fm}$, the energy density already shows signs of "interaction" at this point in time. A further difference between the two quantities is the respective peak value compared to its starting value. This larger increase in the energy density stemming from the additional γ factor in the energy-momentum tensor can also be seen in fig. 43 as function of the time. The ratio has been taken between the energy density and the number density in the center of one of the nuclei (i.e. in the co-moving frame at $z = z_0 + vt$). Initially the ratio between the energy density and the number density is around $\epsilon/n \approx 920\,\mathrm{MeV}$, recovering the vacuum relation $\epsilon = \mu_{\mathrm{crit}} n$. At its peak value the ratio is approximately amplified by γ corresponding to $\epsilon/n \approx 2700\,\mathrm{GeV}$.

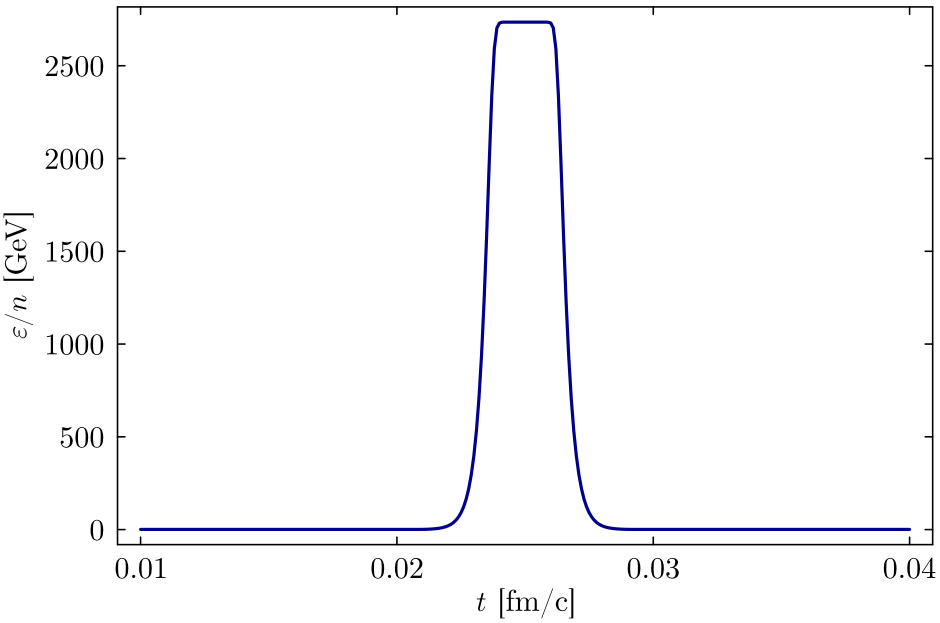

Figure 43: Ratio of the energy density and the number density in the center of a nucleus (i.e. in the co-moving frame at $z = z_0 + vt$) at different times. Initially the ratio between the energy density and the number density is around $\epsilon/n \approx 920\,\mathrm{MeV}$, recovering the vacuum relation $\epsilon = \mu_{\mathrm{crit}} n$. At its peak value the ratio recovers the value of the γ-factor of around $\epsilon/n \approx 2700\,\mathrm{GeV}$.

Since the initial, individual density profiles get boosted by the same velocity everywhere, the individual velocity profiles are simply constants at $\pm v$. When adding the two nuclei, the resulting velocity profile after the matching procedure is then simply a step function, as can be seen in fig. 44. At full overlap ($t = 0.025\,\mathrm{fm/c}$) the velocity is zero everywhere and flips sign for times $t > 0.025\,\mathrm{fm/c}$.

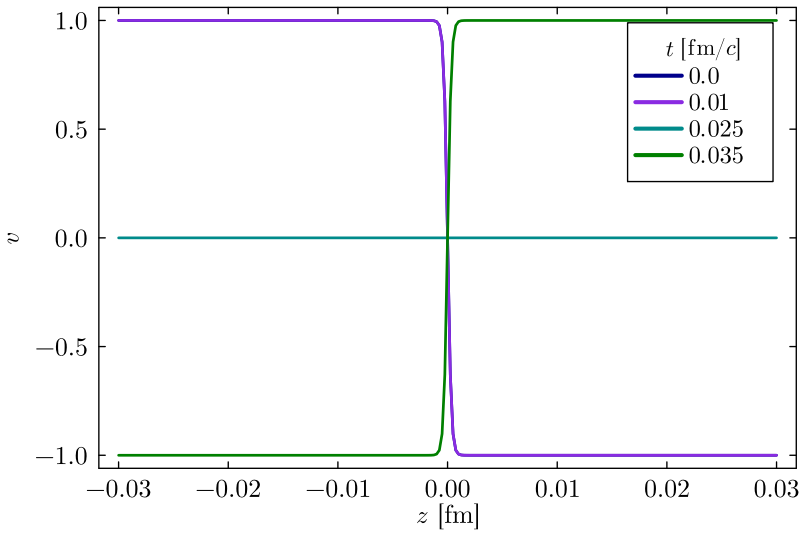

Figure 44: Velocity profile obtained from the Landau matching procedure. Since the initial, individual density profiles get boosted by the same velocity everywhere, the individual velocity profiles are simply constants at $\pm v$. When adding the two nuclei, the resulting velocity profile after the matching procedure is then simply a step function. At full overlap ($t = 0.025\,\mathrm{fm/c}$) the velocity is zero everywhere and flips sign for times $t > 0.025\,\mathrm{fm/c}$.

Finally, the equation of state can be used as described before to obtain the temperature and chemical potential. With this, the trajectory of the system through the phase diagram can be tracked. Obviously the concrete trajectory depends on the equation of state used. A comparison for the different trajectories obtained from the hadron resonance gas, lattice QCD and the composite equation of state can be seen in fig. 45. Even in the collisionless limit, the system follows the expected trajectory, starting at high chemical potential and low temperature and going to high temperature and low chemical potential. However, since no interactions take place, the system ends up being in the same point of the phase diagram as it was at the beginning. There is a striking difference between the different equations of state which can be linked to their expansion in the chemical potential. The ideal QCD equation of state is the one for a gas of free quarks and gluons with terms proportional to μ^0, μ^2 and μ^4. Similarly the lattice QCD equation of state is based on an expansion in chemical potential, which includes terms up to μ^6. Since the chemical potential enters the pressure of the hadron resonance gas as part of an exponential, the hadron resonance gas pressure can be seen as an infinite series in μ. To be able to reach the very high number densities during the collision, the equations of state with fewer powers of the chemical potential need to remain at higher values of the chemical potential, explaining the ordering of the three different models. Evidently all of this has to be taken with a grain of salt, since an interactionless collision is not very realistic and the individual equations of state are on their own not the correct description through the full trajectory of the system.

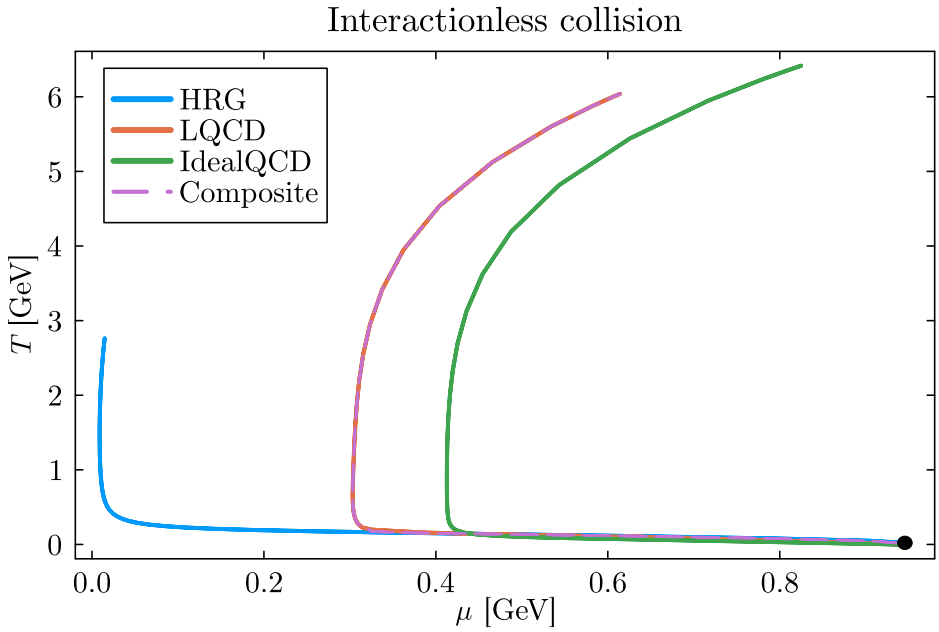

Figure 45: Trajectories of the system through the phase diagram for the collisionless system. The trajectories are obtained by using the equation of state to calculate T and μ from the energy density and number density from the Landau matching. Even in the collisionless limit, the system follows the expected trajectory, starting at high chemical potential and low temperature and going to high temperature and low chemical potential. However, since no interactions take place, the system ends up being in the same point of the phase diagram as it was at the beginning. This initial/final point is marked.

To obtain a more realistic setting, I now return to a system with interactions, governed by the equations of fluid dynamics. However, directly examining the full longitudinal dynamics is rather complicated due to the complex interplay of the three different viscous corrections appearing. Additionally, the large velocity of the incoming nuclei can pose challenges to the numerical implementation of the equations. Therefore, I will first examine a simpler system, where by reasons of symmetry only one dissipative correction appears.

6.5. Hubble universe

A very simple model of the collision part of a heavy-ion collision is that nuclear matter gets contracted during the collision and expands afterwards. A convenient way of modeling this is to consider a homogeneous, isotropic universe filled with nuclear matter, that can contract and expand. The contraction/expansion of the universe can be modeled with a time dependent scale factor $a(t)$ in the line element [11]

$$\mathrm{d}s^2 = -\mathrm{d}t^2 + a(t)^2(\mathrm{d}x^2 + \mathrm{d}y^2 + \mathrm{d}z^2). \tag{6.43}$$

[11] Note that the the expanding universe is conceptually different to a sphere of nuclear matter expanding and contracting in a flat space-time, since a mapping between the two only exists for $a(t) = const.$

Since this system is translation and rotational invariant, all the fluid fields can only depend on time $\Phi(t,x,y,z) = \Phi(t)$. Due to the invariance under spatial rotation all vectors, like the fluid velocity or diffusion current, can only have a non-zero time component, i.e. $u^\mu = (1,0,0,0)$. Since the diffusion current is orthogonal to the fluid velocity, it has to be zero to not violate the rotation symmetry. For similar reasons, the shear stress tensor has to vanish as well. This leaves three non-vanishing (and non-trivial) fluid fields, namely the temperature, chemical potential and the bulk pressure $\Phi = (T,\mu,\Pi)$. The equations of motion for these quantities are obtained via energy-momentum and particle number current conservation, together with the Israel-Stewart type equation for the bulk pressure. An insightful in-between step is to formulate the equations first in terms of the conserved charges ϵ and n, yielding

$$\partial_t \epsilon + 3H(\epsilon + p + \Pi) = 0 \tag{6.44}$$

$$\partial_t n + 3Hn = 0 \tag{6.45}$$

$$\tau_B \partial_t \Pi + \left(1 + +3H\frac{\tau_B}{2} - \frac{\tau_B}{2}\frac{\partial_t T}{T}\right)\Pi + 3H\zeta = 0, \tag{6.46}$$

where the Hubble rate $H = \dot{a}(t)/a(t)$ was introduced. The equation for the number density is actually simple enough to be solved analytically with $n(t) = n_0 e^{-3\int H(t)\mathrm{d}t}$. However, since the equation of state is formulated as $p(T,\mu)$ or $p(\beta,\alpha)$ and not as $p(\epsilon,n)$, it is more convenient to use the formalism developed above to obtain equations for the temperature and chemical potential by means of the thermal Fisher metric. The equation for the bulk pressure has been derived as described by demanding a positive entropy production at all times, see section 2. The entropy production reads as

$$\nabla_\mu S^\mu = -\frac{\Pi}{T}(3H + 3\beta_0\Pi(t)H - \beta_0\frac{\partial_t T}{T}\Pi + 2\beta_0\partial_t\Pi + \Pi\partial_\mu\beta_0\partial_t\mu + \Pi\partial_T\beta_0\partial_t T), \tag{6.47}$$

with β_0 being proportional to the bulk relaxation time (see eq. 6.51).
The conservation equation for the number density can actually be used to obtain the Hubble rate by writing

$$H = -\frac{\partial_t n}{3n}, \tag{6.48}$$

and using the number density from the interactionless collision, fig. 41. The resulting Hubble rate can be seen in fig. 46. Due to the limited interaction time of the two nuclei the Hubble rate obtained from the interactionless limit is a reasonable approximation for the real collision.

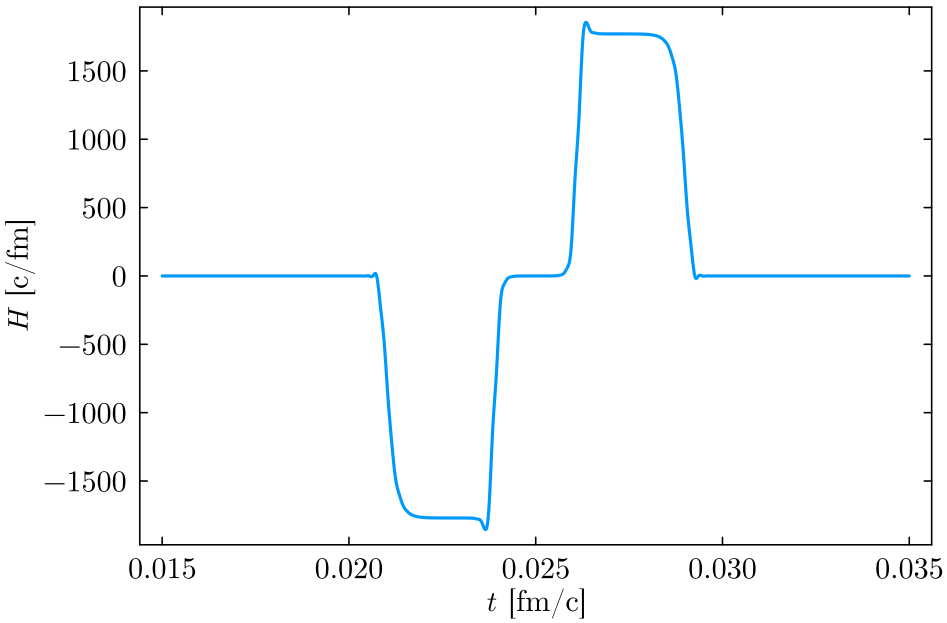

Figure 46: Hubble rate as function of time extracted from an interactionless collision according to eq. 6.48 at $\sqrt{s} = 2.76\,\text{TeV}$.

The final component needed for the implementation of the system of equations is a parametrization of the bulk viscosity as function of the temperature and the chemical potential. For this a parametrization based on the bulk viscosity given in eq. 3.32 is extended by the substitution $T \to \sqrt{T^2 + a^2\mu^2}$ with $a = 0.188$ chosen, such that the peak of the bulk viscosity lies at the phase transition for $T = 0$. The bulk viscosity and corresponding relaxation time read as

$$\zeta_P = \frac{1}{1 + \left(\frac{\sqrt{T^2+a^2\mu^2} - 24\,\text{MeV}}{175\,\text{MeV}}\right)^2}, \tag{6.49}$$

$$\frac{\zeta}{s}(T) = (\zeta/s)_{\max}\, \zeta_P, \tag{6.50}$$

$$\tau_B = 2\beta_0 \zeta_P, \tag{6.51}$$

where the coefficients $(\zeta/s)_{\max}$ and β_0 have been introduced to be able to vary the relaxation time and the viscosity independently from each other, while keeping the same dependence on temperature and chemical potential. The base parametrization of the bulk viscosity ζ_P can be seen in fig. 47. This system of equations has been implemented using the julia coding language. Since the fields only depend on time, the resulting set of ordinary differential equations can be solved using Rosenbrock methods [94, 145].

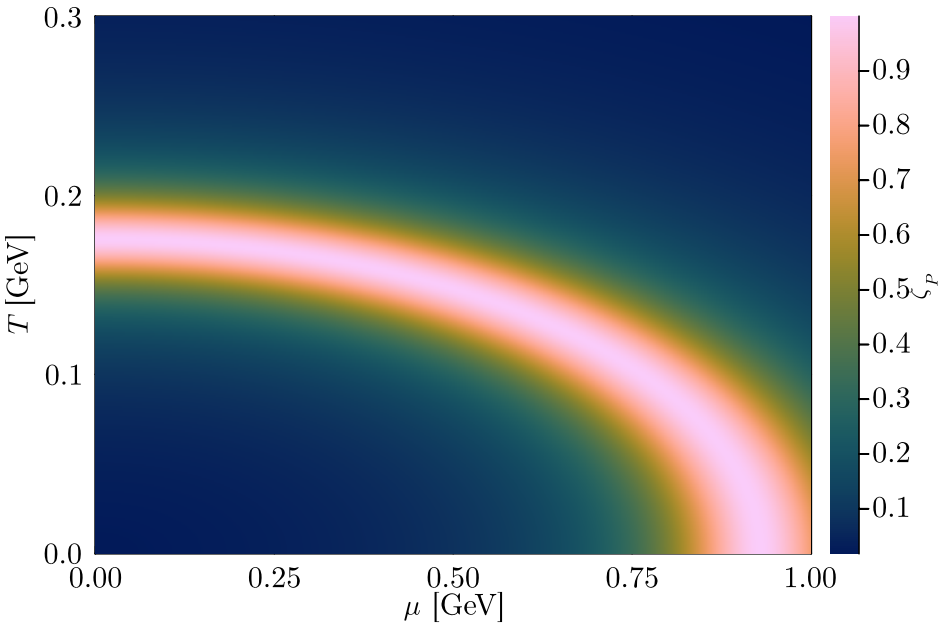

Figure 47: Base parametrization ζ_P of the bulk viscosity and relaxation time as function of temperature and chemical potential. The bulk viscosity and relaxation time are linked to this parametrization via the parameters $(\zeta/s)_{\max}$ and β_0.

6.5.1. Results

Using the Hubble rate for $\sqrt{s} = 2.76\,\text{TeV}$, the solutions to the ODE system are shown in fig. 48. Until $t \approx 0.02\,\text{fm/c}$, the Hubble rate is zero, which means the fields remain at the value they have been initialized with (all fields expect the chemical potential have been initialized as zero and $\mu(t = 0) = \mu_{\text{crit}}$). During the initial contraction phase (i.e. when $H < 0$) the system tries to resist the contraction, which leads to a large, positive bulk pressure. The internal friction of the medium converts the chemical potential into temperature by creating particles, entropy and heat. After the initial contraction phase the Hubble rate shortly remains almost zero, which is the moment when the system reaches its largest temperature. During the subsequent expansion, the system again tries to resist, resulting in the decrease of the bulk pressure. The expansion of the system also leads a decrease of the temperature coming from the decreasing density. However, since the system has a non-zero viscosity, entropy has been created, which means that the temperature cannot drop back to zero during the expansion phase. In the final stages of the collision where the Hubble rate approaches zero again, the bulk pressure also relaxes back to zero.

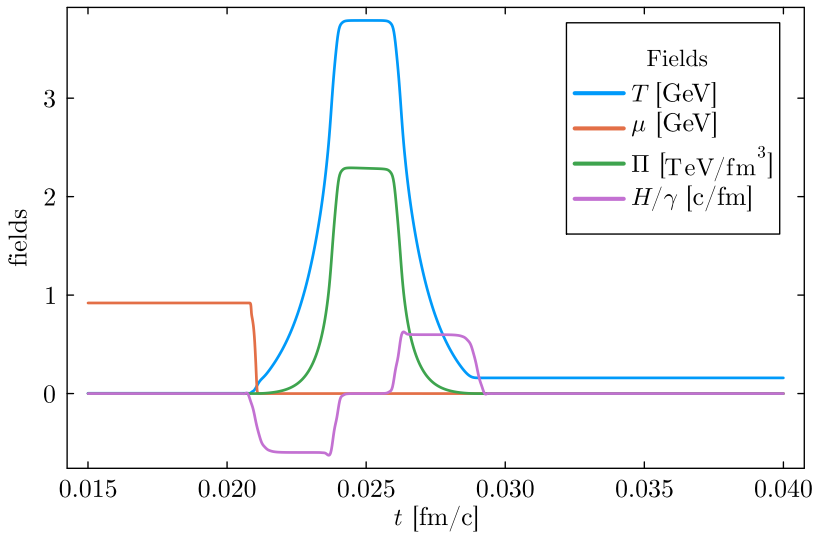

Figure 48: Evolution of the fluid fields of the Hubble universe. During the initial contraction phase the temperature and bulk pressure increase, while the chemical potential decreases. After the subsequent expansion phase the temperature and bulk pressure have decreased again. Since the system has non-zero viscosity, the final temperature is larger than its initial value.

The time evolution of the volume mixing parameter r is shown in fig. 49 for different initial volume ratios. As soon as the contraction starts, the system moves along the phase transition line, increasing the volume ratio parameter r. The fast contraction of the system leads to the universe transitioning quickly between the phases, until $r = 1$ is reached. Afterwards the volume ratio stays constant and the system stays in the corresponding phase, moving away from the phase transition. In the following I will focus on the dynamics of the other fluid fields, considering the evolution of r only taking place for a very short period.

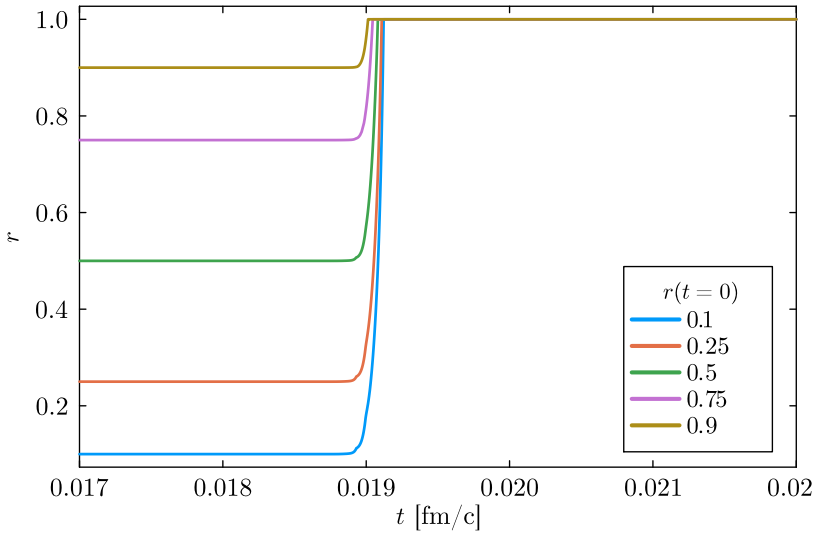

Figure 49: Evolution of the volume ratio parameter r for different initial values of r.

Plotting the trajectory of the system in the phase diagram results in fig. 50. Initially, the system sits at the phase transition of the Walecka model. During the initial contraction the system first stays at almost zero temperature while moving towards zero chemical potential. As soon as the baryon asymmetry has been balanced out by the viscosity, the system starts to produce heat and entropy resulting in a steep rise of the temperature. During the expansion phase the temperature and chemical potential both drop due to the matter being diluted. The final point of this trajectory lies at $\mu \approx 0$ and $T \approx 160\,\mathrm{MeV}$, which is close to the crossover between the QGP and the hadronic phase.

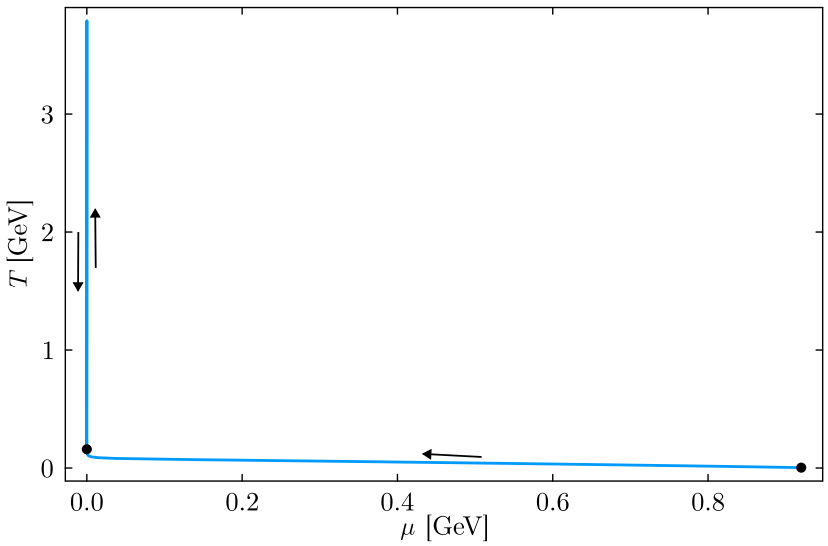

Figure 50: Trajectory of the collision system through the phase diagram for $\sqrt{s} = 2.76\,\mathrm{TeV}$. Initially, the system sits at the phase transition of the Walecka model. During the initial contraction the system first stays at almost zero temperature while moving towards zero chemical potential. As soon as the baryon asymmetry has been balanced out by the viscosity, the system starts to produce heat and entropy resulting in a steep rise of the temperature. During the expansion phase the temperature and chemical potential both drop due to the matter being diluted. The initial (right) and final (left) points of the evolution have been marked.

The entropy production of this event can be seen in fig. 51 together with the Hubble rate. As long as the Hubble rate is zero, no entropy is being produced. As soon as the contraction of the system starts, entropy is being produced. The entropy production hits its maximum at the turning point, when the system switches from contraction to expansion. During the expansion phase of the universe, the density drops, leading to a decrease of the entropy production. Finally, when the Hubble rate is zero again and the system is static again, no more entropy is being produced.

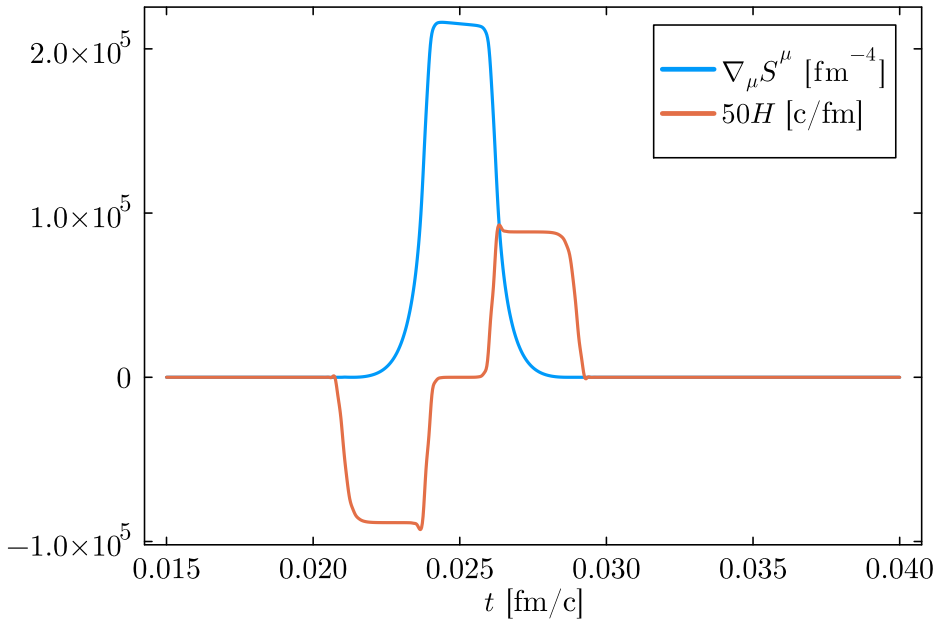

Figure 51: Entropy production together with the Hubble rate as function of the evolution time. As long as the Hubble rate is zero, no entropy is being produced. As soon as the contraction of the system starts, entropy is being produced. The entropy production hits its maximum at the turning point, when the system switches from contracting to expansion. During the expansion phase of the universe, the density drops, leading to a decrease of the entropy production. Finally, when the Hubble rate is zero again and the system is static again, no more entropy is being produced.

This model system allows to study the entropy production and the dynamics of the system as functions of parameters, that are hardly controllable in an experiment. The first parameter is the center of mass energy, or equivalently the γ-factor, which can to some extend be changed in experiment. The other two parameters are the magnitudes of the bulk viscosity $(\zeta/s)_{\max}$ and of the bulk relaxation time β_0. These two parameters are impossible to control experimentally, since they are material quantities. However, it is still very insightful to study the dynamics of the system as function of the bulk viscosity and its relaxation time. To begin I examine the entropy production for different γ-factors, shown in fig. 52. For collisions at lower energy, the expansion and contraction phases last longer, resulting in entropy being produced during a longer time span. However, a slower contraction results in less bulk pressure being build up, in turn resulting in a smaller maximum of the entropy production $\nabla_\mu S^\mu$.

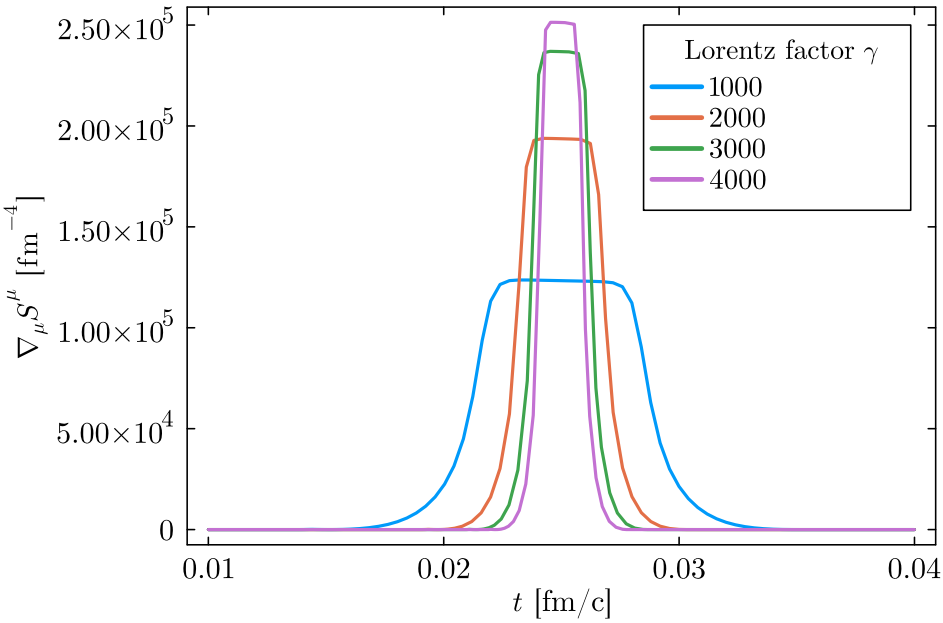

Figure 52: Entropy production as function of time for different γ-factors. The faster and more violent collisions at higher γ produce entropy during a shorter time span, but have a bigger maximal entropy production.

The maximal value of the entropy production as function of γ can be seen in fig. 53. The left panel additionally varies the bulk viscosity by changing $(\zeta/s)_{\max}$, while the right panel varies the bulk relaxation parameter β_0. The first thing to note is that the peak of the entropy production scales with the γ-factor and therefore as well with the collision energy. As expected, more entropy is being produced for a more viscous fluid. Turning to the case of different relaxation times, it shows that the peak value of the entropy production scales inverse to the bulk relaxation time. The reason for this inverse scaling becomes apparent when reconsidering eq. 6.46. A smaller bulk relaxation time allows for larger time derivative of the bulk pressure, in turn enabling a faster reaction of the system to its contraction. The larger time derivative of the bulk pressure leads to larger total bulk pressures and successively to a bigger entropy production.

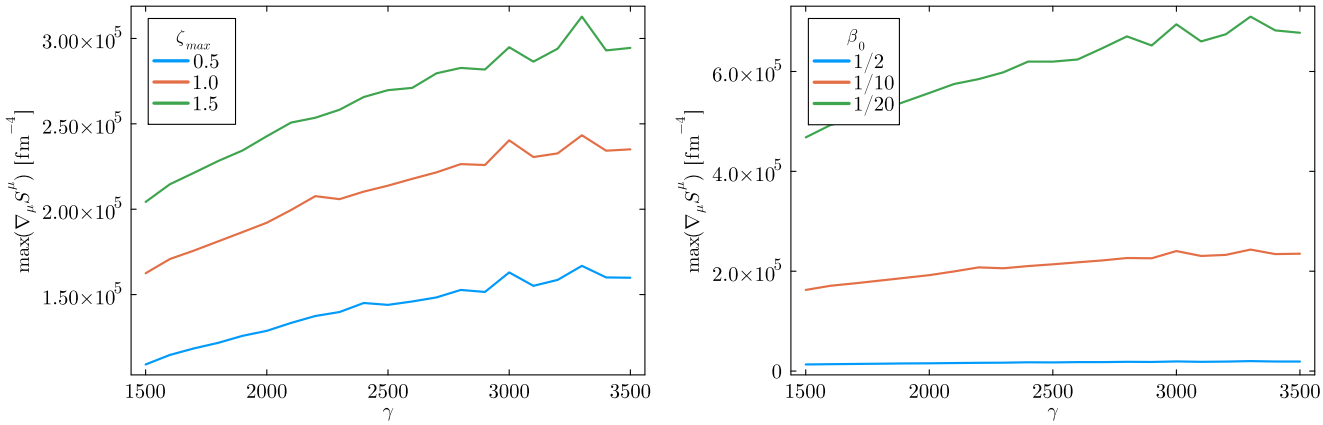

Figure 53: Maximal value of the entropy production as function of the Lorentz γ factor. The left panel additionally varies the bulk viscosity by changing $(\zeta/s)_{\max}$, while the right panel varies the bulk relaxation parameter β_1.

When considering fig. 52 the natural question arises, how the total produced entropy depends on the collision energy, since more entropy is produced, but during a shorter time. Integrating these curves shows that, contrary to the naive expectation, the total produced entropy decreases for increasing collision energy. This can be seen in fig. 54, where the bulk viscosity and relaxation time have been varied again. The decreasing entropy can be attributed to the shorter contraction and expansion phase. Since the Hubble rate dictates the expansion dynamics of the universe, it forces a very short expansion phase. In a real collision, the initial contraction will also be very short due to the high velocity of the two nuclei. Having said that, the subsequent expansion of the real collision is not driven by an external force, such as the Hubble rate, but is rather driven by the pressure gradients of the system. This leads to a prolonged expansion phase [12], in which more entropy is produced at higher collision energies. Despite the slightly unusual scaling with the collision energy, the total produced entropy scales again with the viscosity amplitude and is anti-proportional to the relaxation time parameter β_0.

[12] The expansion time can be defined as time between the initial collision and the point in time, when every part of the system has frozen-out, leading to longer expansion times for systems with larger collision energy, due to the bigger initial heating.

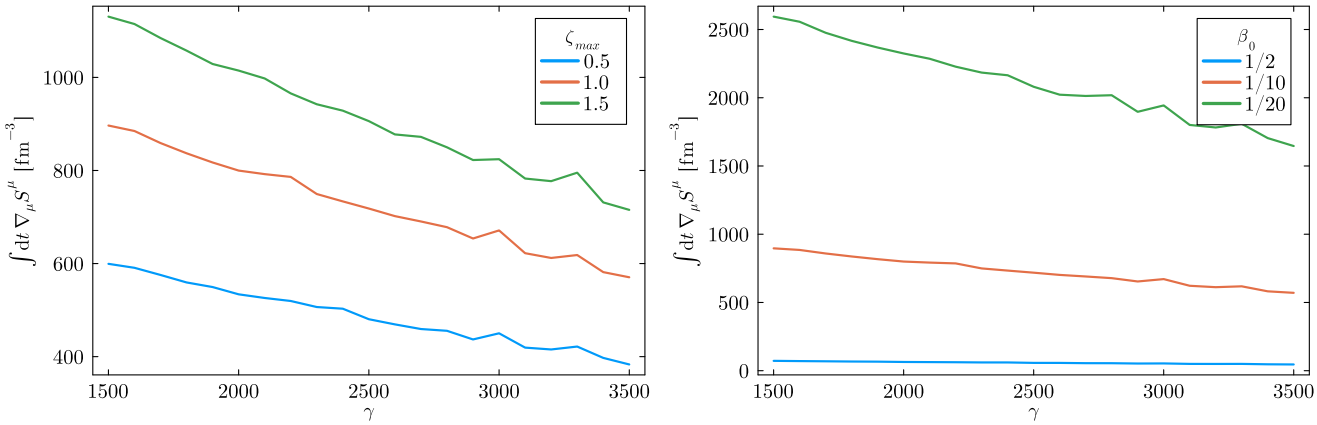

Figure 54: Total entropy produced during the contraction and expansion of the system as function of γ. In the left panel the magnitude of the viscosity is varied while in the right panel the magnitude of its relaxation time is varied.

The full dependence of the produced entropy on the bulk viscosity and the bulk relaxation time is summarized fig. 55. As established before, more entropy is being produced in systems with larger viscosity. By definition, in the case of zero viscosity no entropy is being produced. The slope of the produced entropy when increasing the viscosity increases with decreasing relaxation time. This can again be attributed to the speed at which the system can react to the external contraction and expansion.

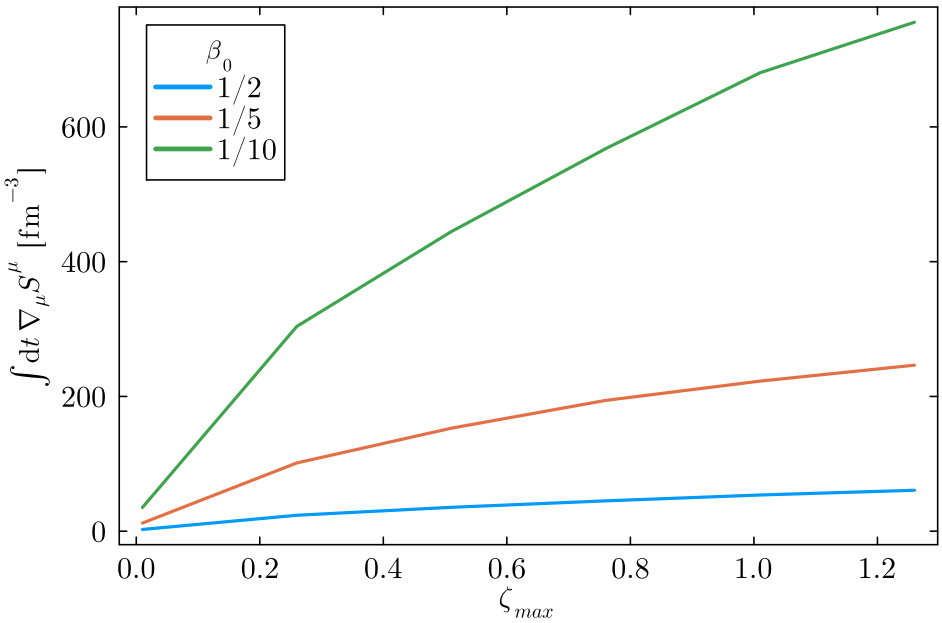

Figure 55: Total produced entropy as function of the viscosity for different relaxation times. As established before, more entropy is being produced in systems with larger viscosity. By definition, in the case of zero viscosity no entropy is being produced. The slope of the produced entropy when increasing the viscosity increases with decreasing relaxation time.

As hinted in the previous discussion, the peak temperature reached during the evolution also scales with the collision energy. The concrete scaling with the collision energy can be seen in fig. 56. As before, the viscosity and relaxation times have been varied. The peak temperature reached during the evolution of the system mirrors the dependence of the previously examined quantities by increasing for larger viscosity and collision energy and smaller relaxation time.

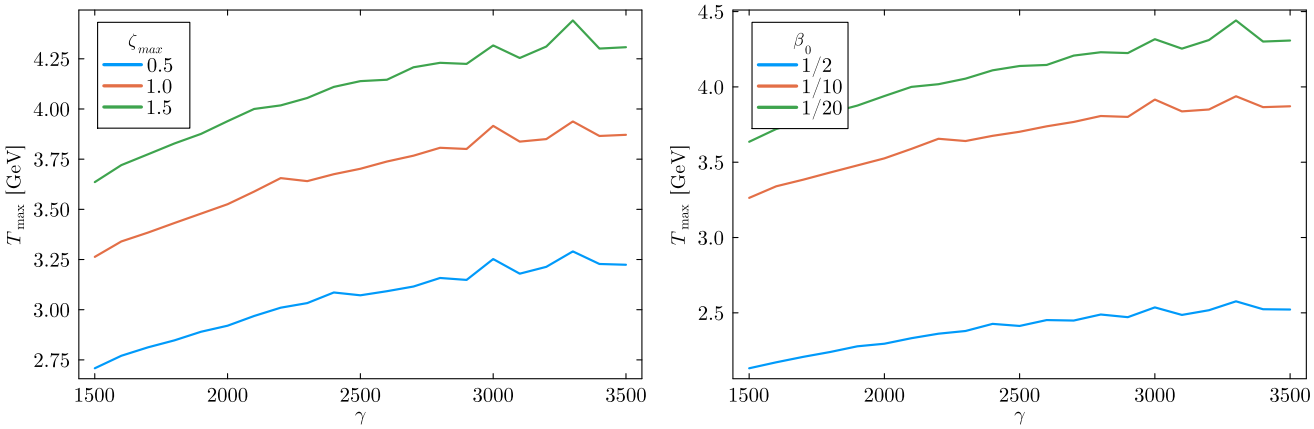

Figure 56: Peak temperature reached during the evolution as function of the collision energy with varying viscosities and relaxation times. As before, the viscosity and relaxation times have been varied.

The ratio between the relaxation time of the system and the expansion/contraction time is crucial for the final state of the system, as can be seen when considering the final temperature of the system. This is depicted in fig. 57. Similar to the total produced entropy, the final temperature also declines with increasing Lorentz factor γ. This initially counter intuitive behavior can be explained by considering that for larger γ factor, the collision dynamics happens in a shorter time frame. Therefore, the system has less time to react to the contraction and the expansion. Increasing the viscosity allows the system to build up the bulk pressure more easily, resulting in a larger final temperature. Similarly, a shorter relaxation time[13] allows for a faster response of the system.

[13] Note that since a homogeneous universe is considered there are no constraints on the relaxation time stemming from causality. If spatially dependent perturbations are introduced or a non-homogeneous system is considered these bounds have to be taken into consideration.

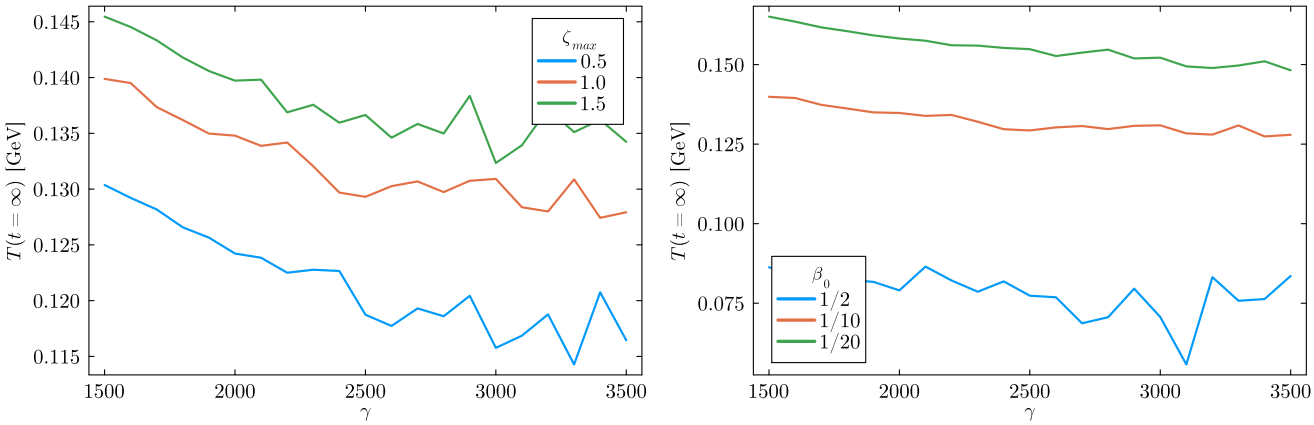

Figure 57: Final temperature reached during the evolution as function of the collision energy with varying viscosities and relaxation times. The final temperature also declines with increasing Lorentz factor γ.

Note that the system shows the typical relaxation behavior after the forced contraction and expansion phase is over. However, due to the steep increase and sharp decline of the bulk pressure the exponential decay is difficult to see in fig. 48. The relaxation can be seen in fig. 58, where the logarithm of the bulk pressure has been plotted with the logarithm of the Hubble rate (a small offset has been added to both curves to avoid any singularities). After the initial build up and subsequent decrease of the bulk pressure, it remains at a non-zero residual value. Since the system is not driven by the Hubble rate anymore and the temperature stays constant, the bulk pressure decays exponentially, as expected from eq. 6.46.

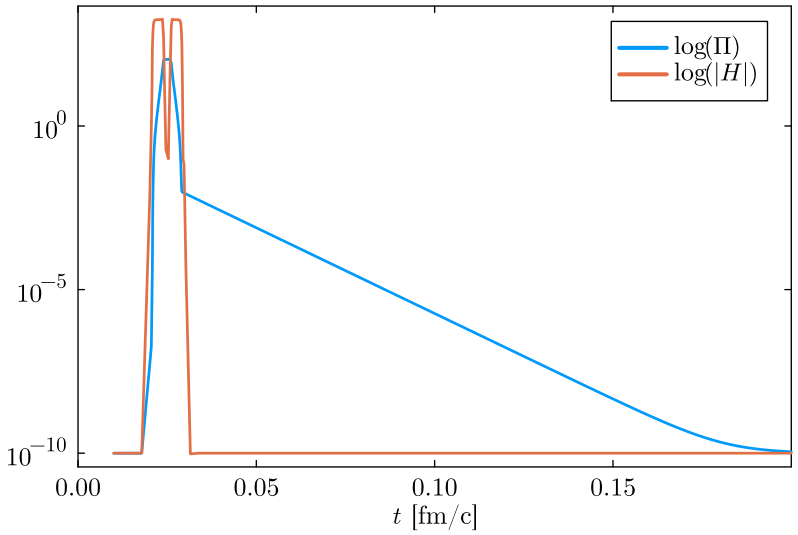

Figure 58: Logarithm of the bulk pressure has together with the logarithm of the Hubble rate (a small offset has been added to both curves to avoid any singularities).

As a final point of the discussion of this system, I want to return to the trajectory of the system through the

phase diagram. The trajectories for different relaxation times are shown in fig. 59. Initially, all trajectories lie on top of each other. When reaching the limit of zero chemical potential, the systems with smaller relaxation times heat up more due to the aforementioned reasons. An interesting observation is that the systems with large relaxation times have a backwards bending trajectory where the temperature and chemical potential increase simultaneously. This can be attributed to the small expansion and contraction phase of the Hubble rate during the turning phase of the universe (see fig. 46). Since the system has a large relaxation time and its viscosity is small at this point (see fig. 47), the external work cannot be absorbed by the bulk pressure and leads to an increase of the temperature and the chemical potential. If the system has a small enough relaxation time, the bulk pressure can build up, resulting in the heating up of the system, during which only the temperature increases.

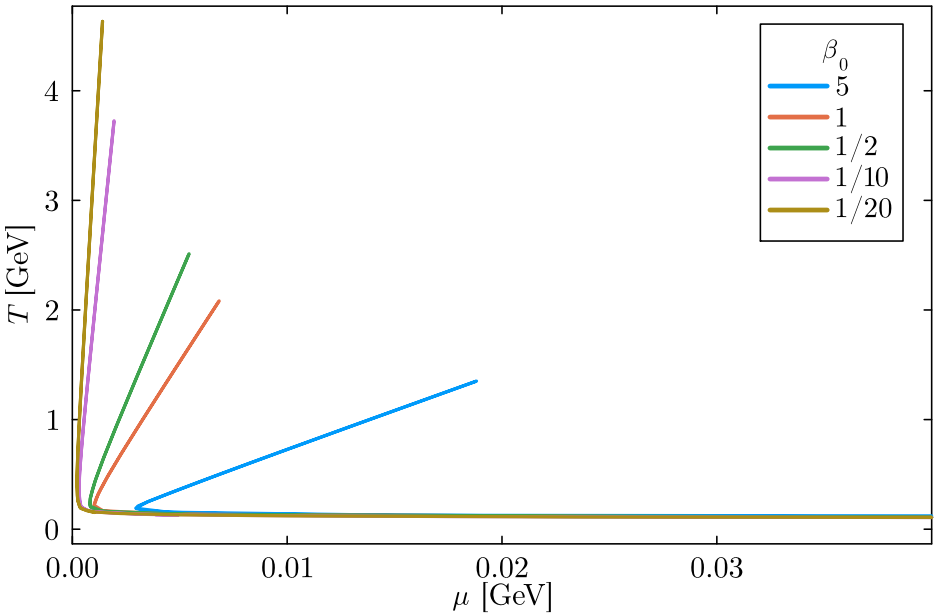

Figure 59: Trajectories of the system through the phase diagram for different relaxation times. Initially, all trajectories lie on top of each other. When reaching the limit of zero chemical potential, the systems with smaller relaxation times heat up more with the systems with large relaxation times having a backwards bending trajectory.

7. Summary and Outlook

7.1. Summary

In this thesis the Fluid$u$M framework has been extended and employed in various applications. Among the extensions of the framework are:

- Consistent calculation of the spectra expressions up to linear order in perturbations. These spectra expressions were used in the applications of the Fluid$u$M framework and are also used in the calculation of flow coefficients.
- Verification of the Fluid$u$M framework. The Fluid$u$M framework is based on a background-fluctuation splitting ansatz and directly evolves event averaged quantities and is therefore fundamentally different from other event-by-event frameworks. The equivalence of the two approaches has been shown by comparing the Fluid$u$M framework with the framework developed by the Duke group.
- Development of a new perturbation basis based on polynomials. This choice of basis functions is inspired by the definition of the initial state eccentricities and allows for an efficient calculation of the flow coefficients.

These extensions and the verification of the framework have allowed several applications of Fluid$u$M, making use of its inherent speed and flexibility. These applications include

- Bayesian parameter extraction. One important application of the Fluid$u$M framework is the combination with Bayesian inference in order to infer QGP parameters from experimental data. This analysis goes beyond the parameter extractions done in different frameworks because the speed of Fluid$u$M allows for an additional quantification of the theoretical model uncertainties.
- Connection to nuclear structure. This application motivated by the isobar data taken at RHIC examined the impact of various parameters governing the early dynamics of the collision on the final multiplicity ratios. This analysis showed that heavy-ion collisions can in fact be used to infer information about the nuclear structure of the ions since some observables are very sensitive to nuclear structure parameters (e.g. the multiplicity ratio to the neutron skin thickness).
- Direct photon analysis. For this application the Fluid$u$M framework was used to predict the spectra of neutral particles needed for the experimental analysis of the direct photons. This novel method is based on data-driven predictions for the η/π^0 ratio.

The second part of this thesis was dedicated to the development of a new description for the initial stages of a heavy-ion collision. This description was obtained by extending the fluid-dynamic description to times before the collision, treating the incoming nuclei already as drops of nuclear matter. One major step in the development of this framework was the construction of an equation of state valid in a large range of the QCD phase diagram. This was achieved by combining different models via a neural network. A second

major step was the preparation of the incoming nuclei together with the initialization of the fluid fields via Landau matching. This was used as a first model of an interactionless collision. The full solution to the dynamics of the system allows to investigate a contracting and expanding Hubble-type universe. Here the entropy production as function of the viscosity and the corresponding relaxation time were investigated.

7.2. Outlook

There are already several ideas to employ and extend the tools developed in this work. I will start out by presenting extensions of the Fluid$u$M framework that are either being planned or that are already being worked on.

Implementation of Fluid$u$M in julia Currently, there is work being done on implementing the Fluid$u$M framework in the julia language. An implementation of Fluid$u$M in julia has several benefits compared to the implementation in Mathematica:

- julia is a general purpose programming language with high execution speed
- julia is an open source software making it easier to access
- julia is a very flexible language allowing for example the inclusion of libraries from other languages or differentiable programming

The increased speed and easier parallelization can for example be used to include more parameters in the fit or the parameter scan, presented in section 5. The possibility to write differentiable code in julia also opens up great possibilities for the parameter extraction of QGP parameters.

Higher order corrections & Hartree approximation The equations of motion derived for Fluid$u$M are obtained by using a background-fluctuation splitting ansatz. The equations for the fluctuations are calculated by linearizing in the formal expansion parameter. Therefore, the extension of the framework beyond linear order in perturbations is an obvious further development. The set of deterministic fluid-dynamic equations of motion together with the stochastic nature of the initial conditions can be used to express the Fluid$u$M framework as a statistical field theory. This allows the introduction of an action, generating the fluid-dynamic equations of motion. Evidently, a background-fluctuation splitting can also be applied to an action of a statistical field theory. This allows to generate equations of motions also for higher order correlation functions, such as the two-point function. One possible way of obtaining an equation governing the dynamics of the two-point function is for example the Hartree approximation, in which the equations of motion for the background fields get altered by the presence of the two-point function (for more details, see e.g. [13]).
Evidently, the two-point function will also have an influence on the particles created at the freeze-out. Therefore the methods described in section 4 have to be extended to account for this. Since the two-point function is an object of second order in perturbations, it will generate higher order tensors $p^\mu p^\nu \ldots$, appearing

in the integration over the freeze-out. After the decomposition of these higher order tensors the methodology presented above can be applied.

Out of equilibrium corrections from maximum entropy Recently a new way of computing the out of equilibrium corrections was proposed in [146] based on maximizing the entropy of the particle distribution function. This framework can be used to compute the single particle distribution function with minimal assumptions. Therefore, it is ideal to simultaneously include multiple out of equilibrium corrections, e.g. stemming from the presence of non-vanishing shear and bulk viscosities, as well as transport phenomena such as heavy-quark or baryon diffusion. In order to calculate particle spectra including resonance decays based on these distribution functions the framework presented in section 4 has to be extended to account for their non-linearity.

Flow coefficients and higher order correlations The inclusion of flow coefficients (see section 4) into the parameter extraction presented in section 5 is one of the main objectives at the time of writing this thesis. It will allow to find better constraints on the bulk and especially the shear viscosity, since the flow coefficients are more sensitive to these quantities. The speed of Fluid$u$M together with the fact that the statistics are gathered on the level of the initial conditions makes Fluid$u$M an ideal tool to study observables based on higher order correlation functions, which usually are numerically demanding due to the large required statistics. Among these are flow coefficients calculated from higher order correlation functions, e.g. $v_2\{4\}$ or $v_2\{6\}$ which can be used to e.g. gain valuable insights in the distribution function of the initial fluctuations. Another interesting type of observable is the correlation between the mean transverse momentum and the flow coefficients [147, 148]

$$\rho(v_n^2, \langle p_\mathrm{T}\rangle) = \frac{\langle\langle p_\mathrm{T}\rangle\, v_n^2\rangle - \langle\langle p_\mathrm{T}\rangle\rangle\, \langle v_n^2\rangle}{\sigma_{p_\mathrm{T}}\sigma_{v_n^2}}, \tag{7.1}$$

which can be used to study nuclear deformations of the heavy ions in greater detail. Seeing as these correlations include two different observables, they are statistically very demanding, making Fluid$u$M an ideal tool for their examination.

Universe with separate transverse and longitudinal dynamics As a final point I want to explore possible continuations of the extension of the fluid-dynamic description to times before the collision, presented in section 6. The final goal is to obtain a full 3+1 dimensional description of the system allowing the detailed study of the entropy production during the collision. However, since the interplay between the different out of equilibrium terms can be challenging to describe, it is useful to study some in between models. A natural first choice would be a universe with two scale factors $a(t)$ and $b(t)$, allowing for separate transverse and longitudinal dynamics. The metric for this system reads as

$$\mathrm{d}s^2 = -\mathrm{d}t^2 + a(t)^2(\mathrm{d}x^2 + \mathrm{d}y^2) + b(t)^2\mathrm{d}z^2. \tag{7.2}$$

Here the two scale factors $a(t)$ and $b(t)$ allow to have a fast initial contraction with a slower expansion that mimics the radial expansion during a heavy-ion collision. Evidently this model still has the shortcoming of an externally driven radial expansion, but since it has fewer symmetries than the model presented in section 6, it has a non-trivial shear viscous pressure. A final step towards the full 3+1 dimensional setting is the 1+1 dimensional setting discussed above, which is equivalent to the collision of two nuclei with infinite extend in the x-y-plane. This 1+1 dimensional setting includes a non-trivial baryon diffusion current as well. All of these models can also be used to test calculations of transport coefficients at non-vanishing densities and temperatures.

Appendix A Hydrodynamic fields in the general Bjorken coordinate frame

In this section I give the expressions for the fluid velocity, shear stress tensor and diffusion current transformed back to Bjorken coordinates. The transformations from the orthogonal frame to Bjorken coordinates are given by

$$u^\mu = v_a^\mu u^a, \quad \nu^\mu = v_a^\mu \nu^a, \quad \pi^{\mu\rho} = v_a^\mu v_b^\rho \pi^{ab}. \tag{A.1}$$

The diffusion current in the orthogonal frame is given by

$$\bar{\nu}_i^a = (0,\bar{\nu}_i,0,0), \quad \text{and} \tag{A.2}$$

$$\delta\nu_i^a = (-\delta v_1 \bar{\nu}_i, \delta\nu_1^i, \delta\nu_2^i, \delta\nu_3^i), \tag{A.3}$$

where the index i runs over the conserved charges. The expressions in the Bjorken frame for the fluid velocity and diffusion currents for their background and perturbations read as

$$u^\mu = (\bar{\gamma}, \bar{v}\bar{\gamma},0,0) + (\bar{v}\bar{\gamma}\delta v_1, \bar{\gamma}\delta v_1, \delta v_2/r, \delta v_3/\tau) \tag{A.4}$$

$$\nu^\mu = (\bar{v}\bar{\gamma}\bar{\nu}, \bar{\gamma}\bar{\nu},0,0) + (\bar{\gamma}(\bar{v}\delta\nu_1 - \bar{\nu}\delta v_1),\bar{\gamma}(\delta\nu_1 - \bar{v}\bar{\nu}\delta v_1),\delta\nu_2/r,\delta\nu_3/\tau) \tag{A.5}$$

Note that the diffusion current now also depends on the background fluid velocity. Similarly the shear stress tensor also gains contributions from the background fluid velocity through the transformation and is given by

$$\pi^{\mu\nu} = \begin{pmatrix} -\bar{v}^2\bar{\gamma}^2\bar{\pi}^t & -\bar{v}\bar{\gamma}^2\bar{\pi}^t & 0 & 0 \\ -\bar{v}\bar{\gamma}^2\bar{\pi}^t & -\bar{\gamma}^2\bar{\pi}^t & 0 & 0 \\ 0 & 0 & \bar{\pi}^{22}/r^2 & 0 \\ 0 & 0 & 0 & \bar{\pi}^{33}/\tau^2 \end{pmatrix} \tag{A.6}$$

$$+ \begin{pmatrix} -\bar{v}\bar{\gamma}^2(\bar{v}\delta\pi^t - 2\delta v_1\bar{\pi}^t) & -\bar{\gamma}(\bar{v}\delta\pi^t - \delta v_1(1+\bar{v}^2)\bar{\pi}^t) & \bar{\gamma}(\bar{v}\delta\pi^{12} - \delta v_2\bar{\pi}^{22})/r & \bar{\gamma}(\bar{v}\delta\pi^{13} - \delta v_3\bar{\pi}^{33})/\tau \\ -\bar{\gamma}(\bar{v}\delta\pi^t - \delta v_1(1+\bar{v}^2)\bar{\pi}^t) & -\bar{\gamma}^2(\delta\pi^t - 2\delta v_1\bar{v}\bar{\pi}^t) & \bar{\gamma}(\delta\pi^{12} - \delta v_2\bar{v}\bar{\pi}^{22})/r & \bar{\gamma}(\delta\pi^{13} - \bar{v}\delta v_3\bar{\pi}^{33})/\tau \\ \bar{\gamma}(\bar{v}\delta\pi^{12} - \delta v_2\bar{\pi}^{22})/r & \bar{\gamma}(\delta\pi^{12} - \delta v_2\bar{v}\bar{\pi}^{22})/\tau & \delta\pi^{22}/r^2 & \delta\pi^{23}/r\tau \\ \bar{\gamma}(\bar{v}\delta\pi^{13} - \delta v_3\bar{\pi}^{33})/\tau & \bar{\gamma}(\delta\pi^{13} - \delta v_3\bar{v}\bar{\pi}^{33})/\tau & \delta\pi^{23}/r\tau & \delta\pi^{33}/\tau^2 \end{pmatrix}. \tag{A.7}$$

As mentioned before, a description in terms of the fields in the orthogonal frame is equivalent to a description in terms of the fields in the Bjorken frame. When using the description in terms of the orthogonal fields, the components of the tetrad are promoted to independent fluid fields with their own evolution equation, accounting for the simplified equations of the fluid velocity.

Appendix B Tensor decomposition

In this section I give the tensor decompositions needed for the calculations of the kernels, as presented in section 4. Since the appearing terms are fully symmetric, I will only present the decompositions for symmetric tensors with up to four Lorentz indices, i.e. p^μ, $p^\mu p^\nu$, $p^\mu p^\nu p^\rho$ and $p^\mu p^\nu p^\rho p^\sigma$.

B.1 Decomposition of p^μ

The decomposition of p^μ is given by one scalar

$$\tilde{p}^\mu = E_p u^\mu \tag{B.1}$$

and one vector

$$\hat{p}^\mu = p^\mu - E_p u^\mu. \tag{B.2}$$

B.2 Decomposition of $p^\mu p^\nu$

The decomposition of $p^\mu p^\nu$ is given by two scalars

$$1.)\tilde{p}^\mu \tilde{p}^\nu \tag{B.3}$$

$$2.)\frac{1}{3}|\mathbf{p}|^2 \Delta^{\mu\nu}, \tag{B.4}$$

two vectors

$$1.)\hat{p}^\mu \tilde{p}^\nu \tag{B.5}$$

$$2.)\tilde{p}^\mu \hat{p}^\nu, \tag{B.6}$$

and one traceless, symmetric tensor

$$\hat{p}^\mu \hat{p}^\nu - \frac{1}{3}|\mathbf{p}|^2 \Delta^{\mu\nu}. \tag{B.7}$$

B.3 Decomposition of $p^\mu p^\nu p^\rho$

The decomposition of $p^\mu p^\nu p^\rho$ is given by four scalars

$$1.)\ \tilde{p}^\mu \tilde{p}^\nu \tilde{p}^\rho \tag{B.8}$$

$$2.)\ \frac{1}{3}|\mathbf{p}|^2 \tilde{p}^\mu \Delta^{\nu\rho} + 2 \text{ permutations}, \tag{B.9}$$

six vectors

$$1.)\ \tilde{p}^\mu\tilde{p}^\nu\hat{p}^\rho + 2 \text{ permutations} \tag{B.10}$$

$$2.)\ \frac{1}{5}|\mathbf{p}|^2\Delta^{\mu\nu}\hat{p}^\rho + 2 \text{ permutations}, \tag{B.11}$$

three symmetric and traceless two tensors

$$\tilde{p}^\mu(\hat{p}^\nu\hat{p}^\rho - \frac{1}{3}|\mathbf{p}|^2\Delta^{\nu\rho}) + 2 \text{ permutations}, \tag{B.12}$$

and one symmetric and traceless three tensor

$$\hat{p}^\mu\hat{p}^\nu\hat{p}^\rho - \frac{1}{5}|\mathbf{p}|^2(\hat{p}^\mu\Delta^{\nu\rho} + \hat{p}^\nu\Delta^{\mu\rho} + \hat{p}^\rho\Delta^{\mu\nu}). \tag{B.13}$$

B.4 Decomposition of $p^\mu p^\nu p^\rho p^\sigma$

The decomposition of $p^\mu p^\nu p^\rho p^\sigma$ is given by eight scalars

$$1.)\ \tilde{p}^\mu\tilde{p}^\nu\tilde{p}^\rho\tilde{p}^\sigma \tag{B.14}$$

$$2.)\ \frac{1}{3}|\mathbf{p}|^2\Delta^{\mu\nu}\tilde{p}^\rho\tilde{p}^\sigma + 5 \text{ permutations} \tag{B.15}$$

$$3.)\ \frac{1}{15}|\mathbf{p}|^4(\Delta^{\mu\nu}\Delta^{\rho\sigma} + \Delta^{\mu\rho}\Delta^{\nu\sigma} + \Delta^{\mu\sigma}\Delta^{\nu\rho}), \tag{B.16}$$

eight vectors

$$1.)\ \hat{p}^\mu\tilde{p}^\nu\tilde{p}^\rho\tilde{p}^\sigma + 3 \text{ permutations} \tag{B.17}$$

$$2.)\ \frac{1}{5}|\mathbf{p}|^2(\Delta^{\mu\nu}\hat{p}^\rho + \Delta^{\mu\rho}\hat{p}^\nu + \Delta^{\nu\rho}\hat{p}^\rho)\tilde{p}^\sigma + 3 \text{ permutations}, \tag{B.18}$$

twelve symmetric and traceless two tensors

$$1.)\ (\hat{p}^\mu\hat{p}^\nu - \frac{1}{3}|\mathbf{p}|^2\Delta^{\mu\nu})\tilde{p}^\rho\tilde{p}^\sigma + 5 \text{ permutations} \tag{B.19}$$

$$2.)\ \frac{1}{7}(\hat{p}^\mu\hat{p}^\nu - \frac{1}{3}|\mathbf{p}|^2\Delta^{\mu\nu})\Delta^{\rho\sigma} + 5 \text{ permutations}, \tag{B.20}$$

four symmetric and traceless three tensors

$$(\hat{p}^\mu\hat{p}^\nu\hat{p}^\rho - \frac{1}{5}|\mathbf{p}|^2(\Delta^{\mu\nu}\hat{p}^\rho + \Delta^{\mu\rho}p^\nu + \Delta^{\nu\rho}p^\mu))\tilde{p}^\sigma + 3 \text{ permutations}, \tag{B.21}$$

and one symmetric and traceless four tensor

$$\begin{aligned}
&\hat{p}^\mu\hat{p}^\nu\hat{p}^\sigma\hat{p}^\rho + \frac{1}{35}|\mathbf{p}|^4(\Delta^{\mu\nu}\Delta^{\rho\sigma} + \Delta^{\mu\rho}\Delta^{\nu\sigma} + \Delta^{\mu\sigma}\Delta^{\rho\nu}) \\
&- \frac{1}{7}[\Delta^{\mu\nu}|\mathbf{p}|^2\hat{p}^\rho\hat{p}^\sigma + \Delta^{\mu\rho}|\mathbf{p}|^2\hat{p}^\nu\hat{p}^\sigma + \Delta^{\mu\sigma}|\mathbf{p}|^2\hat{p}^\rho\hat{p}^\nu \\
&+ \Delta^{\nu\rho}|\mathbf{p}|^2\hat{p}^\mu\hat{p}^\sigma + \Delta^{\nu\sigma}|\mathbf{p}|^2\hat{p}^\mu\hat{p}^\rho + \Delta^{\rho\sigma}|\mathbf{p}|^2\hat{p}^\mu\hat{p}^\nu] \qquad \text{(B.22)} \\
=&\hat{p}^\mu\hat{p}^\nu\hat{p}^\sigma\hat{p}^\rho - [\frac{1}{7}\Delta^{\mu\nu}|\mathbf{p}|^2(\hat{p}^\rho\hat{p}^\sigma - \frac{1}{3}|\mathbf{p}|^2\Delta^{\rho\sigma}) + 5 \text{ perms}] \\
&+ \frac{1}{15}|\mathbf{p}|^4\Delta^{\mu\nu}\Delta^{\rho\sigma} + 2 \text{ perms.} \qquad \text{(B.23)}
\end{aligned}$$

Appendix C Distribution functions and transformation rules

In this section I give all the expressions to initialize the distribution functions on the freeze-out hypersurface for the thermal part and the transformation functions $A_i(w)$ for the decay map. The distribution functions can be obtained by factoring out the tensor and constant fluid field contributions. Since the contributions are all additive, the vector distribution function after a two-body decay is given by

$$g^{\mu}_{b,i}(p,u) = \frac{\nu_a}{\nu_b} \int \frac{\mathrm{d}k^3}{(2\pi)^3 2E_k} D^a_{b|c}(p^\nu k_\nu) g^{\mu}_{a,i}(k,u) \tag{C.1}$$

for a decay $a \to b + c$ and a given contribution type i. Using the orthogonality of the different, irreducible representations of $SO(3)$, this transformation rule can be simplified into a scalar integral

$$f^b_{i,s}(E_p) = B \frac{\nu_a}{\nu_b} \frac{m_a^2}{m_b^2} \frac{1}{2} \int_{-1}^{1} \mathrm{d}w \; A_s(w) f^a_{i,s}(E(w)) \tag{C.2}$$

as seen before for contribution type i and spin s of the irreducible representation. For the equilibrium part of the distribution function and its linearizations, the distribution functions are given by

$$f_s^{\mathrm{eq}} = f_{\mathrm{eq}} \tag{C.3}$$

$$f_s^{\mathrm{eqTemp}} = f_{\mathrm{eq}}(1 \pm f_{\mathrm{eq}})(\beta E_p - \alpha) \tag{C.4}$$

$$f_s^{\mathrm{eqChem}} = f_{\mathrm{eq}}(1 \pm f_{\mathrm{eq}}) \tag{C.5}$$

$$f_s^{\mathrm{eqVel}} = f_{\mathrm{eq}}(1 \pm f_{\mathrm{eq}}). \tag{C.6}$$

Since the background equilibrium part and its perturbations in temperature and chemical potential are all proportional to p^μ, they share the same decomposition with the same terms appearing in the final spectra expressions. Therefore they also share the same transformation rules

$$A_0^{\mathrm{eq}} = A_0^{\mathrm{eqTemp}} = A_0^{\mathrm{eqChem}} = \frac{Q(w)}{|\mathbf{p}|}, \tag{C.7}$$

$$A_1^{\mathrm{eq}} = A_1^{\mathrm{eqTemp}} = A_1^{\mathrm{eqChem}} = \frac{E(w)}{E_p}, \tag{C.8}$$

$$A_0^{\mathrm{eqVel}} = \frac{E(w)^2 - m_a^2}{|\mathbf{p}|^2}, \quad A_1^{\mathrm{eqVel}} = A_0^{\mathrm{eq}} A_1^{\mathrm{eq}}, \tag{C.9}$$

$$A_2^{\mathrm{eqVel}} = \frac{3}{2} \frac{Q(w)^2}{|\mathbf{p}|^2} - \frac{1}{2} \frac{E(w)^2 - m_a^2}{|\mathbf{p}|^2}. \tag{C.10}$$

To obtain these transformation rules, in principle one would need to carry out the integration eq. C.1 for each set of contributions with the same spin to arrive at eq. C.2. However, this way of obtaining the transformation rules is very tedious. A more convenient way of obtaining the transformation rules is to start again from eq. C.1 with the decomposition of g^μ already applied. To obtain a scalar integration, both sides are contracted with the appropriate amount of momenta $p^\mu p^\nu \ldots$. The appearing possible contractions are

given by

$$p_\mu \Delta^{\mu\nu} p_\nu = |\mathbf{p}|^2, \quad k_\mu \Delta^{\mu\nu} k_\nu = E(w)^2 - m_a^2, \quad p_\mu \Delta^{\mu\nu} k_\nu = Q(w)|\mathbf{p}|. \tag{C.11}$$

Since all the appearing quantities only depend on w, the integration over the decay operator now is trivial and can be brought into the required form of eq. C.2. The distribution functions for terms proportional to the shear stress tensor are given by

$$f_s^{\text{shear}} = f_{\text{eq}}(1 \pm f_{\text{eq}}) \tag{C.12}$$

$$f_s^{\text{shearTemp}} = f_{\text{eq}}(1 \pm f_{\text{eq}}) \left((2 \pm f_{\text{eq}})(\beta E_p - \alpha) + \beta \partial_\beta \ln\left(\frac{e+p}{\beta^2}\right)\right) \tag{C.13}$$

$$f_s^{\text{shearChem}} = f_{\text{eq}}(1 \pm f_{\text{eq}}) \left((2 \pm f_{\text{eq}}) - \partial_\alpha \ln(e+p)\right) \tag{C.14}$$

$$f_s^{\text{shearVel}} = f_{\text{eq}}(1 \pm f_{\text{eq}})(2 \pm f_{\text{eq}}) \tag{C.15}$$

$$f_s^{\text{shearShear}} = f_{\text{eq}}(1 \pm f_{\text{eq}}) \tag{C.16}$$

Similar to the equilibrium case, the background shear part and its perturbations in temperature and chemical potential share the same tensor structure with the same contractions. Therefore their transformation rules are also the same

$$A_0^{\text{shear}} = A_0^{\text{shearTemp}} = A_0^{\text{shearChem}} = 0, \tag{C.17}$$

$$A_1^{\text{shear}} = A_1^{\text{shearTemp}} = A_1^{\text{shearChem}} = A_0^{\text{eqVel}} A_0^{\text{eq}}, \tag{C.18}$$

$$A_2^{\text{shear}} = A_2^{\text{shearTemp}} = A_2^{\text{shearChem}} = A_2^{\text{eqVel}} A_1^{\text{eq}}, \tag{C.19}$$

$$A_3^{\text{shear}} = A_3^{\text{shearTemp}} = A_3^{\text{shearChem}} = \frac{5}{2}\frac{Q(w)^3}{|\mathbf{p}|^3} - \frac{3}{2}\frac{Q(w)}{|\mathbf{p}|}\frac{E(w)^2 - m_a^2}{|\mathbf{p}|^2}, \tag{C.20}$$

$$\tag{C.21}$$

$$A_0^{\text{shearShear}} = \frac{E(w)}{E_p}\frac{E_p^2 E(w)^2 + |\mathbf{p}|^2(E(w)^2 - m_a^2)}{E_p^4 + |\mathbf{p}|^4} \tag{C.22}$$

$$A_1^{\text{shearShear}} = \frac{Q(w)}{|\mathbf{p}|}\frac{5E_p^2 E(w)^2 + |\mathbf{p}|^2(E(w)^2 - m_a^2)}{5E_p^4 + |\mathbf{p}|^4}, \tag{C.23}$$

$$A_2^{\text{shearShear}} = A_1^{\text{eq}} A_1^{\text{eqVel}}, \quad A_3^{\text{shearShear}} = A_3^{\text{shear}}, \tag{C.24}$$

$$A_0^{\text{shearVel}} = \left(A_0^{\text{eqVel}}\right)^2, \quad A_1^{\text{shearVel}} = A_0^{\text{eqVel}} A_1^{\text{eqVel}}, \tag{C.25}$$

$$A_2^{\text{shearVel}} = A_0^{\text{eqVel}} A_2^{\text{eqVel}}, \quad A_3^{\text{shearVel}} = A_1^{\text{eq}} A_3^{\text{shear}}, \tag{C.26}$$

$$\begin{aligned} A_4^{\text{shearVel}} = {} & \frac{35Q(w)^4 - 30Q(w)^2(E(w)^2 - m_a^2) +}{8|\mathbf{p}|^4} \\ & + \frac{3(E(w)^2 - m_a^2)^2}{8|\mathbf{p}|^4} \end{aligned} \tag{C.27}$$

The distribution functions for terms proportional to the bulk pressure are given by

$$f_s^{\text{bulk}} = f_{\text{eq}}(1 \pm f_{\text{eq}}) \left(\beta E_p(1/3 - c_s^2) - \frac{1}{3}\frac{\beta m^2}{E_p}\right)\frac{\tau_B}{\zeta} \tag{C.28}$$

$$\begin{aligned} f_s^{\text{bulkTemp}} = {} & f_{\text{eq}}(1 \pm f_{\text{eq}}) \left(\beta E_p(1/3 - c_s^2) - \frac{1}{3}\frac{\beta m^2}{E_p}\right)\frac{\tau_B}{\zeta} \\ & \times \left[(2 \pm f_{\text{eq}})(\beta E_p - \alpha)\right. \\ & -\beta\partial_\beta \ln\left(\beta E_p(1/3 - c_s^2) - \frac{1}{3}\frac{\beta m^2}{E_p}\right) \\ & \left.-\beta\partial_\beta \ln\left(\frac{\tau_B}{\zeta}\right)\right] \end{aligned} \tag{C.29}$$

$$\begin{aligned} f_s^{\text{bulkChem}} = {} & f_{\text{eq}}(1 \pm f_{\text{eq}}) \left(\beta E_p(1/3 - c_s^2) - \frac{1}{3}\frac{\beta m^2}{E_p}\right)\frac{\tau_B}{\zeta} \\ & \times \left[(2 \pm f_{\text{eq}})\right. \\ & +\partial_\alpha \ln\left(\beta E_p(1/3 - c_s^2) - \frac{1}{3}\frac{\beta m^2}{E_p}\right) \\ & \left.+\partial_\alpha \ln\left(\frac{\tau_B}{\zeta}\right)\right] \end{aligned} \tag{C.30}$$

$$\begin{aligned} f_s^{\text{bulkVel}} = {} & f_{\text{eq}}(1 \pm f_{\text{eq}})\left[(2 \pm f_{\text{eq}})\right. \\ & \times \left(\beta E_p(1/3 - c_s^2) - \frac{1}{3}\frac{\beta m^2}{E_p}\right) \\ & \left.-(1/3 - c_s^2) - \frac{1}{3}\frac{m^2}{E_p^2}\right]\frac{\tau_B}{\zeta} \end{aligned} \tag{C.31}$$

$$f_s^{\text{bulkBulk}} = f_{\text{eq}}(1 \pm f_{\text{eq}}) \left(\beta E_p(1/3 - c_s^2) - \frac{1}{3}\frac{\beta m^2}{E_p}\right)\frac{\tau_B}{\zeta}. \tag{C.32}$$

In the case of bulk corrections, the fact that most of the terms have the same tensor structure as the equilibrium contributions can be used. The transformation rules are given by

$$A_s^{\text{bulk}} = A_s^{\text{bulkTemp}} = A_s^{\text{bulkChem}} = A_s^{\text{bulkBulk}} = A_s^{\text{eq}}, \tag{C.33}$$

$$A_s^{\text{bulkVel}} = A_s^{\text{eqVel}}. \tag{C.34}$$

For the diffusion contribution to the spectra, the distribution functions are given by

$$f_s^{\text{diff}} = \frac{f_{\text{eq}}(1 \pm f_{\text{eq}})}{\kappa} \left[\frac{n_B}{e+p} - \frac{Q_B}{E_P} \right] \tag{C.35}$$

$$\begin{aligned} f_s^{\text{diffTemp}} = & \frac{f_{\text{eq}}(1 \pm f_{\text{eq}})}{\kappa} \left[\frac{n_B}{e+p} - \frac{Q_B}{E_P} \right] \\ & \times \left((2 \pm f_{\text{eq}})(\beta E_p - \alpha) - \beta \partial_\beta \ln \left(\frac{n_B}{e+p} - \frac{Q_B}{E_P} \right) \right. \\ & \left. + \beta \partial_\beta \ln(\kappa) \right) \end{aligned} \tag{C.36}$$

$$\begin{aligned} f_s^{\text{diffChem}} = & \frac{f_{\text{eq}}(1 \pm f_{\text{eq}})}{\kappa} \left[\frac{n_B}{e+p} - \frac{Q_B}{E_P} \right] \\ & \times \left((1 \pm f_{\text{eq}}) - \partial_\alpha \ln \left(\frac{n_B}{e+p} \right) + \partial_\alpha \ln(\kappa) \right) \end{aligned} \tag{C.37}$$

$$\begin{aligned} f_s^{\text{diffVel}} = & \frac{f_{\text{eq}}(1 \pm f_{\text{eq}})}{\kappa} \left[(2 \pm f_{\text{eq}}) \left(\frac{n_B}{e+p} - \frac{Q_B}{E_P} \right) \right. \\ & \left. + \frac{Q_B}{E_p^2} \right] \end{aligned} \tag{C.38}$$

$$f_s^{\text{diffDiff}} = \frac{f_{\text{eq}}(1 \pm f_{\text{eq}})}{\kappa} \left[\frac{n_B}{e+p} - \frac{Q_B}{E_P} \right] \tag{C.39}$$

Since the diffusion current is also orthogonal to the background fluid velocity, most transformation rules can again be expressed in terms of previous ones

$$A_s^{\text{diff}} = A_s^{\text{DiffTemp}} = A_s^{\text{DiffChem}} = A_s^{\text{eqVel}}, \tag{C.40}$$

$$A_0^{\text{DiffVel}} = A_1^{\text{eq}} A_0^{\text{eqVel}}, \quad A_1^{\text{diffVel}} = A_0^{\text{eq}} A_0^{\text{eqVel}}, \tag{C.41}$$

$$A_2^{\text{diffVel}} = A_1^{\text{eq}} A_2^{\text{eqVel}}, \quad A_3^{\text{diffVel}} = A_3^{\text{shear}}, \tag{C.42}$$

$$A_0^{\text{diffDiff}} = \frac{E(w)^2(3E_p^2 + |\mathbf{p}|^2) - m_a^2|\mathbf{p}|^2}{3E_p^4 + |\mathbf{p}|^4} \tag{C.43}$$

$$A_1^{\text{diffDiff}} = A_0^{\text{eq}} A_1^{\text{eq}}, \quad A_2^{\text{diffDiff}} = A_2^{\text{eqVel}}. \tag{C.44}$$

References

[1] F. Wilczek, „The Universe is a strange place“, Nucl. Phys. B Proc. Suppl. **134**, edited by R. Battiston, M. Salamon, E. Katsavounidis, and K. Scholberg, 3–12 (2004).

[2] S. F. Novaes, „Standard model: An Introduction“, in 10th Jorge Andre Swieca Summer School: Particle and Fields (Jan. 1999), pp. 5–102.

[3] J. Butterworth, „The Standard Model: How far can it go and how can we tell?“, Phil. Trans. Roy. Soc. Lond. A **374**, edited by C. David Garner, 20150260 (2016).

[4] J. J. Condon and A. M. Matthews, „ΛCDM Cosmology for Astronomers“, Publ. Astron. Soc. Pac. **130**, 073001 (2018).

[5] S. M. Carroll, „The Cosmological constant“, Living Rev. Rel. **4**, 1 (2001).

[6] A. Freitas, „Precision Tests of the Standard Model“, PoS **TASI2020**, 005 (2021).

[7] M. E. Peskin, „Lectures on the Theory of the Weak Interaction“, in 2016 European School of High-Energy Physics (2017), pp. 1–70.

[8] A. Einstein, „A Generalized Theory of Gravitation“, Rev. Mod. Phys. **20**, 35–39 (1948).

[9] A. Einstein, „A generalization of the relativistic theory of gravitation“, Annals Math. **46**, 578–584 (1945).

[10] A. Einstein, „Zur Allgemeinen Relativitätstheorie“, Sitzungsber. Preuss. Akad. Wiss. Berlin (Math. Phys.) **1915**, [Addendum: Sitzungsber.Preuss.Akad.Wiss.Berlin (Math.Phys.) 1915, 799–801 (1915)], 778–786 (1915).

[11] A. Einstein, „The Field Equations of Gravitation“, Sitzungsber. Preuss. Akad. Wiss. Berlin (Math. Phys.) **1915**, 844–847 (1915).

[12] A. Einstein, „The Formal Foundation of the General Theory of Relativity“, Sitzungsber. Preuss. Akad. Wiss. Berlin (Math. Phys.) **1914**, 1030–1085 (1914).

[13] A. A. Erschfeld, „Functional methods for cosmic structure formation.“, PhD thesis (U. Heidelberg (main), 2021).

[14] A. Soloviev, „Hydrodynamic attractors in heavy ion collisions: a review“, Eur. Phys. J. C **82**, 319 (2022).

[15] W. Busza, K. Rajagopal, and W. van der Schee, „Heavy Ion Collisions: The Big Picture, and the Big Questions“, Ann. Rev. Nucl. Part. Sci. **68**, 339–376 (2018).

[16] J. Brewer, A. Mazeliauskas, and W. van der Schee, „Opportunities of OO and pO collisions at the LHC“, in Opportunities of OO and pO collisions at the LHC (Mar. 2021).

[17] F. Gross et al., „50 Years of Quantum Chromodynamics“, Eur. Phys. J. C **83**, 1125 (2023).

[18] R. L. Workman et al. (Particle Data Group), „Review of Particle Physics“, PTEP **2022**, 083C01 (2022).

[19] C. Ratti, „Lattice QCD and heavy ion collisions: a review of recent progress“, Rept. Prog. Phys. **81**, 084301 (2018).

[20] P. de Forcrand, „Simulating QCD at finite density“, PoS **LAT2009**, edited by C. Liu and Y. Zhu, 010 (2009).

[21] J. N. Guenther, „Overview of the QCD phase diagram: Recent progress from the lattice“, Eur. Phys. J. A **57**, 136 (2021).

[22] R. Pasechnik and M. Šumbera, „Phenomenological Review on Quark–Gluon Plasma: Concepts vs. Observations“, Universe **3**, 7 (2017).

[23] G. Baym et al., „From hadrons to quarks in neutron stars: a review“, Rept. Prog. Phys. **81**, 056902 (2018).

[24] M. G. Alford, A. Schmitt, K. Rajagopal, and T. Schäfer, „Color superconductivity in dense quark matter“, Rev. Mod. Phys. **80**, 1455–1515 (2008).

[25] Cern courier, quark-matter fireballs hashed out in protvino, `https://cerncourier.com/a/quark-matter-fireballs-hashed-out-in-protvino/`, Feb. 2021.

[26] „The ALICE experiment – A journey through QCD“, (2022).

[27] L. Ruan, „RHIC physics overview“, Front. Phys. China **5**, 205–214 (2010).

[28] A. Accardi et al., „Electron Ion Collider: The Next QCD Frontier: Understanding the glue that binds us all“, Eur. Phys. J. A **52**, edited by A. Deshpande, Z. E. Meziani, and J. W. Qiu, 268 (2016).

[29] C. Shen and U. Heinz, The road to precision: extraction of the specific shear viscosity of the quark-gluon plası 2015.

[30] F. Gelis, E. Iancu, J. Jalilian-Marian, and R. Venugopalan, „The Color Glass Condensate“, Ann. Rev. Nucl. Part. Sci. **60**, 463–489 (2010).

[31] S. Ghosh et al., „Initial conditions from the shadowed Glauber model for Pb + Pb collisions at $\sqrt{s_{NN}} = 2.76$ TeV“, Phys. Rev. C **93**, 054904 (2016).

[32] S. Chatterjee et al., „Initial condition from the shadowed Glauber model“, Phys. Lett. B **758**, 269–273 (2016).

[33] D. d'Enterria and C. Loizides, „Progress in the glauber model at collider energies“, Annual Review of Nuclear and Particle Science **71**, 315–344 (2021).

[34] J. S. Moreland, J. E. Bernhard, and S. A. Bass, „Alternative ansatz to wounded nucleon and binary collision scaling in high-energy nuclear collisions“, Phys. Rev. C **92**, 011901 (2015).

[35] W. Ke, J. S. Moreland, J. E. Bernhard, and S. A. Bass, „Constraints on rapidity-dependent initial conditions from charged-particle pseudorapidity densities and two-particle correlations“, Phys. Rev. C **96**, 044912 (2017).

[36] J. S. Moreland, J. E. Bernhard, and S. A. Bass, „Alternative ansatz to wounded nucleon and binary collision scaling in high-energy nuclear collisions“, Phys. Rev. C **92**, 011901 (2015).

[37] G. Giacalone, A matter of shape: seeing the deformation of atomic nuclei at high-energy colliders, 2021.

[38] S. Schlichting and D. Teaney, „The first fm/c of heavy-ion collisions“, Annual Review of Nuclear and Particle Science **69**, 447–476 (2019).

[39] W. Broniowski, W. Florkowski, M. Chojnacki, and A. Kisiel, „Free-streaming approximation in early dynamics of relativistic heavy-ion collisions“, Physical Review C **80**, 10.1103/physrevc.80.034902 (2009).

[40] B. Schenke, S. Jeon, and C. Gale, „(3+1)D hydrodynamic simulation of relativistic heavy-ion collisions“, Phys. Rev. C **82**, 014903 (2010).

[41] B. Schenke, S. Jeon, and C. Gale, „Elliptic and triangular flow in event-by-event (3+1)D viscous hydrodynamics“, Phys. Rev. Lett. **106**, 042301 (2011).

[42] J.-F. Paquet et al., „Production of photons in relativistic heavy-ion collisions“, Phys. Rev. C **93**, 044906 (2016).

[43] G. Nijs, W. van der Schee, U. Gürsoy, and R. Snellings, „Bayesian analysis of heavy ion collisions with the heavy ion computational framework trajectum“, Physical Review C **103**, 10.1103/physrevc.103.054909 (2021).

[44] S. Floerchinger, E. Grossi, and J. Lion, „Fluid dynamics of heavy ion collisions with Mode expansion (FluiduM)“, Phys. Rev. C **100**, 014905 (2019).

[45] H. Bebie, P. Gerber, J. Goity, and H. Leutwyler, „The role of the entropy in an expanding hadronic gas“, Nuclear Physics B **378**, 95–128 (1992).

[46] P. Huovinen, „Chemical freeze-out temperature in the hydrodynamical description of Au + Au collisions at $\sqrt{s_{NN}} = 200$GeV“, The European Physical Journal A, 10.1140/epja/i2007-10611-3.

[47] J. Weil et al. (SMASH), „Particle production and equilibrium properties within a new hadron transport approach for heavy-ion collisions“, Phys. Rev. C **94**, 054905 (2016).

[48] M. Bleicher et al., „Relativistic hadron-hadron collisions in the ultra-relativistic quantum molecular dynamics model“, Journal of Physics G: Nuclear and Particle Physics **25**, 1859 (1999).

[49] A. Kirchner, E. Grossi, and S. Floerchinger, „Cooper-Frye spectra of hadrons with viscous corrections including feed down from resonance decays“, arXiv:2308.10616 (2023).

[50] L. Vermunt et al., „Mapping QGP properties in Pb–Pb and Xe–Xe collisions at the LHC“, (2023).

[51] A. Kirchner, K. Reygers, and A. Mazeliauskas, „Improved decay photon cocktail for direct photon analyses in nuclear collisions from hydrodynamic modeling of hadron spectra“, (arXiv, in progress).

[52] A. Kirchner et al., „Extending the fluid description to times before the collision“, (arXiv, in progress).

[53] G. e. a. Giacalone, „EMMI Rapid Reaction Task Force, Nuclear physics confronts relativistic collisions of isobars“, (arXiv, in preparation).

[54] F. Capellino et al., „Fluid-dynamics of charm quarks in the quark–gluon plasma“, arXiv:2307.14449 (2023).

[55] F. Capellino et al., „Momentum distribution of charm hadrons in a fluid-dynamic approach“, arXiv:2307.15580 (2023).

[56] M. Al Qahtani et al., „Anisotropic flow in ultracentral nucleus–nucleus collisions“, (arXiv, in preparation).

[57] L. Rezzolla and O. Zanotti, Relativistic hydrodynamics, EBSCO ebook academic collection (OUP Oxford, 2013).

[58] L. Landau and E. Lifshitz, Fluid mechanics: volume 6, Bd. 6 (Elsevier Science, 2013).

[59] A. Jaiswal and V. Roy, „Relativistic hydrodynamics in heavy-ion collisions: general aspects and recent developments“, Adv. High Energy Phys. **2016**, 9623034 (2016).

[60] G. S. Denicol, H. Niemi, E. Molnar, and D. H. Rischke, „Derivation of transient relativistic fluid dynamics from the Boltzmann equation“, Phys. Rev. D **85**, [Erratum: Phys.Rev.D 91, 039902 (2015)], 114047 (2012).

[61] P. Romatschke and U. Romatschke, Relativistic Fluid Dynamics In and Out of Equilibrium, Cambridge Monographs on Mathematical Physics (Cambridge University Press, May 2019).

[62] W. Israel and J. Stewart, „Transient relativistic thermodynamics and kinetic theory“, Annals of Physics **118**, 341–372 (1979).

[63] J. L. Cervantes-Cota and J. Klapp, „Fluids in cosmology“, edited by L. Di G. Sigalotti, J. Klapp, and E. Sira, 71–105 (2014).

[64] A. Erschfeld and S. Floerchinger, „Dark matter vorticity and velocity dispersion from truncated Dyson-Schwinger equations“, JCAP **02**, 053 (2024).

[65] S. Weinberg, Gravitation and cosmology: principles and applications of the general theory of relativity (Wiley, 1972).

[66] S. Brandstetter et al., „Emergent hydrodynamic behaviour of few strongly interacting fermions“, (2023).

[67] S. Floerchinger, G. Giacalone, L. H. Heyen, and L. Tharwat, „Qualifying collective behavior in expanding ultracold gases as a function of particle number“, Phys. Rev. C **105**, 044908 (2022).

[68] H. Van Ness, M. Abbott, M. Swihart, and J. Smith, Introduction to chemical engineering thermodynamics (McGraw-Hill Education, 2017).

[69] M. Hafez and D. Kwak, Numerical simulations of incompressible flows (World Scientific, 2003).

[70] D. McLean, Understanding aerodynamics: arguing from the real physics, Aerospace Series (Wiley, 2012).

[71] O. Faltinsen, Hydrodynamics of high-speed marine vehicles (Cambridge University Press, 2006).

[72] J. Stam, „Real-time fluid dynamics for games“, in (2003).

[73] Clay mathematics institute, millenium problems, navier-stokes equation, `https://www.claymath.org/millennium/navier-stokes-equation/`, May 2023.

[74] C. Eckart, „The thermodynamics of irreversible processes. iii. relativistic theory of the simple fluid“, Phys. Rev. **58**, 919–924 (1940).

[75] I. Muller, „Zum Paradoxon der Warmeleitungstheorie“, Z. Phys. **198**, 329–344 (1967).

[76] I. Muller, „Speeds of propagation in classical and relativistic extended thermodynamics“, Living Rev. Rel. **2**, 1 (1999).

[77] D. Jou, J. Casas-Vázquez, and G. Lebon, Extended irreversible thermodynamics: with 15 tables, Physics and astronomy online library (Springer, 2001).

[78] B. Carter, „Convective variational approach to relativistic thermodynamics of dissipative fluids“, Proceedings of the Royal Society of London. Series A: Mathematical and Physical Sciences **433**, 45–62 (1991).

[79] M. Grmela and H. C. Öttinger, „Dynamics and thermodynamics of complex fluids. i. development of a general formalism“, Phys. Rev. E **56**, 6620–6632 (1997).

[80] G. S. Denicol, H. Niemi, E. Molnar, and D. H. Rischke, „Derivation of transient relativistic fluid dynamics from the Boltzmann equation“, en, Phys. Rev. D **85**, 114047 (2012).

[81] S. Floerchinger and E. Grossi, „Causality of fluid dynamics for high-energy nuclear collisions“, JHEP **08**, 186 (2018).

[82] S. Floerchinger and U. A. Wiedemann, „Characterization of initial fluctuations for the hydrodynamical description of heavy ion collisions“, en, Phys. Rev. C **88**, 044906 (2013).

[83] S. Floerchinger, „Mode-by-mode hydrodynamics: ideas and concepts“, en, Nuclear Physics A **926**, 115–121 (2014).

[84] S. Floerchinger and U. A. Wiedemann, „Statistics of initial density perturbations in heavy ion collisions and their fluid dynamic response“, en, J. High Energ. Phys. **2014**, 5 (2014).

[85] E. Cheney and D. Kincaid, Linear algebra: theory and applications (Jones and Bartlett Publishers, 2009).

[86] L. Trefethen and D. Bau, Numerical linear algebra (Society for Industrial and Applied Mathematics, 1997).

[87] A. Bazavov et al. (HotQCD), „Equation of state in (2+1)-flavor QCD“, Phys. Rev. D **90**, 094503 (2014).

[88] S. Borsanyi et al., „Calculation of the axion mass based on high-temperature lattice quantum chromodynamics“, Nature **539**, 69–71 (2016).

[89] P. Huovinen and P. Petreczky, „QCD Equation of State and Hadron Resonance Gas“, Nucl. Phys. A **837**, 26–53 (2010).

[90] F. Karsch, D. Kharzeev, and K. Tuchin, „Universal properties of bulk viscosity near the qcd phase transition“, Physics Letters B **663**, 217–221 (2008).

[91] N. Christiansen, M. Haas, J. M. Pawlowski, and N. Strodthoff, „Transport coefficients in yang-mills theory and qcd“, Phys. Rev. Lett. **115**, 112002 (2015).

[92] N. Christiansen, M. Haas, J. M. Pawlowski, and N. Strodthoff, „Transport coefficients in yang-mills theory and qcd“, Physical Review Letters **115**, 10.1103/physrevlett.115.112002 (2015).

[93] J. S. Moreland, J. E. Bernhard, and S. A. Bass, „Bayesian calibration of a hybrid nuclear collision model using p-Pb and Pb-Pb data at energies available at the CERN Large Hadron Collider“, Phys. Rev. C **101**, 024911 (2020).

[94] W. Press, Numerical recipes 3rd edition: the art of scientific computing, Numerical Recipes: The Art of Scientific Computing (Cambridge University Press, 2007).

[95] M. Abramowitz and I. Stegun, Handbook of mathematical functions: with formulas, graphs, and mathematica Applied mathematics series (Dover Publications, 1965).

[96] H. Ma, „Chebyshev–legendre super spectral viscosity method for nonlinear conservation laws“, SIAM Journal on Numerical Analysis **35**, 893–908 (1998).

[97] A. Gelb and E. Tadmor, „Enhanced spectral viscosity approximations for conservation laws“, Applied Numerical Mathematics **33**, 3–21 (2000).

[98] E. Tadmor and K. Waagan, „Adaptive spectral viscosity for hyperbolic conservation laws“, SIAM Journal on Scientific Computing **34**, A993–A1009 (2012).

[99] S. S. Gubser, „Symmetry constraints on generalizations of bjorken flow“, Phys. Rev. D **82**, 085027 (2010).

[100] H. Marrochio et al., „Solutions of conformal israel-stewart relativistic viscous fluid dynamics“, Phys. Rev. C **91**, 014903 (2015).

[101] S. S. Gubser and A. Yarom, „Conformal hydrodynamics in minkowski and de sitter spacetimes“, Nuclear Physics B **846**, 469–511 (2011).

[102] S. Floerchinger and U. A. Wiedemann, „Kinetic freeze-out, particle spectra and harmonic flow coefficients from mode-by-mode hydrodynamics“, en, Phys. Rev. C **89**, 034914 (2014).

[103] A. Kirchner, E. Grossi, and S. Floerchinger, „Cooper-frye spectra of hadrons with viscous corrections including feed down from resonance decays“, (2023).

[104] A. Mazeliauskas, S. Floerchinger, E. Grossi, and D. Teaney, „Fast resonance decays in nuclear collisions“, en, Eur. Phys. J. C **79**, 284 (2019).

[105] R. Hagedorn, „Statistical thermodynamics of strong interactions at high-energies“, Nuovo Cim. Suppl. **3**, 147–186 (1965).

[106] R. Hagedorn and J. Ranft, „Statistical thermodynamics of strong interactions at high-energies. 2. Momentum spectra of particles produced in pp-collisions“, Nuovo Cim. Suppl. **6**, 169–354 (1968).

[107] L. D. Landau, „On the multiparticle production in high-energy collisions“, Izv. Akad. Nauk Ser. Fiz. **17**, 51–64 (1953).

[108] G. Milekhin, „Hydrodynamic theory of multiple production of particles in collisions between fast nucleons and nuclei“, SOVIET PHYSICS JETP **35** (1959).

[109] F. Cooper and G. Frye, „Single-particle distribution in the hydrodynamic and statistical thermodynamic models of multiparticle production“, Phys. Rev. D **10**, 186–189 (1974).

[110] S. A. Bass, J. Bernhard, and J. S. Moreland, „Determination of quark-gluon-plasma parameters from a global bayesian analysis“, Nuclear Physics A **967**, 67–73 (2017).

[111] A. Mazeliauskas and V. Vislavicius, „Temperature and fluid velocity on the freeze-out surface from π, K, p spectra in pp, p-Pb and Pb-Pb collisions“, Phys. Rev. C **101**, 014910 (2020).

[112] L. Vermunt et al., „Mapping properties of the quark gluon plasma in pb-pb and xe-xe collisions at energies available at the cern large hadron collider“, Physical Review C **108**, `10.1103/physrevc.108.064908` (2023).

[113] J. E. Bernhard et al., „Applying Bayesian parameter estimation to relativistic heavy-ion collisions: simultaneous characterization of the initial state and quark-gluon plasma medium“, Phys. Rev. C **94**, 024907 (2016).

[114] H. Song and U. Heinz, „Causal viscous hydrodynamics in 2 + 1 dimensions for relativistic heavy-ion collisions“, Phys. Rev. C **77**, 064901 (2008).

[115] S. Bass et al., „Microscopic models for ultrarelativistic heavy ion collisions“, Progress in Particle and Nuclear Physics **41**, 255–369 (1998).

[116] S. Ryu et al., „Effects of bulk viscosity and hadronic rescattering in heavy ion collisions at energies available at the BNL Relativistic Heavy Ion Collider and at the CERN Large Hadron Collider“, Phys. Rev. C **97**, 034910 (2018).

[117] B. Abelev et al. (ALICE), „Centrality dependence of π, K, p production in Pb-Pb collisions at $\sqrt{s_{NN}}$ = 2.76 TeV“, Phys. Rev. C **88**, 044910 (2013).

[118] K. Aamodt et al. (ALICE), „Higher harmonic anisotropic flow measurements of charged particles in Pb-Pb collisions at $\sqrt{s_{NN}}$=2.76 TeV“, Phys. Rev. Lett. **107**, 032301 (2011).

[119] G. Giacalone, G. Nijs, and W. van der Schee, „Determination of the Neutron Skin of Pb208 from Ultrarelativistic Nuclear Collisions“, Phys. Rev. Lett. **131**, 202302 (2023).

[120] C. Sirimanna et al. (JETSCAPE), „Photon-triggered jets as probes of multi-stage jet modification“, in 30th International Conference on Ultrarelativstic Nucleus-Nucleus Collisions (Jan. 2024).

[121] D. Devetak et al., „Global fluid fits to identified particle transverse momentum spectra from heavy-ion collisions at the Large Hadron Collider“, arXiv:1909.10485 [hep-ph, physics:nucl-ex, physics:nucl-th] (2019).

[122] J. Adam et al. (ALICE), „Direct photon production in Pb-Pb collisions at $\sqrt{s_{NN}} = 2.76$ TeV“, Phys. Lett. B **754**, 235–248 (2016).

[123] M. M. Aggarwal et al. (WA98), „Observation of direct photons in central 158-A-GeV Pb-208 + Pb-208 collisions“, Phys. Rev. Lett. **85**, 3595–3599 (2000).

[124] A. Adare et al. (PHENIX), „Enhanced production of direct photons in Au+Au collisions at $\sqrt{s_{NN}} =$ 200 GeV and implications for the initial temperature“, Phys. Rev. Lett. **104**, 132301 (2010).

[125] L. Adamczyk et al. (STAR), „Direct virtual photon production in Au+Au collisions at $\sqrt{s_{NN}} = 200$ GeV“, Phys. Lett. B **770**, 451–458 (2017).

[126] Y. Ren and A. Drees, „Study of the η to π^0 Ratio in Heavy-Ion Collisions“, Phys. Rev. C **104**, 054902 (2021).

[127] S. Collaboration et al., Search for the chiral magnetic effect with isobar collisions at $\sqrt{s_{NN}} = 200$ gev by the s 2021.

[128] S. A. Voloshin, „Testing the chiral magnetic effect with central $U + U$ collisions“, Phys. Rev. Lett. **105**, 172301 (2010).

[129] H.-j. Xu et al., „Probing nuclear structure with mean transverse momentum in relativistic isobar collisions“, Physical Review C **108**, 10.1103/physrevc.108.l011902 (2023).

[130] J. Jia and C. Zhang, „Scaling approach to nuclear structure in high-energy heavy-ion collisions“, Physical Review C **107**, 10.1103/physrevc.107.l021901 (2023).

[131] G. Nijs and W. van der Schee, „Inferring nuclear structure from heavy isobar collisions using trajectum“, SciPost Physics **15**, 10.21468/scipostphys.15.2.041 (2023).

[132] H. Li et al., „Multiphase transport model predictions of isobaric collisions with nuclear structure from density functional theory“, Physical Review C **98**, 10.1103/physrevc.98.054907 (2018).

[133] H.-j. Xu et al., „Determine the neutron skin type by relativistic isobaric collisions“, Physics Letters B **819**, 136453 (2021).

[134] J. Walecka, „A theory of highly condensed matter“, Annals of Physics **83**, 491–529 (1974).

[135] J. I. Kapusta and C. Gale, Finite-temperature field theory: principles and applications, 2nd ed., Cambridge Monographs on Mathematical Physics (Cambridge University Press, 2006).

[136] B. D. Serot and J. D. Walecka, „Relativistic nuclear many-body theory“, in Recent progress in many-body theo edited by T. L. Ainsworth, C. E. Campbell, B. E. Clements, and E. Krotscheck (Springer US, Boston, MA, 1992), pp. 49–92.

[137] S. Floerchinger and C. Wetterich, „Chemical freeze-out in heavy ion collisions at large baryon densities“, Nucl. Phys. A **890-891**, 11–24 (2012).

[138] J. Eser and J.-P. Blaizot, „Thermodynamics of the parity-doublet model: Symmetric nuclear matter and the chiral transition“, Phys. Rev. C **109**, 045201 (2024).

[139] A. Sommerfeld, „Zur elektronentheorie der metalle auf grund der fermischen statistik“, Zeitschrift für Physik **47**, 1–32.

[140] R. Kim, X. Wang, and M. Lundstrom, Notes on fermi-dirac integrals, 2019.

[141] A. Monnai, B. Schenke, and C. Shen, „Equation of state at finite densities for QCD matter in nuclear collisions“, Phys. Rev. C **100**, 024907 (2019).

[142] A. Monnai, B. Schenke, and C. Shen, „QCD equation of state at finite densities for nuclear collisions“, Nucl. Phys. A **1005**, edited by F. Liu et al., 121868 (2021).

[143] G. Gamow and E. Rutherford, „Mass defect curve and nuclear constitution“, Proceedings of the Royal Society of London. Series A, Containing Papers of a Mathematical and Physical Character **126**, 632–644 (1930).

[144] C. F. V. Weizsacker, „Zur Theorie der Kernmassen“, Z. Phys. **96**, 431–458 (1935).

[145] H. H. Rosenbrock, „Some general implicit processes for the numerical solution of differential equations“, The Computer Journal **5**, 329–330 (1963).

[146] C. Chattopadhyay, U. Heinz, and T. Schaefer, „Fluid dynamics from the Boltzmann equation using a maximum entropy distribution“, Phys. Rev. C **108**, 034907 (2023).

[147] P. Bozek, „Transverse-momentum–flow correlations in relativistic heavy-ion collisions“, Phys. Rev. C **93**, 044908 (2016).

[148] A. Mazeliauskas and D. Teaney, „Fluctuations of harmonic and radial flow in heavy ion collisions with principal components“, Phys. Rev. C **93**, 024913 (2016).

Acknowledgments

My PHD has been an exceptional experience. I want to thank all the people who accompanied and supported me during this journey.

First of all, I would like to thank my advisor Prof. Dr. Stefan Floerchinger who gave me the opportunity to pursue my PHD in his group. I am very grateful for his constant support and all the very helpful discussions about my projects and physics in general we had. He is a great source of inspiration and always motivated me to learn and understand more about physics.

Second, I want to thank Prof. Dr. Carlo Ewerz for agreeing to be my second referee and Prof. Dr. Lauriane Chomaz and Prof. Dr. Andre Butz to be part of my examination committee.

A very big thank you goes to Eduardo Grossi who helped and supported me since the beginning of my master thesis. I enjoyed working with him and learning about physics and coding from him a lot.

Additionally, I also want to thank Aleksas Mazeliauskas with whom I started working with during my master thesis already. I deeply appreciate his support for my work and career, especially after his return to Heidelberg.

Next I want to thank Giuliano Giacalone who taught me a lot about phenomenological studies and data analysis in heavy-ion collisions.

I would also like to thank the experimentalists from the ALICE groups in Heidelberg and at GSI, especially Silvia Masciocchi, Andrea Dubla, Ilya Selyuzhenkov, Luuk Vermunt, Lukas Kreis and Klaus Reygers together with their students. I always enjoyed our collaborations, discussing physics with them and learning about the experimental point of view from them.

A big thank you also goes to the phenomenology group of the GSI with Federica Capellino, Rafet Kavak and Rossana Facen. I enjoyed sharing my PHD experience, as well as the interesting discussions about physics and Italian cooking with Federica Capellino. I want to thank Rossana Facen and especially Rafet Kavak for their work with me and the possibility to tutor them during their work.

I am also very thankful for the great people in the office in Heidelberg and Jena with whom I shared many laughs and discussions ranging from chess games to physics. Special thanks goes to Lars Heyen and Laura Batini.

Ein wichtiger Teil meiner Reise und wichtiger Ausgleich war das Musizieren im Universitätsorchester der

Universität Heidelberg. Ich möchte mich bei Michael Sekulla für seinen unermüdlichen Einsatz bedanken. Besonderer Dank gilt dem Blech für die vielen Auftritte, Stimmproben und geselligen Momente nach den Proben, mit besonderem Dank an das Tiefblech mit Flora, Thomas, Paul, Valentin und Robert. Zusätzlicher Dank gilt der Donau Philharmonie Ulm mit ihrem Dirigenten Philipp Solle, sowie Felix und Ann-Katrin für das gemeinsame Musizieren und ihre endlose Gastfreundschaft.

Zusätzlich möchte ich mich bei den Schachfreunden Heidelberg, allen voran Manuel, Jörg, Christian und Christopher für die vielen interessanten Vereinsabende und Mannschaftskämpfe bedanken. Besonderer Dank gilt hier auch Kalle und Dieter für die vielen schönen Abende.

Zuletzt möchte ich mich ein paar sehr wichtigen Leuten zuwenden. Allen voran Daniel Boneß, mit dem mich seit dem wir uns im Vorkurs des Bachelors kennen gelernt haben eine tiefe Freundschaft verbindet. Ich bin sehr dankbar für die vielen gemeinsamen Stunden, die wir mit Zetteln, der Bachelor- und Masterarbeit und anderem verbracht haben.

Abschließend möchte ich mich bei meiner Familie bedanken, angefangen bei meinen Großeltern Babette, Paul, Ingrid und Wolfgang sowie Lilo und Roland und meinen Onkeln Steffen und Peter, die mich immer unterstützt haben. Mein Größter Dank gilt meinen Eltern Ullrich und Bettina und meiner Schwester Viktoria. Diese Arbeit war nur durch ihre andauernde Unterstützung und das Wissen, dass ich mich egal mit was an sie wenden kann möglich.